UNIVERSITÄT ROSTOCK

Development of Palladium Nanoparticles Based Catalysts for Aerobic Oxidation of 5-Hydroxymethylfurfural and Glycerol

Dissertation

zur
Erlangung des Doktorgrades
doctor rerum naturalium (Dr. rer. nat.)
der Mathematisch-Naturwissenschaftlichen Fakultät
der Universität Rostock

vorgelegt von
Baraa Siyo geb. am 29. August 1985, Latakia, Syrien
Rostock, Juni 2014

urn:nbn:de:gbv:28-diss2014-0180-6

Einreichung der Dissertation: 25. Juni 2014

1. Gutachter: Prof. Dr. Peter Langer, Institut für Chemie, Universität Rostock, Germany
2. Gutachter: Prof. Dr. Johannes Gerardus de Vries, Leibniz Institut für Katalyse, Rostock, Germany

Tag der öffentlichen Verteidigung: 21. Oktober 2014

Die vorliegende Arbeit entstand in der Zeit von Januar 2012 bis Juni 2014 im Leibniz Institute für Katalyse (Likat) an der Universität Rostock.

Eidesstattliche Erklärung

Hiermit erkläre ich, dass diese Arbeit bisher von mir weder an der Mathematisch-Naturwissenschaftlichen Fakultät der Universität Rostock noch einer anderen wissenschaftlichen Einrichtung zum Zwecke der Promotion eingereicht wurde. Ich erkläre auch, dass ich diese Arbeit selbständig angefertigt und ohne fremde Hilfe verfasst habe, keine außer den von mir angegebenen Hilfsmitteln und Quellen dazu verwendet habe und die den benutzten Werken inhaltlich und wörtlich entnommen Stellen als solche kenntlich gemacht habe.

Baraa Siyo
Rostock, Juni 2014

Acknowledgment

I would like to express my utmost gratitude, indebtedness and appreciation to Prof. Dr. Peter Langer for giving me the opportunity to work in his research group and for his kind supervision, support, and encouragement.

I would like highly acknowledge Dr. Norbert Steinfeldt for his guidance, support, and revisions throughout my research work

I am especially grateful to Dr. Habil. Klaus Jänisch, Prof. Johannes G. de Vries and Prof. Norbert Kockmann for their support and advices throughout my work.

I would like to express my sincere thanks to all the current members of our research group, Dr. Heike Erich, Dr. Sandra Hübner, Dr. Patrick Loos, Michael Sebek, Manuela Pritzkow Hannes Alex, Dr. Jens Baumgard, Dr. Elka Kraleva, Saioa Goicoechea and Jola Pospech for their helpfulness throughout my work and for the friendly atmosphere.

I express high gratitude to the analytical department in the Leibniz institute for catalysis, Dr. Wolfgang Baumann, Dr. Matthias Schneider, Dr. Marga-Martina Pohl, and Dr. Jörg Radnik for their assistance in the interpretation of the results.

I am grateful to my country 'Syria Arab Republic' especially to Tishreen University in Latakia and to the DAAD for their financial support.

I acknowledge all my previous teachers and professors in Tishreen University especially Prof. Dr. Shahid Mustafa for his support and encouragement.

All words are not enough to express my thankfulness and gratitude to my parents for their love and support although the long distance between us. They are the source of hope and happiness. I owe sincere and heartiest gratitude to my beloved brothers (Emad, Muhammad, and Ziad) and sisters (Abeer, Rasha, and Roaa) for their eternal love, support, and encouragement.

Baraa Siyo

Dedication

I affectionately dedicate this thesis to the candles whom lighten my way

"My parents"

"فاروق سيو&اميرة ديب"

Baraa Siyo

Abstract

In this dissertation, mono- and bimetallic polyvinylpyrrolidone stabilized palladium nanoparticles were synthesized via the polyol method. The prepared nanoparticles were deposited onto different metal oxide supports and then applied in the oxidation of 5-hydroxymethylfurfural (HMF) and glycerol (GLY) with and without addition of homogenous base using molecular oxygen as oxidant. A high yield of 2,5-furandicarboxylic acid (FDCA) > 90 % connected with a relatively stable catalytic performance was obtained by oxidation of HMF in alkaline solution on a Pd/ZrO_2/La_2O_3 catalyst. A lactic acid (LA) yield of 75 % was obtained by the oxidation of GLY in alkaline solution on a Pd-Ag/TiO_2 catalyst (Pd:Ag = 4:1 mol/mol) which additionally showed a stable catalytic performance when the catalyst was recycled. Various characterization methods including XRD, TEM, SAXS, XPS and AAS were applied to obtain information about the size of Pd NPs and their electronic structure before and after utilization in the oxidation reactions, thus, to make a correlation between the characteristics of the catalysts and their catalytic performance.

Zusammenfassung

Im Rahmen der hier vorliegenden Doktorarbeit wurden mono- und bimetallische Polyvinylpyrrolidon stabilisierte Pd-Nanopartikel (NPs) mit Hilfe der Polyol-Methode hergestellt. Diese NPs wurden auf verschiedenen Trägermaterialien abgeschieden und in der Oxidation von 5-Hydroxymethylfurfural (HMF) und Glycerin (GLY) getestet. Die Reaktion wurde mit und ohne lösliche Base und mit molekularem Sauerstoff als Oxidationsmittel durchgeführt. Eine hohe Ausbeute an 2,5-Furandicarbonsäure (FDCA) von mehr als 90 %, verbunden mit einer relativ hohen Stabilität des Katalysators, wurde bei der Oxidation von HMF in alkalische Lösung mit Pd/ZrO_2/La_2O_3 erreicht. Bei der Oxidation von GLY in alkalische Lösung mit einem Pd-Ag/TiO_2 Katalysator (Pd:Ag = 4:1 mol/mol) konnte eine Ausbeute von 75 %, bezogen auf die Milchsäure, erzielt werden. Zusätzlich blieb die Katalysator-Performance über mehrere Recyclingversuche hinweg stabil. Verschiedene Methoden wie XRD, TEM, SAXS, XPS und AAS wurden zur Charakterisierung der Pd-Katalysatoren eingesetzt. Durch Korrelation der entsprechenden Daten, wie Größe und elektronischer Strukturen der Pd-NPs vor und nach dem Einsatz in der Oxidationsreaktion, konnten neue Informationen über die Katalysatoren und deren Anwendbarkeit gewonnen wurden.

List of Abbreviations

Acetic acid	AA
Brunauer–Emmett–Teller	BET
Conversion	X
Copper	Cu
Diameter	d
Dihydroxyacetone	DHA
Ethylene glycol	EG
Energy Dispersive X-Ray	EDX
Formic acid	FA
5-Formylfuran-2-carboxylic acid	FFCA
2,5-Furandicarboxylic acid	FDCA
Glycerol	GLY
Glyceraldehyde	GLYHD
Glyceric acid	GLYA
Glycolic acid	GOA
Gold	Au
Hydrotalcite	HT
Hour	h
High angle annular dark field	HAADF
High performance liquid chromatography	HPLC
5-Hydroxymethylfurfural	HMF
5-Hydroxymethylfuran-2-carboxylic acid	HMFCA
Inductively coupled plasma	ICP
Lactic acid	LA
Metal	M

Nanoparticles	NPs
Nuclear magnetic resonance	NMR
Oxalic acid	OXA
Palladium	Pd
Powder x-ray diffraction	XRD
Polyvinylpyrrolidone	PVP
Radius	R
Small angle x-ray scattering	SAXS
Scanning transmission electron microscopy	STEM
Scanning electron microscopy	SEM
Silver	Ag
Selectivity	S
Tartonic acid	TA
Transmission electron microscopy	TEM
Turnover frequency	TOF
Ultraviolet –visible	Uv-Vis
Yield	Y
X-ray photoelectron spectroscopy	XPS

Table of Content

List of Figures

List of Tables

List of Schemes

1. Introduction and Objective

Metal nanoparticles dispersed onto various supports (e.g. metal oxide) are widely used as catalysts in many processes in the chemical industry, such as fine chemical, polymer, petrochemical and pharmaceutical industries [1]. The catalytic activity and selectivity of such materials is strongly influenced by the shape, size, and size distribution of the active metal species, nature of the support, and the interaction of active metal species with the carrier material [2].

There are various methods for preparation of heterogeneous supported catalysts in which the active metal is dispersed on a support. Conventionally, such catalysts are prepared by the adsorption of a metal species on the surface of the carrier material and subsequent thermal treatment in an oxidative and/or reductive atmosphere. The metal morphology and dispersion are strongly affected by the interaction between the metal precursor and support which is a disadvantage of this method [3, 4].

Another method which could be used to prepare heterogeneous supported catalysts is the deposition of pre-formed metal nanoparticles onto different supports [5]. In recent years, methods based on colloid chemistry have been applied to prepare mono- and bimetallic nanoparticles with controlled shape, size and narrow size distributions [6]. Deposition of the pre-formed metal nanoparticles onto different supports alters the particle size only slightly. This allowed, for example, studying the effect of support on the activity and selectivity in various heterogeneously-catalyzed reactions, isolated from the other factors of the catalyst preparation [7, 8]. Another advantage of the separately prepared metal nanoparticles based catalysts is their relatively high activity because of a high surface area to volume ratio [2].

The interest in the synthesis of fine and bulk chemicals from renewable feedstocks have increased significantly in recent years because the supply of fossil fuels is limited.

5-Hydroxymethylfurfural (HMF) is considered as a promising chemical for several industrial applications because it is available from biomass (e.g. fructose or glucose) and could serve as building block for many other molecules [9-12]. One of the promising products obtained from HMF oxidation is 2,5-furandicarboxylic acid (FDCA), which is considered as one of the twelve most important biomass derived chemicals [13]. FDCA is considered to be a potential alternative for the terephtalic acid that is used for the preparation of polyethylene terephthalate (PET) [14].

Glycerol (GLY, 1,2,3-propane triol), a by-product of biodiesel production through trans-esterification of triglycerides, is a highly versatile building block, due to its easy availability and its high functionalization [15]. One of the promising routes is the catalytic oxidation of GLY to lactic acid (LA). LA is considered as an important chemical for many applications in the food, cosmetic, and pharmaceutical industries [16].

Pd based materials have been successfully applied in the aerobic oxidation of alcohols to carbonyl groups, both in organic and aqueous reaction media [17-28]. So far, studies of Pd based materials in HMF oxidation were reported only on Pd/C catalysts [23]. Here, only the rate and product distribution for HMF oxidation over Pd/C was compared with that from the other supported metal Pt/C and Au/C catalysts. However, the influence of the support, correlation of Pd catalysts properties (e.g. particle size) with their catalytic performance and the stability of Pd catalysts in HMF oxidation has not yet been studied.

In glycerol oxidation, the influence of particle size of Pd catalysts on the glycerol oxidation and optimization of reaction conditions over this catalyst were already studied, where the reaction was orientated to glyceric acid [24, 26, 29-31]. So far, three studies were published for the oxidation of glycerol to lactic acid under strong basic conditions (NaOH:GLY= 4:1 mol/mol) using Au-Pt/TiO_2 [32], Au-Pt/CeO_2 [33], and Au/CeO_2 [34] catalysts with a high yield of (≥ 80 %). With Pd catalysts, only results on an Au-Pd/TiO_2 have been reported in glycerol oxidation towards lactic acid in an acidic medium with a low yield of 47 % [35]. However, the influence of varying bimetallic Pd-M (M= Ag, or Cu) catalysts composition on glycerol conversion and lactic acid yield and their stability have not yet been studied. Furthermore, obtaining a high yield of lactic acid with a low amount of catalyst and low molar ratio of NaOH to GLY is still open to investigation.

This work aims to provide a better understanding of the individual steps in the development of supported catalysts with pre-formed palladium nanoparticles in order to obtain active and selective catalysts for the selective oxidation of 5-hydroxymethylfurfural and glycerol in aqueous solution using molecular oxygen as oxidant as follows:

- Preparation of differently sized palladium nanoparticles by the polyol method, to study the relationship between the particle size of palladium nanoparticles and their catalytic performance in the oxidation reaction.
- Deposition of pre-formed palladium nanoparticles onto different metal oxide supports, to study the influence of support on catalytic performance of supported palladium nanoparticles in the oxidation reactions.
- Modification of the surface of pre-formed palladium nanoparticles by adding a second metal (e.g. Ag, Au, or Cu) and subsequent deposition of these bimetallic nanoparticles onto support, to enhance their catalytic performance in the oxidation reactions.

Additionally, the possibility of reusability of the catalysts and the influence of reaction parameters on the oxidation reactions were studied as well. The catalysts were characterized using XRD, XPS and TEM and compared before and after utilization in oxidation reactions.

Scheme 1 represents the schematic structure of this work.

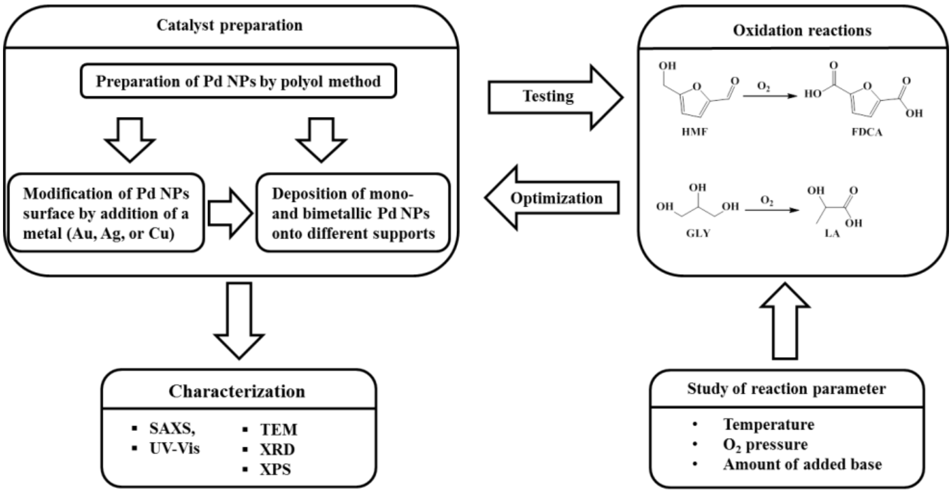

Scheme 1. **Schematic structure of the work.**

2. Theoretical Part

Catalysis evolved to be a powerful technology in the bulk chemicals, fine chemicals, pharmaceuticals and petrochemical industries [36]. The term catalyst originated from the Greek word (κατάλυσις) which means dissolution. The term catalysis was first used by Berzelius in 1836 to introduce a new process by which a chemical reaction could be promoted by using a catalyst. By definition, a catalyst can accelerate a reaction rate without being consumed in the process [37]. Catalysts can be divided into three main groups, i.e. heterogeneous, homogenous and enzymatic catalysts. There is another kind of catalyst and it is called quasi-homogenous (unsupported metal nanoparticle) [38].

2.1 Metal nanoparticles

2.1.1 Properties and synthesis of nanoparticles

By definition nanoparticles are materials exhibiting particle sizes in the range of 1 to 100 nm, which are similar to ultrafine particles but clearly smaller than fine particles which cover a range of 100 to 2500 nm. Nanoparticles can be metal clusters (agglomerates of metal atoms) or small colloidal particles. It is worth noting that, not all small colloidal particles are nanoparticles [2, 39]. The term colloidal particle describes a compound in the colloidal system which is dispersed as very fine particles in another compound (dispersion medium). Colloid science has a long history. Already in 1861 Thomas Graham coined this name according to the Greek word "κολλα" which means glue, as some of his colloidal systems were glue-like. However, the nomenclature of Graham did not give information about the size range. Much later on in 1972 Everett [40] defined the size of colloids to be in the range of 1 to 1000 nm. Nanoparticles have been shown to exhibit structural, electronic, magnetic, and optical properties that differ from those of the corresponding bulk materials [41].This is due to an increased surface area which results in higher reactivity, quantum effects and lower melting points. Figure 1 shows the formation of discrete electronic energy levels on the way from bulk to molecule.

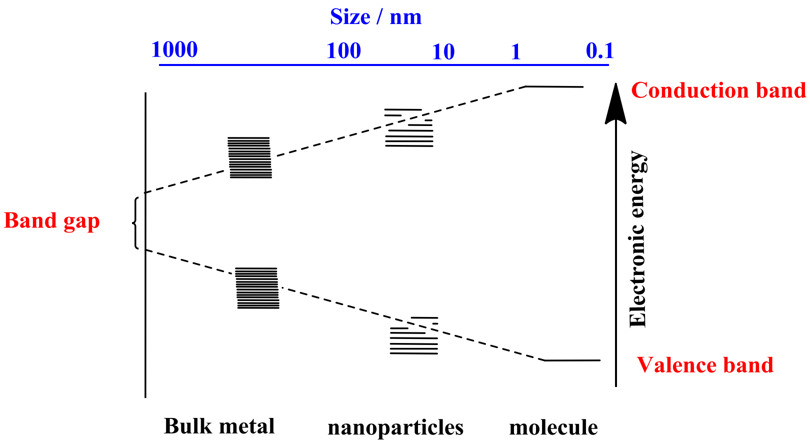

Figure 1. Formation of discrete electronic energy levels on the way from bulk to molecule [42].

In the bulk metal the band is formed by the combination of neighboring energy levels of several atoms. When the particle size decreases and reaches the nanoscale every particle is made up of a smaller number of atoms. The number of overlapping orbitals or energy levels changes dramatically in these bands leading to a larger band gap (the differences between the highest valence band and the lowest conduction band). This effect explains the nanoparticles have a wider band gap than the corresponding bulk metal.

There are two basic methods to synthesize nanoparticles: "top down" and "bottom up" (Figure 2) [43]. The so-called "top down" method is a physical method, which generates nanoparticles by crushing of a bulk substrate via various techniques e.g. mechanical, thermal or irradiative methods. The "top down" approach usually leads to a very broad size distribution. The "bottom up" method is classified as chemical method. Here, nanoparticles are prepared from atomic or molecular precursors. This method allows forming nanoparticles in a highly controlled manner.

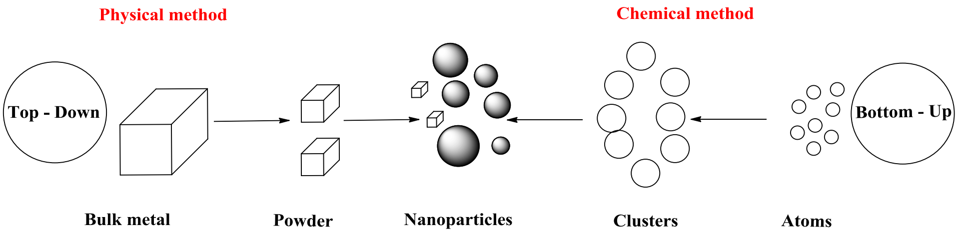

Figure 2. Schematic of methods to prepare metal nanoparticles [43].

One of the first models used to describe the nanoparticle formation was given by LaMer in 1950. LaMer and co-workers illustrated the production of monodispersed sulfur sols by the decomposition of dilute sodium thiosulfate in dilute hydrochloric acid [44]. Figure 3 shows the LaMer process. It was stated that the process can be divided into three steps. The first step is the generation of sulfur. During this so called pre-nucleation stage, the amounts of sulfur increase to the critical concentration (c_{crit}). The (c_{crit}) is the minimal concentration for nucleation. The concentration of sulfur is still increasing up to the point of super-saturation (c_{max}) which is considered as the maximal concentration for nucleation. No additional nucleation will happen if the concentration of sulfur lowers below the level of minimum super-saturation. The third step represents the growth stage, where the sulfur concentration decreases to the solubility level (c_s, growth stage).

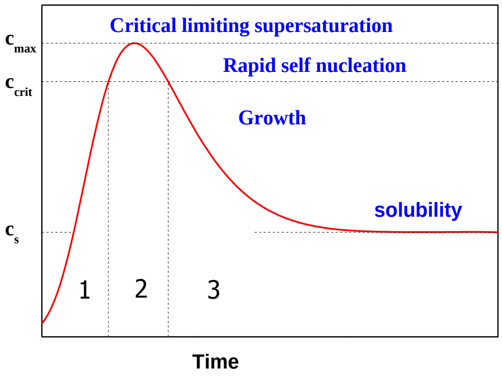

Figure 3. LaMer model of the sulfur sols [44].

Various sub-methods of using the Bottom-up approach have prevailed because of the controlled growth. Selected methods which are widely applied in the synthesis of nanoparticles will be described in the following section [45].

2.1.1.1 Chemical reduction

As early as 1857, Faraday investigated the synthesis of a colloidal gold solution by reduction of $HAuCl_4$ with phosphorus [46]. One of the first reproducible procedures for the preparation of metal colloids in solution was established by Turkevtich et al. in the early 1950s [47-49]. They prepared 20 nm gold particles by reduction of $[AuCl_4]^-$ with sodium citrate. Additionally, they were the first to propose a mechanism for the stepwise formation of nanoparticles based on nucleation, growth and agglomeration as illustrated in Figure 4.

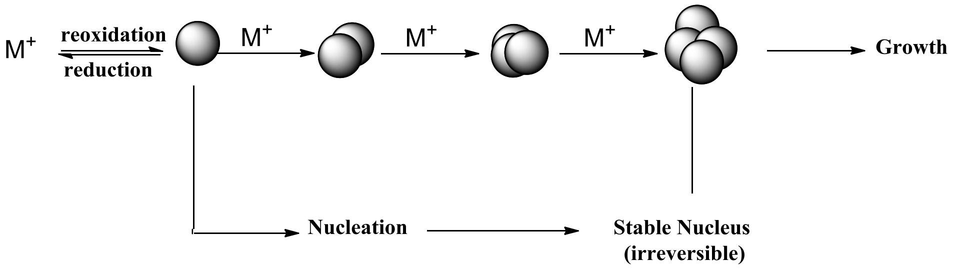

Figure 4. Formation of nanostructured metal colloids by reduction of metal salt [47-49].

The polyol process is a method which is often applied for the preparation of nanoparticles with controlled shape and size. The polyol method was first introduced by Fievet et al. for preparation of e.g. gold, palladium, iridium, osmium, copper, silver, cobalt, lead, or cadmium nanoparticles [50, 51]. In this process, nanoparticles are prepared by reduction of an inorganic metal precursor in liquid polyol. The polyol acts as both, solvent and reducing agent. Common choices of polyol involve ethylene glycol, 1,2-propylene glycol, and 1,5-pentanediol. Ethylene glycol exhibits a high boiling point (197 °C) which allows the synthesis of nanoparticles in a wide temperature range [52]. One advantage of a polyalcohol over other reducing agents such as sodium borohydride or other boranes is that ketones and carboxylic acids are formed as oxidation products, which can be easily separated from the reaction solution [53, 54]. The mechanism of platinum or ruthenium nanoparticle formation in ethylene glycol was proposed to involve the reduction of metal ion (M^{n+}) to metal zero (M^0) while ethylene glycol get oxidized to glycolic acid. Furthermore, it was proposed that hydroxide ions (OH^-) are required to generate acetate ions (glycolate) which could act as stabilizing agent for the metal nanoparticles (Pt or Ru NPs) in ethylene glycol [55, 56]. It is worth pointing out that the polyol method doesn’t require any special equipment and it can be used to synthesize different nanoparticles even in relatively high concentration compared to other methods.

2.1.1.2 Electrochemical synthesis

Reetz et al. [57] have developed an electrochemical method for the synthesis of mono- and bimetallic nanoparticles since 1994. The principle of this method can be briefly described as follows: i) oxidative dissolution of the metal anode, ii) transfer of the metal ions to the cathode, iii) the reduction of the metal ion to metal zero at the cathode, iv) nucleation of particles followed by growth, vi) control of the growth step and stabilizing of the formed nanoparticles with stabilizing agent. In the case of the preparation of bimetallic nanoparticles, the same steps will be followed but using two metal anodes simultaneously instead of one. The advantage of the electrochemical method is the avoidance of contaminating by-products which are formed from chemical reducing agent and the simple isolation of the products from the precipitate.

2.1.1.3 Reduction of organic ligands in organometallic precursors

This method was used to prepare metallic nanoparticles using the low valence of a metal complex. The ligands can be reduced with either hydrogen or carbon monoxide. The reduced ligands leave the metallic center. Thus, this method leads to formation of cluster of metal atoms [58].

2.1.1.4 Thermal decomposition

The thermal decomposition of organometallic compounds in high boiling organic solvents in the presence of stabilizing surfactants leads to the formation of nanoparticles. One major advantage is the high crystallinity and mono-dispersity of the prepared nanoparticles [59].

2.1.2 Nanoparticle stabilization

Metallic nanoparticles have a high ratio of surface area to volume. Thus, they have an excess surface free energy corresponding to the lattice energy. This makes them thermodynamically unstable in solution. Therefore, protective agents are essential in order to be able to outbalance the attractive van der Waals forces. The stabilization can be achieved in three different ways. The first type is electrostatic stabilization (e.g. inorganic or organic ions). The anions and cations in the solution derived from the starting materials will be connected with the nanoparticle. This leads to an electrical double layer around the particle, the resulting Coulombic repulsion prevents the nanoparticles from agglomeration. The second type of the stabilization is steric. For instant, nonionic polymers or surfactants could prevent the agglomeration of the nanoparticles mainly due to the adsorption of the large molecules. The third type of NPs stabilization is by electrosteric forces (e.g. ionic surfactant or polymers-polyelectrolytes) [60]. This type of stabilization is a combination of both effects (steric and electrostatic). Selections of stabilizers (e.g. linear polymers, dendrimers, and ligands), which are widely utilized, will be described below [60, 61]:

2.1.2.1 Linear polymers

Linear polymers are widely utilized as stabilizers. A common stabilizer in NPs preparation is poly (*N*-vinyl-2-pyrrolidone) (PVP) because it is harmless and soluble in many polar solvents. PVP mainly stabilizes the nanoparticles through steric effects of its framework. PVP could interact with the surface of the nanoparticles through polymer functional groups (C=O, C-N) [60, 62]. Figure 5 shows the stabilization of nanoparticles by PVP. Two protective shells could be formed around the formed nanoparticles. The first shell is created by adsorption of PVP on the surface of the nanoparticles. The second shell might be less ordered than the first, with the PVP dissolving freely in the suspension [45].

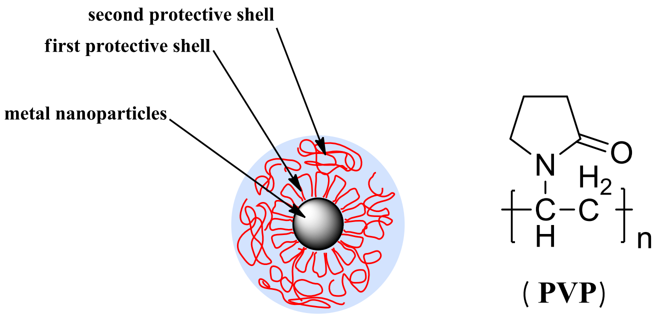

Figure 5. Schematic illustration of PVP protected metal nanoparticles [45].

2.1.2.2 Dendrimers

Dendrimers are hyper-branched macromolecules which can support the stability of a nanoparticle especially if a heteroatom is incorporated. Most dendrimers employed as stabilizer for nanoparticle synthesis, are nitrogen-based e.g. poly (propylene imine) (PPI) and poly(amido amine) (PAMAM) [63], which is the most commonly used dendrimer. However, the major drawback of dendrimers is their limited solubility, which greatly limits their utility. PAMAM, for example, is only soluble in few solvents, such as water, alcohols, and weak acids in low concentrations. The instability of dendrimers at a high temperature of 150 °C to 300 °C is considered as disadvantage as well [64, 65]. Furthermore, the dendrimers are not favored economically because they are costly.

2.1.2.3 Ligands

Ligands are widely utilized as protecting agent for the nanoparticle. Typically, the ligands have a heteroatom, which provides an accessible lone pair. This leads to a strong bond between the ligand and the surface of the metal, with the organic chain of the ligand preventing the NPs from agglomeration [5, 66]. There are different types of ligand and some of these involve phosphines [67], thiols [68, 69], or amines [70].

2.1.3 Palladium nanoparticles: synthesis and application

Noble metals and especially palladium (Pd) play an important role in chemical synthesis, and pollution abatement. Palladium is widely used as heterogeneous and homogenous catalyst in many industrial applications e.g. in cleaning of automobile exhaust, the synthesis of vinyl acetate or the hydrogenation of acetylene [71]. The first successful example of palladium-catalyzed aerobic oxidation of secondary alcohols to ketones was reported by Blackburn and Schwartz in 1977 [25]. Further successful studies of oxidations with palladium catalysts were reported for e.g. glycerol [26], α,β-unsaturated alcohols [27], benzyl alcohol [28], and 2-hexanol [18].

Palladium nanoparticles can be prepared using different methods as described before in Section 2.1.1, applying different Pd salt precursors, reducing agents, and stabilizers [6, 72]. Sawoo et al. synthesized Pd NPs by reduction of a Pd precursor (K_2PdCl_4) in water with a fisher carbene complex using polyethylene glycol (PEG) as stabilizer agent. They stated that the size of Pd NPs decreased as the molar ratio of the PEG to Pd increased in the synthesis solution [73]. Ramirez et al. [54] have synthesized palladium nanoparticles by hydrogenation of tris (dibenzylideneacetone)dipalladium [$Pd_2(dba)_3$] in tetrahydrofuran (THF) using organic ligands (polyphosphines).

Baumgard et al. [74] synthesized PVP protected Pd NPs using Na_2PdCl_4 as Pd precursor by the polyol method (ethylene glycol acts as solvent and reducing agent). Additionally, he studied the influence of the reaction parameters on the particle size in batch e.g. molar ratio of NaOH to Pd, Pd precursor concentration, molar ratio of Pd to stabilizer (PVP), and the reaction temperature. The variation of the initial concentration of Pd salt did not show any increase or decrease in the particle sizes. It was stated that this behavior was unexpected because the available amount of Pd salt should have a strong influence on the concentration of palladium atoms in solution. Thus, at low Pd concentrations, the critical nucleation concentration would be difficult to reach according to the LaMer theory and this should lead to the formation of a larger particles. In the presence of HCl the Pd NPs were only formed at very high temperatures. While in presence of NaOH, Pd NPs could be obtained at lower temperature. Therefore, he studied the influence of NaOH concentration on the particle size at

100 °C in the range 10-500 mM using 20 mM Pd. The results showed that a large particle size was obtained if the NaOH concentration was < 30 mM, otherwise smaller particles were formed. With 250 mM NaOH, particle sizes started to increase probably by aggregation of the formed particles. This was attributed to a decrease of the stabilization effect of PVP. At a very high NaOH concentration of 500 mM, a black precipitate was observed and the synthesis solution decolorized. Thus, the change in the molar ratio of NaOH to Pd ratio had the strongest influence on the particle size of the Pd NPs. In contrast, the other parameters studied had only a minor influence on the particle size. Furthermore, the OH^- concentration in the synthesis solution affected the rate of the Pd reduction and also on the temperature at which the palladium ion could be reduced [74].

2.1.4 Bimetallic nanoparticles: synthesis and application

Bimetallic nanoparticles consist of two metals and they have gained a special academic and industrial research interest. It is known that bimetallic catalysts often have a better catalytic performance in comparison with their monometallic counterparts [75, 76]. During the past years, bimetallic Pd-M (M= metal) catalysts have been successfully applied in different oxidation reactions. As examples, Pd-Au catalysts have shown interesting catalytic performances in various oxidation reactions e.g. 1-phenylethanol [77], ethanol [78], and glycerol [30]. Pd-Ag based materials also showed superior catalytic performances in e.g. the electrocatalytic oxidation of ethanol [79], glycerol oxidation [80], and benzyl alcohol oxidation [81]. In addition, Pd-Cu catalysts have been successfully applied oxidation reactions e.g. electro catalytic oxidation of methanol [82] and formic acid [83].

The influence of bimetallic catalysts on the reaction could be ascribed to different factors e.g. each metal might promote different initial reaction steps (bi-function effect), electrons might be transferred from one metal to the other, and by assemble effect, i.e. the specific group of surface atoms developed by geometric growth [76, 84-86]. Various synthesis routes were employed for the preparation of bimetallic nanoparticles. Selected methods include:

- Co-reduction: The principle of this method is based on mixing of two different metal salts and reducing them simultaneously [43].

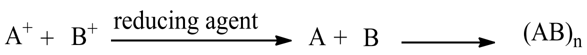

$$A^+ + B^+ \xrightarrow{\text{reducing agent}} A + B \longrightarrow (AB)_n$$

Figure 6. Schematic view of preparation of bimetallic nanoparticles by co-reduction.

- Successive reduction: The principle of this method is based on the addition of the second element onto previously formed monometallic nanoparticles. This method is usually carried out to prepare ‘core-shell’ structured bimetallic nanoparticles [43].

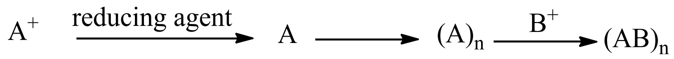

Figure 7. Schematic view of preparation of bimetallic nanoparticles by successive-reduction.

The structures of bimetallic nanoparticles can be divided into different types e.g. core-shell, random alloy, or cluster in cluster [87]. In the type which is termed as core-shell structure, the core will be formed from one metal and the other metal will locate around the core to configure a shell. The structure random-alloy could be formed if the two different metals which have similar atomic sizes are randomly located. In another configuration, named cluster-in-cluster, a nano-cluster is formed by one metal with the second metal surrounding the nano-cluster and acting as binder. This is considered to be a modified type of the core-shell structure [43]. The mentioned types are showed in Figure 8.

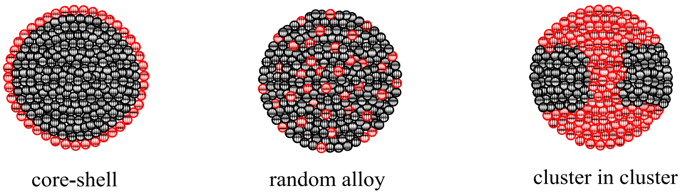

Figure 8. Various structure models of bimetallic nanoparticles.

Generally, different factors could affect the type of the structure of bimetallic nanoparticles e.g. the preparation method, reaction conditions, or the reduction kinetic of each element (redox potential) [88, 89]. As examples, the Pd(core)-Au(shell) could be synthesized by the addition of the dissolved pre-formed palladium nanoparticle in hexane solution to the gold salt ($HAuCl_4.3H_2O$) containing solution in presence of 1-octadecene and oleylamine [90]. Pd(shell)-Au(core) were synthesized by a sonochemical method [91]. The authors stated that the physical effects of the ultrasound could affect the formation of the core/shell structure [91]. Another interesting study was reported by Kuai et al. [92]. They stated that a simple method of hydrothermal co-reduction route could be used to synthesize the bimetallic Pd-Au nanoparticles in different structures (alloy or core-shell) depending on the addition of cetyltrimethylammoniumbromid (CTAB). When CTAB was added to the reaction, the formation of an alloy structure was observed. Without CTAB, a core-shell structure was formed. The reason was attributed to the poor reductive potential of the PVP comparison to CTAB. Thus, the reduction rate of both metals will be different to be with Au being reduced first and Pd being reduced secondly [92]. Pd(core)-Ag(shell) nanoparticles were successfully synthesized by the reduction of silver salt on the surface of Pd particles in presence of formaldehyde [93]. An alloy structure of PVP-protected Pd-Cu nanoparticles was synthesized by refluxing a glycol solution of copper hydroxide and palladium [94, 95].

2.1.5 Methods of catalyst preparation

Heterogeneous supported catalysts can be prepared using different methods. In conventional catalyst preparation, the support can be impregnated with a metal precursor [3, 4]. The formation of the metal particles onto support takes place under heating in reductive or oxidative atmosphere, often named calcination. Thus, a broad size distribution will be formed. The difficulties of this method include the reproducibility of the catalyst preparation, because the metal particles are formed in the presence of the support, so that metal morphology and dispersion are strongly affected by the nature and surface structure of the support. Nevertheless, this method was widely used because of its low cost and simplicity [3, 4]. Another method which could be used to prepare heterogeneous supported catalysts is the deposition of pre-formed metal nanoparticles onto different supports. This method promises a much higher control of the particle size with narrow size distribution and morphology independent on the used support [96]. It provides the opportunity to study the influence of the support on the catalytic reaction isolated from the other factors [7, 8, 97]. Different methods to deposit pre-formed metallic nanoparticles are known, such as direct colloidal deposition, colloidal deposition by surface modification, via ion exchange, using flame spraying techniques, and Langmuir-Blodgett techniques [5].

The support could e.g. create additional active sites which might lead to bi-functional catalysts (e.g. by oxygen vacancies), increase the mechanical resistance, stabilize the metal particle size against alteration in the structure and the shape of the metal nanoparticles, increase the metal dispersion due to its high surface area, transfer charge from/to the metal nanoparticle, and adsorb intermediate reaction species [98, 99].

Different types of support have been used in heterogeneous catalysis including transition metal oxides, silica, zeolite, activated carbon, pillared clays, red mud, polymers, and black carbon [100]. Carbon supports are very important in catalysis and are often used because of their high surface area and chemical inertness (i.e. having little or no ability to react).

However, the low reactivity of the carbon surface makes it difficult to deposit metals on it. Therefore, pre-treatment of the carbon support in oxidizing environment is recommended to introduce oxygen containing surface groups, thus enhancing the interaction with the metal [100]. Supporting materials made of metal oxides do not require this pre-treatment and are therefore beneficial in that respect.

2.1.6 Catalyst deactivation

The critical issue in industrial catalytic processes is the loss of the catalytic performance (activity and/or selectivity) during the reaction [101]. Several studies were focused on the reasons of catalyst deactivation [102]. In particular, in the case of liquid-phase oxidation of alcohols, four major reasons were found to be responsible for the deactivation of the catalyst.

- Oxygen poisoning

This phenomenon refers to blocking of surface by strongly adsorbed oxygen species. This could happen when a high amount of oxygen is introduced. This effect is also known as “over-oxidation” and could be classified as irreversible deactivation [103].

- Chemical poisoning

The catalyst could be poisoned or deactivated by the adsorption of the substrate, reaction intermediates or/and by-products which could be formed during the reaction on the active sites of the catalyst. Chemical poisoning is classified as reversible deactivation because the adsorbed products on the catalyst might be removed via washing of the catalyst [103].

- Leaching

The term leaching refers to the loss of the active metal species by migration into liquid phase. Leaching is an irreversible deactivation. Different factors could affect the amount of metal leaching e.g. high pH values. Noteworthy, metal leaching could be avoided or at least minimized by adding a second metal as promoter [104]

- Sintering

The term sintering refers to a loss of the active surface resulting from agglomeration and coalescence of small particles [104]. Sintering is classified as irreversible deactivation and could occur for supported and unsupported metal catalysts. Different factors could lead to an acceleration of this phenomenon e.g. high temperature.

2.1.7 Removal of linear polymer stabilizers from supported catalyst

As already stated in section 2.1.2, stabilizers prevent nanoparticles from aggregation during synthesis but can reduce their catalytic activity by blocking the active sites at the same time. Therefore, different methods were developed to remove the stabilizer from the catalyst surface (Table 1). Treatment with hot water was performed on a PVA stabilized Au/TiO_2 catalyst (Entry 1, Table 1). Various analytical techniques showed that PVA was partially removed and a slight increase of the particles size was observed depending on the treatment time [105]. UV-ozone was utilized to remove the capping agent PVP from Pt nanoparticles (Entry 2, Table 1). Various analytical techniques confirmed the absence of PVP as well as a change in shape and spatial distribution of the nanoparticles [106]. Different solution mixtures were reported to remove the capping agent PVP by washing the catalytic material several times with a mixture of ethanol and *n*-hexane followed by heating (Entry 3, Table 1) [107] or with a mixture of H_2O_2/H_2SO_4 (Entry 4, Table 1) [108]. Furthermore, calcination procedures [109, 110] as well as treatment with UV/H_2O_2 [111] were developed for this purpose (Entries 5-7, Table 1). Plasma treatment was also investigated as method to remove the PVP stabilized Pt NPs (Entry 8, Table 1) [112].

Table 1. Selected methods for removing PVP from supported catalysts.

Entry	Stabilizer	Metal	Method	Ref.
1	PVA	Au	reflux in water	[105]
2	PVP	Pt	UV-ozone	[106]
3	PVP	Pt	washing by (EtOH: *n*-hexane) and then heating at 300 °C	[107]
4	PVP	Pt	washing by H_2O_2:H_2SO_4	[108]
5	PVP	Au/Pd	calcination (oxidation at 400 °C and reduction at 200 °C)	[109]
6	PVP	Pt	calcination (oxidation and reduction at 200 °C)	[110]
7	PVP	-	UV-H_2O_2	[111]
8	PVP	Pt	Plasma treatment	[112]

2.2 Catalytic selective liquid phase oxidation

2.2.1 Selective oxidation of 5-hydroxymethylfurfural

5-Hydroxymethylfurfural (HMF) is an essential chemical because it is a versatile building block and potential availability from carbohydrates by acid catalyzed dehydration of carbohydrates e.g. fructose or glucose (Scheme 2) [9-12].

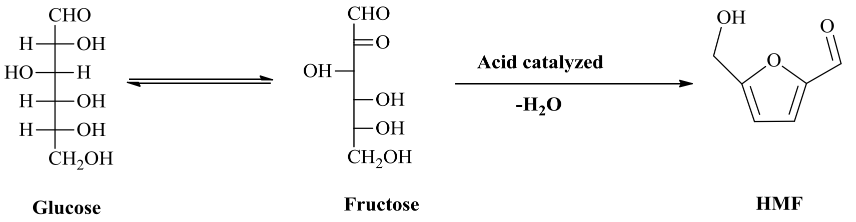

Scheme 2. Synthesis of 5-hydroxymethylfurfural (HMF) [113].

5-Hydroxymethylfurfural is considered as platform building block and, after its reduction or oxidation, as a potential starting material for several industrial applications [114]. 2,5-Furandicarboxylic acid (FDCA, Scheme 3) which can be formed by oxidation of HMF, is considered as one of the twelve most potentially useful biomass derived chemicals [13], and might be used as a renewable intermediate for polymers, fine chemicals, pharmaceuticals and agrochemicals [14]. In this reaction, 5-hydroxymethyl-furan-2-carboxylic acid (HMFCA) and 5-formyl-furan-2-carboxylic acid (FFCA) could occur as intermediates (Scheme 3).

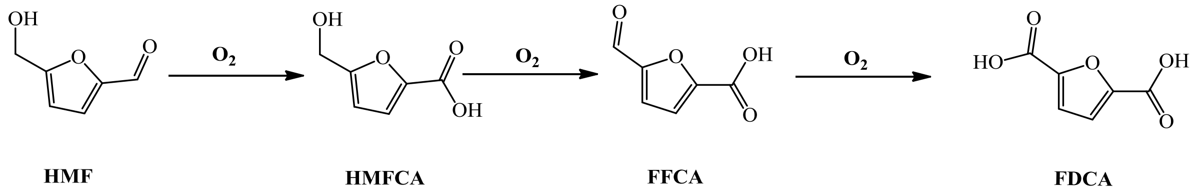

Scheme 3. Formal reaction scheme of the aerobic HMF oxidation in presence of base [115].

A main disadvantage of this reaction is the necessity of a base in the reaction mixture. The base plays an essential role in deprotonating the alcohol group and preventing the deactivation of the catalyst by adsorption of 2,5-furandicarboxylic acid (FDCA) because FDCA is hardly soluble in base-free aqueous solution [116]. However, at the same time the substrate HMF is highly instable in water at high pH values, i.e. in the presence of a base [117]. Under these conditions, HMF undergoes several side reactions involving ring opening to form products like levulinic acid and formic acid. Those HMF degradation products lead to the formation humins type products [118].

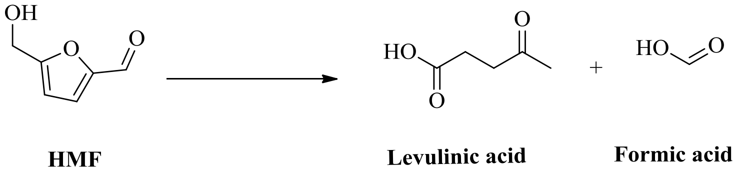

Scheme 4. HMF degradation pathway [119].

Previously, the selective oxidation of HMF to FDCA was studied using a stoichiometric oxidant like $KMnO_4$ [120], highly polluting catalysts such as Pb catalyst [121] and homogeneous metal salts such as Co/Mn/Br at high pressure (70 bar air) [122]. Heterogeneous catalysts were also applied for the selective oxidation of HMF using molecular oxygen. The influence of the molar ratio HMF/metal, temperatures, and oxygen pressures were reported with and without the addition of homogeneous base.

Reported conditions and FDCA yield for oxidation of HMF on monometallic catalysts in the presence of homogenous base are summarized in Table 2.

Davis et al. [23] have compared reaction rate and product distribution over the supported metal catalyst Pd/C, Pt/C, Au/C, and Au/TiO_2 (Entry 1). Compared to the Pd and Pt materials, the gold catalysts showed a reaction rate an order of magnitude higher under the given reaction conditions (6.9 bar O_2, room temperature). However, here, the major product was HMFCA while Pt and Pd delivered FDCA as major product. The authors reported that a higher base concentration (OH^-) and oxygen pressure was required to improve the selectivity of the gold catalysts towards the desired product FDCA.

Gorbanev et al. [116] reported the selective oxidation of HMF to FDCA over Au/TiO_2 at room temperature. Increasing oxygen pressure from 10 to 20 bar enhanced the yield of FDCA up to 71 % at full conversion of HMF. Here, about 4 % leaching of gold species was detected and hence a decrease of the conversion by 5 to 10 % was observed in the recycle experiments.

Casanova et al. studied differently supported gold catalysts, such as Au/TiO_2, Au/CeO_2, Au/C, and Au/FeO_2 [123]. Among the catalysts mentioned, the best results were obtained for Au/CeO_2 (96 % yield of FDCA at full HMF conversion, Entry 3). Furthermore, the recyclability of the catalyst was successful only when the oxidation reaction was performed at room temperature for 4h. During this time, all HMF was converted to HMFCA and HMF degradation was avoided and then increasing the temperature up to 130 °C was necessary to oxidize HMFCA further to FDCA. In this way the catalyst was reusable three times, otherwise the catalyst will be deactivated by blocking of active sites by HMF degradation products in the initial stage. However, a significant decrease of the FDCA yield to 81 % was observed in the 4th run.

Table 2. Reported conditions and yield of FDCA in HMF oxidation over monometallic catalysts in presence of base.

Entry	Catalyst	FDCA Y[%]	HMF:Cat [mol:mol]	Base:HMF [mol:mol]	T [°C]	t [h]	pO_2 [bar]	HMF [M]	Ref.
1	Pd/C	79	150:1	2:1	25	6	6.9	0.15	[23]
2	Au/TiO_2	71	100:1	4:1	30	18	20	0.10	[116]
3	Au/CeO_2	96	640:1	4:1	130	7	10[1]	0.15	[123]

[1] **air, water as solvent, ≥99 % HMF conversion.**

Bimetallic catalysts were also used in the selective oxidation of HMF to FDCA with addition of homogeneous base (Table 3).

Pasini et al. [119] have reported the HMF oxidation of on an $Au\text{-}Cu/TiO_2$ catalyst (Entry 1). This bimetallic catalyst showed higher activity, better stability and resistance against poisoning compared to their monometallic counterparts, which was attributed to a strong synergistic effect (Entry 1). In the recycling experiments, a fast deactivation of the Au/TiO_2 catalyst was observed. The authors stated that the monometallic catalyst had lost oxidative activity quickly and after the second run it was totally poisoned and started to polymerize rather than oxidize the reactants. In contrast, the bimetallic $Au\text{-}Cu/TiO_2$ catalyst was reused 5 times without losing activity but with a slight decrease of FDCA yield. Thus, the bimetallic catalyst remained catalytically active because of the presence of the second metal (copper) in the active phase.

Ait Rass et al. [124] have reported the selective oxidation of HMF over a Pt-Bi/C catalyst (Entry 2). The presence of bismuth (Bi) as promoter in the catalyst prevented the Pt catalyst from deactivation (oxygen poisoning). In addition, the group studied the nature of base by keeping the pH of the reaction solution constant. The authors stated that by using Na_2CO_3 the activity clearly increased compared to using $NaHCO_3$ while strong HMF degradation was detected when NaOH was employed.

Table 3. Reported conditions and yield of FDCA in HMF oxidation over bimetallic catalyst in presence of base.

Entry	Catalyst	FDCA Y [%]	HMF:Cat [mol:mol]	Base:HMF [mol:mol]	T [°C]	t [h]	pO_2 [bar]	HMF [M]	Ref.
1	$Au\text{-}Cu/TiO_2$	99	100:1	4:1	95	4	10	0.1	[119]
2	Pt-Bi/C	99	100:1	2:1	100	3	40[1]	0.1	[124]

[1] air, water as solvent, ≥99 % HMF conversion.

Table 4 summarizes reported conditions and FDCA yield in the oxidation of HMF without the addition of a base.

Gupta et al. [125] used differently supported gold catalysts, such as Au/HT, Au/Al_2O_3, Au/C and Au/SiO_2 (Entry 1, Table 4). Hydrotalcite (HT, $[Mg_{8-x}Al_x\ (OH)_{16}(CO_3^{2-})].nH_2O$) is considered to be a basic support and among these catalysts Au/HT delivered the highest yield of FDCA (99 %) at full conversion. Even though leaching of gold was not detected, a slight decrease of the FDCA yield was observed in consecutive runs (from 99 % in first run to 90 % in third run).

Gorbanev et al. [126] have reported a number of catalysts based on $Ru(OH)_x$ in the TiO_2, Al_2O_3, Fe_3O_4, ZrO_2, and CeO_2. The best result was obtained using CeO_2 as support (Entry 2, Table 4). Additionally, the catalyst was reusable. Magnesium-based carrier materials [spinel ($MgAl_2O_4$), magnesium oxide (MgO) and hydrotalcite (HT)] were also studied in the HMF oxidation by Gorbanev et al. [127]. High yields of FDCA were achieved with $Ru(OH)_x$ containing catalysts on HT and MgO (99 and 87 %, respectively) whereas the spinel ($MgAl_2O_4$) supported catalyst delivered only 38 % yield of FDCA after 6 h. However, compared to the spinel material the HT and MgO catalysts turned out to be less stable due to leaching of Mg ions into the solution. Here, the authors stated that the stability of HT observed by Gupta et al. (Entry 1, Table 4) is due to the mild reaction conditions (ambient oxygen pressure and elevated temperature).

Generally, the advantage of using metal species supported on basic materials is to produce carboxylic acids rather than their salts form, which is beneficial in economic and environmental aspects [125, 128].

Table 4. Reported conditions and yield of FDCA in HMF oxidation over monometallic catalysts without addition of base.

Entry	Catalyst	FDCA Y [%]	HMF:Cat [mol/mol]	T [°C]	t [h]	pO_2 [bar]	HMF [M]	Ref.
1	Au/HT	99	40:1	95	7	50[1]	0.16	[125]
2	$Ru(OH)_x/CeO_2$	36	20:1	140	6	2.5	0.05	[126]
3	$Ru(OH)_x$/HT	99	20:1	140	6	2.5	0.05	[127]

[1] mL/min, water as solvent, ≥99 % HMF conversion.

Davis et al. [129] have reported oxidation steps for the selective oxidation of HMF in the presence of base on supported Pt and Au catalysts utilizing the isotopically-labeled $^{18}O_2$ and $H_2{}^{18}O$ to investigate the source of the oxygen in the products (Scheme 5).

However, the first step involved a reversible hydration of the aldehyde group of HMF to a germinal diol via nucleophilic attack of hydroxide ions (OH^-) to the carbonyl group and then the proton will be transferred from the water to the formed alkoxy ion intermediate. The second step involved the dehydrogenation of the formed germinal diol intermediate, aided by the hydroxide ions (OH^-) adsorbed on the metal surface, to form the carboxylic acid product (5-hydroxymethyl-furan-2-carboxylic acid, HMFCA) which is present as carboxylate in alkaline solution. Here, two water molecules and two electrons were produced where the electrons are deposited on the metal surface of the catalyst. In third step, an alkoxy intermediates is formed after the deprotonation of the alcohol group by hydroxide ion. Then, the alkoxy intermediate reacts to the aldehyde, formally by loss of hydride. Two water molecules and two additional electrons were produced in the step 3. The fourth step involved a reversible hydration of the aldehyde to the germinal diol (as occurred in the step 1). In the fifth step involved the dehydrogenation of the formed germinal diol, aided by the hydroxide ion adsorbed on the metal surface catalyst, to produce the carboxylic acid (2,5-furandicarboxylic acid, FDCA), which is present as carboxylate in alkaline solution, with liberating two electrons and two water molecules. However, six electrons were produced during this mechanism and deposited on the metal surface of the catalyst. The results showed that $^{18}O_2$ atoms were incorporated in HMFCA and FDCA products when the oxidation is performed in $H_2{}^{18}O$. It was stated that the water employed as oxygen source. The oxygen is not involved in this mechanism because it was found that the oxygen served as electron scavenger on the metal, thereby closing the catalytic cycle [129].

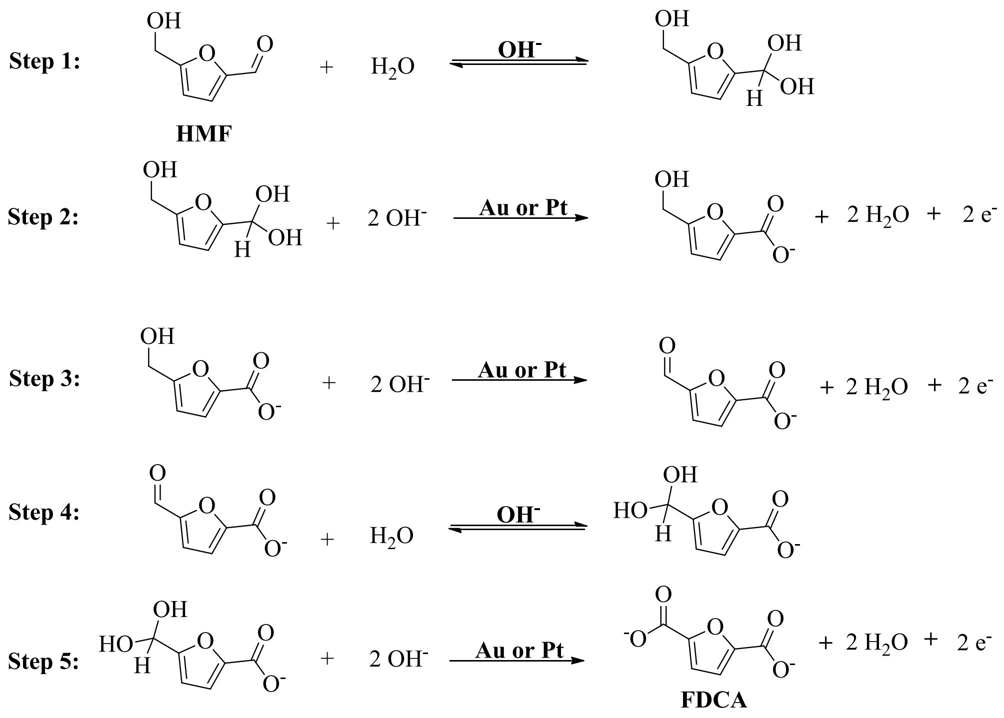

Scheme 5. Oxidation steps for HMF oxidation in alkaline aqueous solution on Pt or Au catalysts [129].

2.2.2 Selective oxidation of glycerol

Up to now, the production of energy is mostly dependent on crude oil [130]. Renewable energy has attracted a significant interest with the depletion of petroleum reserves. Biodiesel is a substitutional diesel fuel, which is derived from biological sources e.g. vegetable oil or animal fat [131, 132]. Crude glycerol is an essential by-product of biodiesel formation in the trans-esterification process of glyceride (Scheme 6) [15].

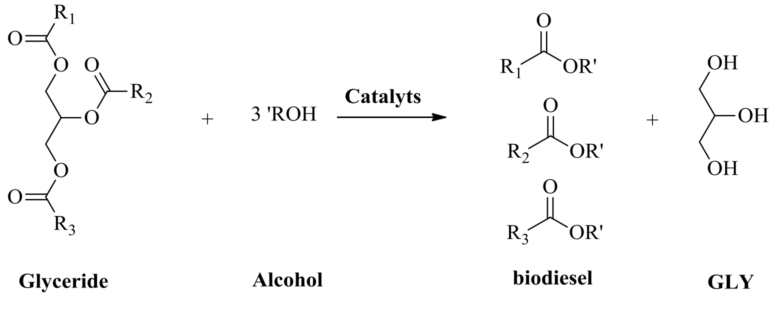

Scheme 6. Production of glycerol [131].

Glycerol (GLY) is a versatile multifunctional molecule and can undergo a manifold of reactions, such as hydrogenolysis [133], dehydration [134], pyrolysis [135], transterification esterification [136, 137], etherification [138], oligomerization [139], polymerization [140], carboxylation [141] and oxidation.

Scheme 7 shows general reaction pathways of the glycerol oxidation. It becomes obvious that the oxidation of glycerol can follow multiple routs. Oxidation of the primary alcohol group of glycerol forms glyceraldehyde (GLYHD) which can be oxidized to glyceric acid (GLYA). Further oxidation delivers tartonic acid (TA). Oxidation of the secondary alcohol group of glycerol leads to dihydroxyacetone (DHA). Further oxidation delivers hydroxypyruvic acid (HPA). Glyceraldehyde undergoes isomerization to dihydroxyacetone in alkaline aqueous solution. DHA and GLYHD can also be converted to lactic acid by dehydration and subsequent 1,2-hydride shift of the keto-enol tautomerization intermediates. Additionally, C-C cleavage can occur during glycerol oxidation to form C-2 and C-1 products, such as glycolic acid (GOA), oxalic acid (OXA), acetic acid (AA), formic acid (FA), CO and CO_2.

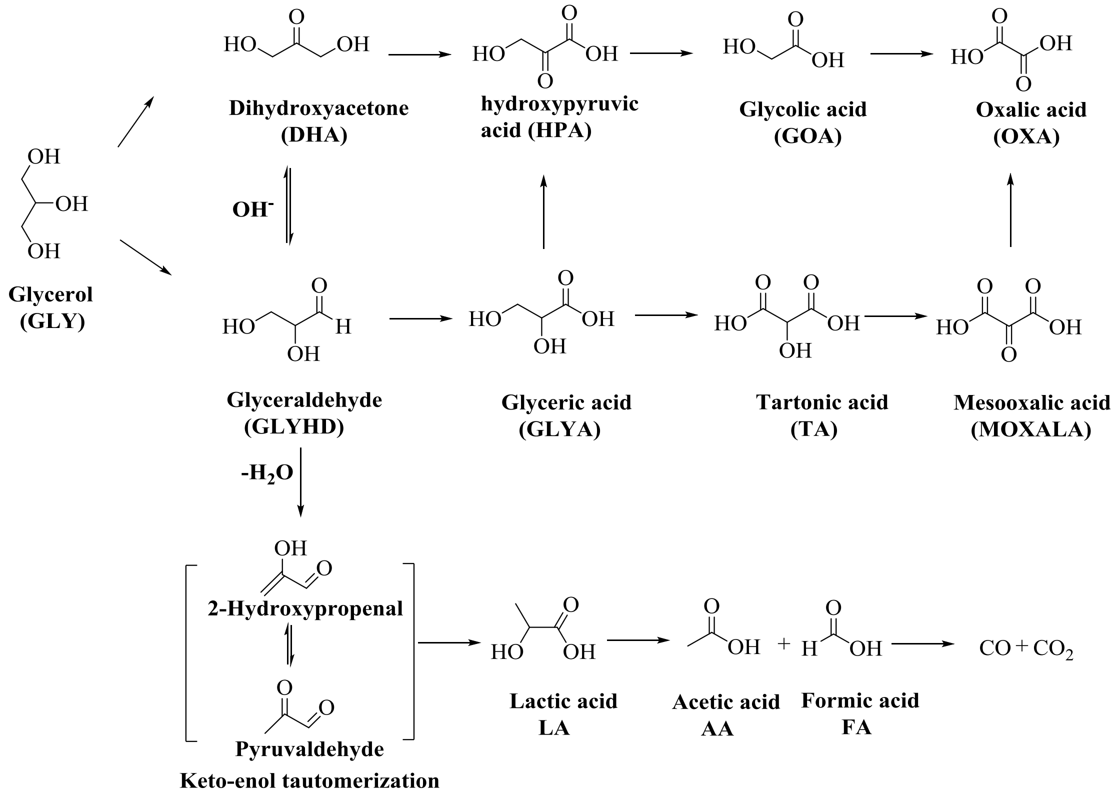

Scheme 7. Proposed pathways of glycerol conversion [30, 32, 35].

The mechanism of glycerol oxidation to glyceric acid was proposed by Zope et al [142]. The group investigated the oxidation using gold and platinum catalysts and labeled oxygen ($^{18}O_2$) and water ($H_2{}^{18}O$) in presence of base. They stated that O_2 did not play a role in the mechanism which is consistent with HMF oxidation mechanism described above. The unlabeled glyceric acid was formed when $^{18}O_2$ was used while the ^{18}O atom was detected in the product when the oxidation was performed in $H_2{}^{18}O$.

The role of molecular oxygen in the catalytic cycle was to regenerate the hydroxide ion rather than produce atomic oxygen by dissociation. Scheme 8 represents the role of O_2 in the oxidation of glycerol where (*) is a site of the metal surface of the catalyst. The first step is the reduction of the molecular oxygen. This step regenerates the hydroxide ions. Step 2 is involved the disproportionation of the peroxide into atomic oxygen and hydroxide on the surface of the metal catalyst. In the third step, the adsorbed peroxide on the metal surface could react with water on the metal surface of the catalyst to produce hydrogen peroxide and hydroxide. The forth step is the decomposition of hydrogen peroxide on the metal surface of the catalyst. The fifth step closes of the catalytic cycle by scavenging the electrons from the metal surface through the reaction between the adsorbed hydroxide with any metal hydrides found on the metal surface (step 5). However, the role of oxygen is essentially the scavenging of electrons deposited onto the metal surface of the catalyst, oxidizing metal-hydride bonds and OH^- regeneration [142].

Step 1: $O_2^* + H_2O^* \longrightarrow OOH^* + HO^*$

Step 2: $OOH^* + * \longrightarrow O^* + HO^*$

Step 3: $OOH^* + H_2O^* \longrightarrow H_2O_2^* + HO^*$

Step 4: $H_2O_2^* + * \longrightarrow OH^* + HO^*$

Step 5: $OH^* + H^* \longrightarrow H_2O^* + *$

Scheme 8. The role of oxygen in glycerol oxidation [142].

2.2.2.1 Selective oxidation of glycerol to dihydroxyacetone

Dihydrxoyacetone (DHA) is one of the products that can be obtained by selective oxidation of glycerol. DHA is considered as an important product due to its application in cosmetics, especially as an active ingredient in sunless tanners.

Synthesis of DHA from oxidation of glycerol was performed using mono- and bimetallic catalysts applying different reaction conditions (Table 5)

The production of DHA by oxidation of GLY was reported without addition of base on e.g. an alloyed Pd-Ag/carbon (Entry 1) or a Pt-Sb/MWCNT (Entry 2) catalysts [80]. The studies revealed that compared to monometallic Pd/C the glycerol conversion was significantly increased upon utilization of the bimetallic catalyst Pd-Ag/C (Table 5, Entry 1). It is assumed that Ag prevents the deactivation of the active Pd catalyst. Additionally, the author found that selective oxidation to DHA was possible with Pd-Ag on metal oxides, such as TiO_2. However, this catalyst was less selective than Pd-Ag on carbon. In the recycling experiments, a decrease in the activity was observed but the selectivity toward DHA stayed almost unchanged [80].

The Pt-Sb/MWCNT was more active and selective toward DHA compared to Pt-Bi/MWCNT and Pt/MWCNT catalysts. Moreover, the C-C cleavage products were clearly minimized on Pt-Sb/MWCNT catalyst. The differences in the catalytic behavior of the prepared catalysts were attributed to the structure and morphology of the catalysts. Where the antimony (Sb) was homogenously incorporated into the lattice of Pt an alloy structure of Sb and Pt catalyst was formed. In contrast, the Pt particles were wrapped in a layer of $Bi_2O_2CO_3$ in a Pt-Bi catalyst. In the recycling experiments on Pt-Sb/MWCNT, the activity was slightly decreased in the fifth cycle but the selectivity toward DHA remained unchanged in all runs [143].

Interestingly, the DHA could be produced from oxidation of GLY in acidic media (pH was adjusted to 2 by addition of HCl) on Pt-Bi/C catalyst (Entry 3,Table 5) [144]. The bimetallic catalyst was optimized in terms of Pt/Bi ratio on various supports. The optimized composition was 3 % Pt-0.6 % Bi supported on charcoal [144].

In other studies it was found, that the presence of base to form DHA from GLY oxidation is necessary on e.g. a monometallic Au/MWCNT (Entry 4) or an alloyed Au-Pt/C catalyst (Entry 5). The monometallic Au supported on AC (activated carbon) delivered glyceric acid as main product while using Multi-walled carbon nanotubes as support led to produce DHA as main product under the same reaction conditions (Entry 4). Hence, the type of support affected the products distributions [145]. A platinum promoted gold catalyst delivered an enhanced DHA selectivity (36 %) compared to that achieved with a monometallic Au catalyst (26 %) at a conversion of 50 % (Entry 5) [146].

Table 5. Reported conditions and selectivity of DHA in GLY oxidation.

Entry	Catalyst	GLY X [%]	DHA S [%]	GLY:Cat [mol/mol]	Base:GLY [mol/mol]	t [h]	pO_2 [bar]	GLY [M]	Ref.
1	Pd-Ag/C	52	84	500:1	base-free	24	3	0.5	[80]
2	Pt-Sb/ MWCNT	90	51.4	-	base-free	2	150[2]	1	[143]
3	Pt-Bi/C	80	60	-	pH= 2	8	3	1	[144]
4	Au/ MWCNT	50	60	-	2:1	-	3	0.3	[145]
5	Au-Pt/C	50	36	2460:1	pH =12	6	10	1.5	[146]

[2] mL/min, as the reaction temperature of 80 °C for (Entries 1 and 4) and 60 °C (Entries 2-3, and 5).

2.2.2.2 Selective oxidation of glycerol to glyceric acid

Glyceric acid (GLYA) is also an essential product that can be obtained by GLY oxidation. It serves as an intermediate for further oxidation products such as tartonic acid (TA, Scheme 7) and mesoxalic acid (MOXA). The formation of glyceric acid from glycerol was widely studied using different catalysts at various reaction conditions with and without addition of base. Table 6 summarizes the reported conditions and GLYA selectivity for the oxidation of glycerol to glyceric acid.

The production of GLYA from oxidation of GLY was reported without base addition on e.g. a Pt/HT (Entry 1), an Au (core)-Pt (shell)/MgO (Entry 2), Pt/MWNTs (Entry 3), Pt/C (Entry 4), or Au-Pt/H-mordenite (Entry 5).

The Pt/HT catalyst showed a high selectivity for the reaction to glyceric acid (Entry 1). The activity of the catalyst was greatly affected by the Mg/Al ratio of the supporting material where an increasing activity was observed at increasing molar ratios of Mg/Al in the hydrotalcite [147]. Even though the Au(core)-Pt(shell)/MgO catalyst exhibited the same particle size and structure compared to Au(core)-Pd(shell)/MgO but it turned out to be more active and selective toward glyceric acid (Entry 2). The reusability tests on Au-Pt/MgO catalyst showed a decrease in the activity and GLYA selectivity as well [31].

The production of GLYA in base-free solution was not only achieved with the catalyst containing basic support but also using carbon as support (Entries 3-4).

In particular, Gao et al. [148] compared a Pt on activated carbon and multi walled carbon nanotubes under base–free conditions at 60 °C. The Pt/MWNTs catalyst was more active and selective due to easier accessibility of the active Pt sites on the external wall of the support (Entry 3). In contrast, the study reported by Liang et al. showed the possibility of having a high selectively for the reaction to glyceric acid, by optimization of the particle size of catalyst (Entry 4). The author prepared differently sized carbon supported platinum nanoparticles in the range of 1.2 to 26.5 nm. It was found that Pt NPs with a size of less than 6 nm were more active and selective with a good recyclability compared to particles >10 nm [149].

Villa et al. [150] studied the influence of the support on the glycerol oxidation in base free aqueous solution. The alloyed Au-Pt on an acidic support (H-mordenite) showed better activity and selectivity toward glyceric acid comparable with another support e.g. activated carbon, TiO_2, or $MgAl_2O_4$. Moreover, the C-1 products (e.g. formic acid, CO_2, and CO) were also minimized (Entry 5).

The production of GLY from oxidation of GLY was reported with base addition on e.g. an Au/charcoal (Entry 6), Au/TiO_2 (Entries 7 and 8), Au-Pt catalyst/C (Entry 9), or Pd/C (Entry 10). No conversion of GLY on the Au/charcoal was observed in the absence of base. Thus, a molar ratio of NaOH to GLY (1:1) was required to perform the oxidation reaction efficiently (Entry 6). Additionally, it was found that the reaction rate is depended on the oxygen pressure where higher glycerol conversions were obtained at higher oxygen pressures [151].

The influence of the reactor configuration on the glycerol oxidation on an Au/TiO_2 using a 2:1 molar ratio of NaOH to GLY was studied by Zope et al. (Entry 7) [128]. The product distribution depended on the reactor system, due to the differences in the contact between gas, liquid and solid. A substantial amount of tartonic acid (TA) and oxalic acid (OXA) were detected in fixed bed system compared with batch reactor. Entry 7 in Table 6 shows results from the batch experiment [128].

Dimitratos et al. [152] studied the effect of the synthetic method (deposition-precipitation versus sol immobilization method) and reduction method (calcination versus chemical reduction) on the catalytic activity of Au/TiO_2 materials in the glycerol oxidation using a 4:1 molar ratio of NaOH to GLY. It was reported that the catalytic activity depends on the choice of the reduction method and the type of protecting agent (PVA, THPC) during Au NPs synthesis. The highest activity was obtained with Au/TiO_2 prepared at low temperatures during chemical reduction by deposition-precipitation (Entry 8).

Bianchi et al. [29] compared the catalytic performance of mono- and alloyed bimetallic catalysts based on Au, Pd and Pt supported on carbon at a higher molar ratio of NaOH to GLY (4:1). The bimetallic catalyst showed better catalytic results compared to the monometallic materials. Particularly, an Au-Pd catalyst was more selective towards glyceric acid than an Au-Pt catalyst (Entry 9).

Garcia et al. [26] studied the effect of the pH value over different metal catalysts (Entry 10). A selectivity of 70 % towards glyceric acid was achieved at a complete conversion on Pd/C at a pH value of 11. Pt/C delivered only 55 % selectivity towards the desired product under the given reaction conditions.

Table 6. Reported conditions and selectivity of GLYA in GLY oxidation.

Entry	Catalyst	GLY X [%]	GLYA S [%]	GLY:Cat [mol/mol]	Base:GLY [mol/mol]	t [h]	pO_2 [bar]	GLY [M]	Ref.
1	Pt/HT	55	78	800:1	base-free	6	10^1	0.1	[147]
2	Au-Pt/MgO	42	85	500:1	base-free	2	3	0.3	[31]
3	Pt/ MWCNT	70	69	450:1	base-free	-	150^1	1	[148]
4	Pt/C	50	47	-	base-free	6	150^1	1	[149]
5	Au-Pt/H-mordenite	70	83	500:1	base-free	8	3	0.3	[150]
6	Au/ charcoal	56	100	538:1	1:1	3	3	1	[151]
7	Au/TiO_2	83	61	8000:1	2:1	3	11	0.3	[128]
8	Au/TiO_2	50	81	500:1	4:1	-	3	0.3	[152]
9	Au-Pd/C	90	69	500:1	4:1	3	3	0.3	[29]
10	Pd/C	100	70	-	pH=11	4	1	1	[26]

[1] mL/min, water as solvent, as the reaction temperature of 60 °C for (Entries 1- 2, 5- 6 and 9- 10), 23 °C for (Entry 3), 100 °C (Entry 4), 50 °C (Entry 7), and 30 °C (Entry 8).

2.2.2.3 Selective oxidation of glycerol to lactic acid

Lactic acid (LA, 2-hydroxy propionic acid, Scheme 7) is considered as an important platform chemical in many applications in the food, cosmetic, and pharmaceutical industries [16].

Various approaches were applied to synthesize lactic acid, involving hydrothermal methods [153-155], hydrogenolysis [156], chemical fermentation routes [157-159], and selective oxidation [32-35]. Selective oxidation allows the reaction to proceed under mild reaction conditions in contrast to hydrothermal and hydrogenolysis methods.

The synthesis of LA by selective oxidation of GLY is rather challenging due to the glyceraldehyde (GLYHD) intermediate and its isomer dihydroxyacetone (DHA) (Scheme 7), which are sensitive to further oxidation. In many cases primarily glyceric acid (GLYA) is formed without any significant formation of lactic acid (LA) [148]. Table 7 summarizes reported conditions and LA selectivity for the oxidation of GLY.

A high LA selectivity of ≥ 80 at approximately full conversion was obtained using a high molar ratio of NaOH to GLY (4:1) on Au-Pt/TiO_2 (Entry 1), Au-Pt/CeO_2 (Entry 2) and Au/CeO_2 (Entry 3).

The bimetallic catalyst Au-Pt/TiO_2 (Entry1) showed a superior stability during the recycling experiments compared to monometallic counterparts (Au or Pt). It was stated that the interaction of Au with Pt avoided the agglomeration of Au particles and the poisoning of Pt site by oxygen as well [32]. The reusability of the catalyst Au-Pt/CeO_2 (Entry 2) or Au/CeO_2 (Entry 3) was successfully demonstrated four times without significant loss in the LA selectivity.

Recently, the formation of lactic acid (LA) by selective oxidation of glycerol was investigated under acidic conditions (Lewis acid, $AlCl_3$) on Au-Pd/TiO_2 (Entry 4). The Au-Pd/TiO_2 catalyst gave a very low GLY conversion and LA selectivity connected with the formation of large amount of CO_2. When $AlCl_3$ was present, GLY conversion and LA selectivity was improved. At the same time small amounts of CO_2 were formed. It was stated that the synergistic roles between the Lewis acid ($AlCl_3$) and Au-Pd/TiO_2 had an influence on the formation of lactic acid (LA) [35].

Table 7. Reported conditions and selectivity of LA in GLY oxidation.

Entry	Catalyst	GLY X [%]	LA S [%]	GLY:Cat [mol/mol]	T [°C]	t [h]	pO_2 [bar]	GLY [M]	Ref.
1	Au-Pt/TiO_2	99	85.3	-[3]	90	-	1	0.2	[32]
2	Au-Pt/CeO_2	98	80	680:1	90	3.5	5	0.17	[33]
3	Au/CeO_2	99	83	-	100	-	150[1]	-	[34]
4	Au-Pd/TiO_2[2]	13.6	66.6	2500:1	160	2	10	1	[35]

Water was used as solvent and the NaOH:GLY =4:1 mol:mol for all data, [1] mL/min air, [2] 10 mM $AlCl_3$. [3] $2.5•10^{-3}$ mmol.

However, the selective oxidation of HMF or GLY isn’t yet industrially applicable for many reasons. One of the major difficulties is that highly active and selective catalysts, which at the same time show a high stability, remain elusive. Furthermore, despite base is often necessary in the reaction mixtures, it isn’t favored economically and environmentally. Without base, the reaction usually proceeds slowly or might not at all. In some cases, the oxidation reactions were performed in base-free solution by using e.g. a high amount of catalyst, but this process isn't economically favored. As supports, carbon and basic supports were mostly used, when oxidation reactions were performed in base-free solution. The stability of a basic support in aqueous solution is also considered as challenge. Thus, the aim of this work is to provide a better understanding of single steps in the development of supported catalysts with pre-formed palladium nanoparticles in order to obtain active and selective catalysts for these oxidation reactions in aqueous solution and study their stability in this medium.

3. Characterization

Many characterization techniques were used to characterize the catalysts such as the X-ray diffraction (XRD), transmission electron microscopy (TEM), scanning electron microscopy (SEM), small angel X-ray scattering (SAXS), X-ray photoelectron spectroscopy (XPS), BET measurement, and UV- visible spectroscopy (UV-Vis). The basic principle of each technique briefly explained as the following:

3.1 Powder X-ray diffraction

Powder X-ray diffraction (XRD) analysis gives information about the phase composition, the crystallinity and the mean crystallite size of the NPs.

The X-ray was first discovered by Wilhelm Roentgen in 1895. Much later on in 1912, Max von Laue has discovered the X-ray diffraction [160]. The generation of X-rays occurs by heating the filament in a cathode ray tube. The X-rays will be filtered using an X-ray filter in order to produce monochromatic radiation and then collimated to one trend before hitting the specimen. The wavelength of the X-ray radiation should be in the range of interatomic distances of the crystals. Thereby, X-ray is diffracted on the lattice atoms of the specimen. Depending on the angle a constructive or destructive interference could occur. The occurrence of constructive interference is described according to Bragg law (equation 1).

$$n\lambda = 2\ d \sin\theta \tag{1}$$

This law describes the relation between interplanar spacing d, the diffraction angle θ and the wavelength of the incident X-ray (λ). Comprised of reflex intensity and reflex angle pattern are unique for each crystalline material. The composition of the mixtures of different phases could be determined by using the database. The crystallite size can be calculated from the peak width with the Scherrer formula (equation 2) [161].

$$D = K\lambda/(B\cos\ \theta\,) \tag{2}$$

Where K = the scherrer’s constant, B = the full width at half maximum of the diffraction peak, θ = the diffraction angle and λ = the X-ray wavelength.

3.2 Transmission electron microscopy

Transmission electron microscopy (TEM) provides information about the particle size, shape, chemical composition, and element distribution of samples from biological to organic and inorganic materials including nanoparticles (NPs).

In the transmission electron microscopy, the sample is transmitted by electrons. The source of the electrons mostly is field emission (Schottky emitter or cold field emission) or simple thermal emission (LaB_6 cathode) accelerated by voltage up to 400 kv. This ensures a strong shortening of the wavelength of the electrons, whereby the resolution is much higher than with visible light. Then the electron beam will be parallelized by a condenser lens system, so that the sample is evenly lit. In the sample, a part of the electron is scattered, and this is subjected to the mechanism of Rutherford scattering. Two types of the scattering occur, the elastic (kinetic energy of the electron is the same) and the inelastic (kinetic energy of the electrons decreases). The other part of the electrons passes through the sample without unimpeded. The images or diffraction pattern can be obtained through various lenses and apertures [162]. Currently, the use of scanning methods increasingly gets more importance. Due to Cs-correctors, it is possible to get atomic resolution for high angle annular dark field and annular bright field measurements. These methods give new insight into the field of nanoparticles smaller than 1 nm down to single heavy atoms at supports like those which are used in the catalyst preparation. Atoms with higher electron density and larger sample thickness help to create a greater decrease of the primary beam intensity. In the dark-field mode, the primary beam is not detected by a ring detector or a diaphragm, electrons are used only for imaging [163].

3.3 Scanning electron microscopy

Scanning electron microscopy (SEM) is a powerful technique for studying the surface of the specimen because this technique is capable of providing a better resolution compared to optical microscope. The SEM measurement is based on scattered electrons, which is in contrast to the TEM measurement. In the SEM, the sample is scanned by electrons. The source of these electrons is mostly a tungsten filament or a simple thermal emission Lanthanum hexaboride (LaB_6) accelerated by voltage (e.g. 20 kV). The electron beam will be parallelized by a condenser lens system to produce a thin beam of electrons before scanning the specimen. Different signals will be generated when the electron beam hits the sample. The secondary electron (SE) and backscattered electrons (BSE) are the two signals usually utilized to produce the SEM images. Both signals (SE and BES) could be collected in the case of applying a positive voltage to the collector screen in front of the detector. But in the case of applying a negative voltage, the BSE signal will be only captured because the low energy of SE is rejected. And then the captured electrons are magnified and could be used to produce SEM image [164].

3.4 Small-angle X-ray scattering

Small-angle X-ray scattering (SAXS) analysis provides information about the particle size and size distribution of NPs directly in solution without any pre-treatment. This feature is considered as the major advantage of using SAXS analysis because it makes it possible to avoid any effects on particles size during the pretreatment [165-167]. SAXS analysis is based on elastic collisions. This effect happens due to the interaction between the incident x-ray and specimen and leads the reflected X-ray to be scattered in all orientations. If the reflected X-rays intervene with another one then the constructive interference will occur depending on the angle. The occurrence of the constructive interference could be described by Bragg law [168].

$$\mathrm{n}\,\lambda = 2\ \mathrm{d}\sin\ \theta \tag{3}$$

Where n = any integer, λ = wavelength, d = the vector acting the displacement between reflection sites, θ = the angle between the reflected x-ray and the plane formed by the surface of the material.

In SAXS analysis, the total intensity of the radiation I (q) which is scattered by a dispersion of particles is expressed by:

$$\mathrm{I}\,(\mathrm{q}) = \int D_n\,(R).m^2\,(R).P(q,R).dR \tag{4}$$

Where R = the particle radius, $D_n(R)$ = the number of particles of size R, m(R) = the integral over the excess scattering length density over the surrounding medium of a particle of size R.

$\Delta\rho$ Indicates to the differences between the scattering length of a particle and the matrix and is expressed by:

$$m(R) = \frac{4\pi}{3} R^3 \Delta\rho \tag{5}$$

p (q,R) indicates to the normalized scattered intensity of a single, spherical particle of size R and the shape factor as well. The p (q,R) is formulated as:

$$p(q,R) = \left(\frac{3[\sin(qR) - (qR)\cos(qR)]}{(qR)^3}\right)^2 \tag{6}$$

The q indicates to the scattering vector and is defined in the term of scattering angle (θ) and the wavelength λof the irradiation (equation 7).

$$q = 4\pi\lambda^{-1} . \sin\frac{\theta}{2} \tag{7}$$

The volume weighted distribution function D_v (R) was evaluated according to the equation 8, assuming a spherical shape of particles where R is the radius of a sphere.

$$D_v(\mathrm{R}) = D_n(\mathrm{R}). R^3 \tag{8}$$

3.5 X-ray photoelectron spectroscopy

X-ray photoelectron spectroscopy (XPS) is considered as one of the most common surface analytical techniques. It provides information for the materials in the near-surface region (<20 nm) e.g. oxidation state of the elements and surface composition. XPS could detect the elements which have atomic numbers ≥ 3. X-ray photoelectron spectroscopy (XPS) has a long history. XPS is based on the photoelectric effect which was discovered by Albert Einstein in 1905 [169]. Much later on in 1960, Kai Siegbahn has developed this technique into a useful tool for chemical analysis using high resolution electron spectroscopy. XPS is also known as electron spectroscopy for chemical analysis (ESCA) which was introduced by Kai Siegbahn.

In XPS, the irradiation of the atoms by X-ray causes an emission of electrons, so-called photoelectrons with a certain kinetic energy dependent on their binding energy and the energy of the used X-rays. The kinetic energy is measured by an electrostatic analyzer. The binding energy of the electrons could be calculated by [170]:

$$\mathrm{E_{binding}} = \mathrm{E_{photon}} - (\mathrm{E_{kinetic}} + \emptyset) \tag{9}$$

Where the $\mathrm{E_{binding}}$ = the binding energy of the electron, $\mathrm{E_{photon}}$ = the characteristic energy of X-ray being used, $\mathrm{E_{kinetic}}$ = the kinetic energy of the ejected electron, and $\emptyset$ = the work function.

3.6 BET measurement

BET (Brunauer, Emmett and Teller) is the most common method used to get information about the specific area of a solid. BET theory is based on the physical adsorption of the gas on the solid materials. Commonly, the adsorbate gas is the nitrogen (N_2) [171]. The BET concept is considered as an extension of the Langmuir theory (monolayer) to multilayer adsorption. There are different hypotheses in the BET theory which describe the physical adsorption such as i)- each site of the material has the same nature and could accept one adsorbed molecule, and hence the surface is homogenous, ii)– no interaction between the adsorbed molecules, iii)-the adoption energy is identical for all layers. The BET equation is expressed by [172]:

$$\frac{\mathrm{p}}{(\mathrm{p^0} - \mathrm{p})\,\mathrm{V_a}} = \frac{\mathrm{c}-1}{\mathrm{c\,V_m}}\left(\frac{\mathrm{p}}{\mathrm{p^0}}\right) + \frac{1}{\mathrm{c\,V_m}} \tag{10}$$

Where p = the partial vapour pressure of the adsorbate gas in equilibrium with the surface, p^0 =saturated pressure of adsorbate gas, V_a = the volume of gas adsorbed at standard temperature and pressure, V_m = the volume of gas adsorbed at standard temperature and pressure to form a monolayer on the specimen surface and c = the BET constant, which is formulated as:

$$\mathrm{c} = \exp\frac{\mathrm{E_{1}} - \mathrm{E_2}}{\mathrm{RT}} \tag{11}$$

Where $E_1$and E_2 = the heat of adsorption for first and higher layers, respectively.

The total surface area (SA) is evaluated by:

$$\mathrm{SA} = \mathrm{V_m}\,.\frac{\mathrm{N_A}}{\mathrm{V}}.\,\mathrm{A}_m \tag{12}$$

Where N_A = the Avogadro’s number, V= the molar volume of adsorbent gas and A_m = the cross-sectional area.

The specific surface area SSA (m^2/g) is expressed by:

$$\mathrm{SSA} = \frac{\mathrm{SA}}{\mathrm{a}} \qquad (13)$$

Where (a) indicates the mass of adsorbent.

3.7 UV-Vis spectroscopy

UV-Vis spectroscopy or absorption spectroscopy is widely used in different fields such as nanomaterial science. It provides information about the electronic structure of the nanoparticles [92] and the structure of the bimetallic nanoparticles like an alloy or a core/shell [92, 93].

In the UV-Vis, the interaction of the beam with the sample causes electronic transition from the ground state (low-energy state) to the excited one (high-energy state). The energy difference between the ground state and excited state affects the position of the maximum absorption band and the intensity of the molecules. Additionally, the interaction between the beam and electronic system could affect the intensity of the absorption band.

A convenient expression which connects the absorbance with path length is Lambert-Beer Law. According to this law the concentration of the sample could be calculated by [173] :

$$\log\frac{\mathrm{I}_0}{\mathrm{I}} = \varepsilon \mathrm{cl} \qquad (14)$$

Where I = the intensity of the transmitted radiation, I_0 = the intensity of the incident radiation, ε= the molar absorption coefficient, c = the concentration of absorbing species, l = the path length of the absorbing solution.

A strong and broad band could be detected in the UV-Vis spectra for the metallic nanoparticles (> 2 nm). This called a surface plasmon band (SPB), and it is also known as Mie resonances originated from Gustave Mie who is the most famous in SPB theory. The incoming light interaction with the nanoparticles results in a global scattering. Thus, the surface plasmon band is attributed to the collective electron charge oscillations of the excited metal nanoparticles by light [174]. There are many factors which affect the shape and the intensity of the surface plasmon band such as the electronic interactions between the stabilizing ligands and nanoparticle, the dielectric constant of the surrounding medium, shape, and monodispersity of the NPs. Particles of Au, Ag, or Cu exhibit very clear surface plasmon band in the UV-Vis spectra which usually appears at 250, 385, and 560 nm, respectively [175].

4. Experimental Part

4.1 Materials

Sodium tetrachloropalladate(II) (Na_2PdCl_4, >98 %), polyvinylpyrrolidone (PVP) K30 and gold(III) chloride trihydrate ($HAuCl_4 \cdot 3H_2O$) were purchased from Sigma-Aldrich. Silver nitrate ($AgNO_3$) and ethylene glycol (EG, >99.5 %) were purchased from Merck and Fluka, respectively. Copper (II) chloride anhydrous (>99 %) was purchased from Acros Organics. As supports P25 (TiO_2, Evonik), Pural MG 30, MG 61, MG 70 (Sasol), γ-Al_2O_3 (Alfa Aesar), KF/Al_2O_3 (Sigma-Aldrich) and ZrO_2/La_2O_3 (MEL, 7 wt % La_2O_3) were used. All chemicals were used as received.

4.1.1 Synthesis of polyvinylpyrrolidone protected palladium nanoparticles

Palladium nanoparticles (Pd NPs) were synthesized in a round bottom flask equipped with a reflux-condenser under argon. Sodium tetrachloropalladate (Na_2PdCl_4) and polyvinylpyrrolidone (PVP, monomer unit = 111.4 g/mol) were dissolved in ethylene glycol at room temperature. The Pd salt containing solution was heated up to 90 °C and NaOH dissolved in ethylene glycol (0.5 M) was added quickly. After 3 h at 90 °C with 800 rpm the black solution was cooled and stored at ambient temperature. For the synthesis of Pd_4, the same procedure was applied but the NPs formation was carried out at 25 °C. Here, after 24 h the NPs containing solution was filled up to 25 mL of ethylene glycol. Table 8 summarizes the synthesis parameters of monometallic NPs.

Table 8. Synthesis conditions of Pd NPs.

Entry	NPs	NaOH:Pd mol/mol	PVP:Pd mol/mol	T_1 °C	T_2 °C	[Pd] mM	Time h
1	Pd_1	1:1	3:1	100	90	20	3
2	Pd_2	2:1	3:1	100	90	20	3
3	Pd_3	4:1	3:1	100	90	20	3
4	Pd_4	2:1	3:1	25	25	27.6	24

T_1- temperature of NaOH addition, T_2 – synthesis temperature.

4.1.2 Synthesis of bimetallic nanoparticles starting from pre-formed Pd NPs

To 10 mL of Pd_3 NPs (20 mM) was added 50 mL acetone and centrifuged for 15 min at 3500 rpm. The Pd NPs/PVP precipitation was separated from the mixture by decantation and re-dissolved in 10 mL ethylene glycol adjusted to a pH of 11 by NaOH in EG (0.5 M). To prepare bimetallic nanoparticles an appropriate volume of a 20 mM metal salt dissolved in ethylene glycol ($V_{precursor}$) was added under stirring (800 rpm) by a Hamilton syringe pump with a flow rate of 1 mL/h. Table 9 summarizes the synthesis parameters of bimetallic NPs.

Table 9. Synthesis conditions of bimetallic Pd-M nanoparticles.

Entry	Precursor in EG	$V_{precursor}$	V_{PdNPs}	T	Pd:M (mol:mol)		
	20 mM	mL	mL	°C	10:1	4:1	2:1
1	$HAuCl_4 \cdot 3H_2O$	1	10	25	X		
		2.5				X	
2	$AgNO_3$	1		90	X		
		2.5				X	
		5		90			X
3	$CuCl_2$	1			X		
		2.5				X	

T – Synthesis temperature.

4.1.3 Deposition of mono and bimetallic Pd nanoparticles onto support

For preparation of heterogeneous catalysts with 0.5 wt % Pd loading, 10 mL acetone was added to 2.3 mL of Pd_3 NPs (5.0 mg Pd). The NPs precipitate was separated from the liquid phase by centrifugation (3500 rpm for 10 min), re-dissolved in 10 mL ethanol and added within 1 h under stirring (800 rpm) to a suspension of 0.995 g support in 25 mL ethanol using a syringe pump. Deposition of NPs on the supports ZrO_2/La_2O_3 and KF/Al_2O_3 were realized in 25 mL water instead of ethanol. The slurry was stirred until the NPs were completely deposited onto the support. Depending on the respective support, different time passed until the solution became clear, TiO_2 (1h) < Al_2O_3, hydrotalcite (20h) < KF/Al_2O_3, ZrO_2/La_2O_3 (48 h). The solid material was then separated from the solvent by centrifugation (3500 rpm, 20 min) and dried in an oven at 40 °C.

The same procedure was used to deposit bimetallic Pd-M NPs (M= Au, Ag or Cu) onto TiO_2. For preparation of catalysts with 0.5 wt % Pd loading, appropriate amounts of the Pd-M NPs solutions (2.6, 2.9 and 3.6 mL = 5.0 mg Pd) were applied which contained nominal molar ratios of Pd to M of 10:1, 4:1, and 2:1 respectively. The deposition time was the same to those using monometallic Pd NPs. Figure 9 illustrates the preparation of the supported nanoparticles.

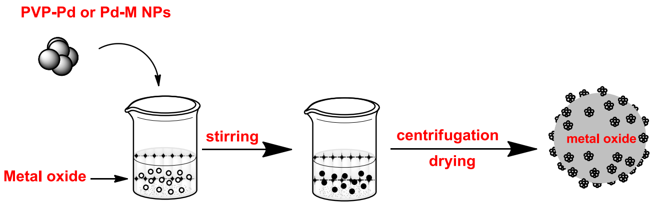

Figure 9. Preparation of supported pre-formed nanoparticles.

4.1.4 Thermal treatment of hydrotalcite support

The thermal treatment of hydrotalcite (HTs_30) support was carried out in a tube furnace at 300 °C for 5 hours, using a flow rate of 20 mL/min oxygen (>99.99 %) and 80 mL/min argon (>99.99 %).

4.2 Oxidation of 5-hydroxymethylfurfural

4.2.1 Materials

5-Hydroxymethylfurfural (HMF, >99 %) and 2,5-furandicarboxylic acid (FDCA, >97 %) were acquired from Sigma-Aldrich, 5-hydroxymethyl-furan-2-carboxylic acid (HMFCA) was obtained from Santa-Cruz Biotechnology. 5-Formyl-furan-2-carboxylic acid (FFCA) was purchased from Endothermic Life Science Molecules, and oxygen (>99.99 %) was obtained from Air-Liquide. All chemicals were used as received.

4.2.2 Reaction setup

5-Hydroxymethylfurfural (HMF) oxidation was carried out in a 25 mL three-necked round bottom flask equipped with a reflux condenser. The reactor was charged with 0.4 mmol of HMF solved in 20 mL of water. The molar ratio of HMF to Pd was 100:1. The reactor was placed in a pre-heated oil bath (100 °C). After few seconds of oxygen flow an aqueous NaOH (0.5 M) was introduced through a septum. The oxygen flow rate was controlled by a mass flow controller (Bronkhorst) and aqueous NaOH (0.5 M) was continuously added to the reaction mixture using a Hamilton syringe pump. The parameters were changed appropriately in order to investigate the effect of reaction conditions. Details of the reaction conditions are described in each result. Optimized reaction conditions were: 90 °C reaction temperature, 35 mL/min oxygen flow, and dosage of aqueous NaOH (0.5 M) with 1 mL/h. Figure 10 shows the experimental set up of the oxidation of HMF.

Figure 10. Experimental set up of the oxidation of HMF.

4.2.3 Analysis of the components in HMF oxidation

The reaction mixtures were analyzed by HPLC. Monitoring the reaction progress, samples of 50 µL were taken from the reaction mixture in regular time intervals using a 100 µl Hamilton syringe. The samples were diluted with a 0.2 % aqueous solution of H_3PO_4 and filled up to a volume of 10 mL. Then, the samples were centrifuged to remove the solid and subjected to HPLC analysis. Concentrations of products in the reaction solutions were calculated from calibration equations determined by HPLC measurements of reference substrates with known concentration. Table 10 summarizes the measurement conditions of HPLC analysis of the oxidation of HMF.

Table 10. Parameters of HPLC analysis for HMF oxidation.

Column	Rezex ROA-Organic acid H^+ (8%) (phenomenex)
Eluent	0.2 % aq. H_3PO_4
Temperature	25 °C
Flow rate	0.8 mL/min
Detectors	Merck-Hitachi L-4500 diode array detector
Auto sampler	Merck-Hitachi AS-2000A
Pump	Merck-Hitachi L-6200A intelligent pump
duration	40 min

Calibration curves of the components in HMF oxidation are shown in Figure 47, Appendix. Table 11 summarizes the calibration factor and the retention time of each component in the HMF oxidation.

Table 11. Retention times (RT) and calibration factors (f) of the components in HMF oxidation.

Component	f	RT
5-Hydroxymethylfurfural	1.35×10^{10}	30.91
5-Hydroxymethylfuran-2-carboxylic acid	0.90×10^{10}	20.48
5-Formylfuran-2-carboxylic acid	1.81×10^{10}	23.63
2,5-Furandicarboxylic acid	1.54×10^{10}	16.75

Evaluation criteria

The concentration of the components (C, mmol/ml) in the samples during the HMF oxidation could be calculated from the peak area obtained from the HPLC/UV chromatogram using the following equation:

$$\mathrm{C} = \frac{\mathrm{A_{HPLC,UV}\ x\ 200}}{\mathrm{f_{HPLC,UV}}} \tag{15}$$

Where $A_{HPLC,\ UV}$ = the peak area obtained from UV detector, f = the calibration factor, and 200 = the dilution value of the samples (50 µl in 10 mL).

The conversion of HMF, selectivity and yield of the products are calculated according to the following equations:

Conversion of HMF (X_i):

$$\mathrm{X_i(\%)} = \frac{\mathrm{C_{i0}} - C_\mathrm{i}}{C_\mathrm{i0}}\mathrm{x100} \tag{16}$$

Selectivity of product (S_j):

$$\mathrm{S_j(\%)} = \frac{\mathrm{C_j}}{\mathrm{C_{i0} - C_i}}\mathrm{x100} \tag{17}$$

Yield of products (Y_j):

$$\mathrm{Y_j(\%)} = \frac{\mathrm{C_j}}{C_\mathrm{i0}}\mathrm{x100} \tag{18}$$

Herein, C_{i0} = the concentration of HMF at t = 0, C_i = the concentration of HMF at time t and $C_{j=}$ the concentration of HMFCA, FFCA, or FDCA at time t in mmol/mL.

Carbon mass balance (M_c) is calculated by:

$$M_c = \frac{(c_{HMFCA,t} + c_{FFCA,t} + c_{FDCA,t})}{(c_{HMF,0} - c_{HMF,t})} \tag{19}$$

4.3 Oxidation of glycerol

4.3.1 Materials

Glycerol (GLY, >99 %) and Glycolic acid (GOA, >99 %) were purchased from Acros organics. Oxalic acid (OXA, >99 %) and DL-Glyceraldehyde (GLYHD, >90 %) were purchased from Sigma-Aldrich while DL-glyceric acid (GLYA, 20 % in water) and Dihydroxyacetone (DHA, >98 %) were obtained from TCI and VWR, respectively. Lactic acid (LA, >99 %) and tartonic acid (TA, >99 %) were purchased from Fluka. Oxygen (>99.9 %) was obtained from Air-Liquide. All chemicals and solvents were used as received.

4.3.2 Reaction setup

Glycerol oxidation was carried out in a small autoclave (25 mL, Parr). The reactor was charged with 9 mL aq. solution of GLY (5 mmol, 0.5 M), 21 mg of catalyst (molar ratio GLY:Pd = 5000:1) and aq. NaOH (10 M). After sealing, the reactor was pressurized with oxygen and then heated to the reaction temperature. During the experiment, the stirring rate was adjusted to 800 rpm (magnetic stirring). The parameters were changed appropriately in order to investigate the effect of reaction conditions. Details of the reaction conditions are described in each result. Figure 11 shows the experimental set up of glycerol oxidation. Optimized reaction conditions were: 100 °C reaction temperature, 5 bar of oxygen, and 1 mL aqueous solution of NaOH (10 M).

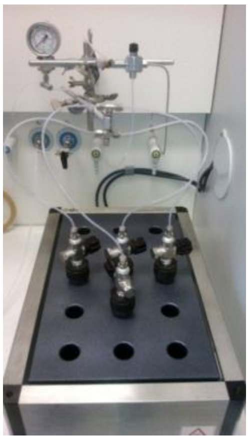

Figure 11. Experimental set up of the GLY oxidation.

4.3.3 Analysis of the component in glycerol oxidation

4.3.3.1 HPLC analysis

The reaction mixtures were analyzed by HPLC. After an appropriate reaction time, the reactor was cooled down, 250 µl of reaction mixture was taken out and diluted with 5 mM aqueous H_2SO_4 to 10 mL. Then, samples were centrifuged to remove the solid and subjected to HPLC analysis (Merck/Hitachi). Table 12 summarizes the parameters of HPLC analysis.

Table 12. Parameters of HPLC analysis for GLY oxidation.

Column	Rezex ROA-Organic acid H^+ (8%) (phenomenex)
Eluent	5 mM aq. H_2SO_4
Temperature	75 °C
Flow rate	0.5 mL/min
Detectors	UV-Vis and refractive index (RI)
Auto sampler	Merck-Hitachi AS-2000A
Pump	Merck-Hitachi L-6200A intelligent pump
Duration	30 min

Calibration curves of the components in GLY oxidation are shown in Figure 48, Appendix. The calibration factor and retention times of each component in the GLY oxidation are summarizes Table 13 .

Table 13. Retention times (RT) and calibration factors (f) of products in GLY oxidation.

Component	f/(UV)	RT(UV)
Glycerol	[1]64820	[1]17.07
Dihydroxyacetone	54747	16.43
	[1]51492	[1]16.69
Glyceric acid	265759	12.32
Glyceraldehyde	56535	14.61
Glycolic acid	88973	13.97
Tartonic acid	685736	8.03
Oxalic acid	2.07×10^6	7.76
Lactic acid	82999	14.43
Formic acid	7.66×10^4	15.20

[1]Obtained from refractive index detector.

Evaluation criteria

The quantification of glycerol (GLY) and dihydroxyacetone (DHA) in the reaction mixture is a challenge in the development of the analytical method because the products have nearly similar retention times. Therefore, a method was developed using simultaneously ultraviolet detector (UV) and refractive index detector (RID).

Due to the UV inactivity of glycerol, dihydroxyacetone (DHA) was quantified by evaluation of the recorded HPLC peaks in the UV range accurately (equation 20).

$$'c_{\mathrm{DHA}} = \frac{\mathrm{A}_{\mathrm{DHA,UV}} \text{ x } 40}{\mathrm{f}_{\mathrm{DHA,UV}}} \tag{20}$$

Where $A_{DHA,\,UV}$ = the peak area of DHA obtained from UV detector, f = the calibration factor of DHA obtained from UV detector, and 40 = value of the dilution (250 µl in 10 mL).

Next, the determined concentration of dihydroxacetone (DHA) in the sample could be used to calculate the peak area of DHA in the RID chromatogram by:

$$\mathrm{A}_{\mathrm{DHA,RID}} = \mathrm{f}_{\mathrm{RID}} \text{ x } 'c_{\mathrm{DHA}} \tag{21}$$

Where f = the calibration factor of DHA from RID.

The area of glycerol can be subtracted from the total area and the RID-HPLC area of dihydroxyacetone. Then, the glycerol concentration can be calculated by:

$$'c_{\mathrm{GLY}} = \frac{\left(\mathrm{A}_{\mathrm{DHA+GLY,RID}} - \mathrm{A}_{\mathrm{DHA,RID}}\right) \text{ x } 40}{\mathrm{f}_{\mathrm{GLY,RID}}} \tag{22}$$

Where $A_{DHA+GLY,\,RID}$ = the total peak area of GLY and DHA in the HPLC-RID chromatogram.

The conversion of glycerol, selectivity and yield of the products are calculated using the following equations:

Conversion of GLY (X_i):

$$X_i\,(\%) = \frac{C_{i0} - C_i}{C_{i0}}\ \text{x}\ 100 \tag{23}$$

Yield of products (Y_j):

$$Y_j(\%) = \frac{C_j}{C_{io}}\,\text{x}\ (\text{s.f.})\ \text{x}\ 100 \tag{24}$$

Selectivity of product (S_j):

$$S_j(\%) = \frac{C_j}{C_{i0} - C_i}\,\text{x}\ (\text{s.f.})\ \text{x}100 \tag{25}$$

Where C_{i0} = concentration of GLY at t = 0, C_i = concentration of GLY at time =t and $C_{j=}$ concentration of lactic acid, glyceric acid, tatronic acid, glycolic acid, oxalic acid, or acetic acid at time t in mmol/L and s.f. = the stoichiometric factor.

Turnover frequency (TOF) refers to the molar ratio of converted substrate to catalyst per hours. Thus, TOF is expressed by:

$$\text{TOF} = \frac{\text{mol of GLY converted}}{\text{t(h)x mol of total metal}} \tag{26}$$

Carbon mass balance (M_c) was calculated as:

$$M_c = \frac{(3C_{C-3,t} + 2C_{C-2,t} + C_{C-1,t})}{3(C_{GLY,0} - C_{GLY,t})} \tag{27}$$

Where C_{C-3} = the concentration of the C-3 products (lactic, glyceric and tatronic acid), C_{C-2} = the concentration of the C-2 products (glycolic and oxalic, and acetic acid), and C_{C-1} = the concentration of the C-1 product (formic acid).

4.3.3.2 NMR analysis

The quantification of lactic acid (LA), formic acid (FA) and glyceraldehyde (GYHD) in the reaction mixture is a challenge in the development of the analytical method by HPLC because the products have nearly similar retention times. Therefore, the NMR analysis was additionally used. However, selected reaction mixtures were quantified by ^{1}H NMR using a Bruker AV 400 spectrometer at 400.13 MHz and 25 °C. The aqueous reaction solutions (mixture of H_2O and D_2O) contained a known amount of maleic acid (0.25 M) which was used as reference for the concentration determination. The spectra were acquired with 30° pulses, at least 64 transients and a repetition time of 30 s, because maleic acid has a slow longitudinal relaxation behavior [176]. It proved to be essential to apply a thorough individual baseline correction to all resonance signals, this procedure provided better and more consistent results than solvent suppression by pre-saturation.

Chemical shifts (δ) are given in parts per million (ppm) and the coupling constants in Hz. Signal multiplicities were termed as follows: s (singlet), d (doublet), t (triplet), q (quartet), dd (double doublet), tt (triple triplet).

The following signals were assigned to the components (1H-NMR spectrum was shown in Figure 49, Appendix):

FA, $\delta = 8.45$ ppm (s, 1H); maleic acid, $\delta = 6.04$ ppm (s, 2H); TA, $\delta = 4.34$ ppm (s, 1H); LA, $\delta = 4.11$ ppm (q, $^3J = 6.9$ Hz, 1H), 1.32 ppm (d, $^3J = 6.9$ Hz, 3H); GLYA, $\delta = 4.08$ ppm (dd, $^3J = 5.9$ Hz, $^3J = 3.3$ Hz, 1H), 3.81 ppm (dd, $^3J = 3.3$ Hz, $^2J = 11.8$ Hz, 1H), 3.70 ppm (dd, $^3J = 5.9$ Hz, $^2J = 11.8$ Hz, 1H); GOA, $\delta = 3.94$ ppm (s, 2H); GLY, $\delta = 3.76$ ppm (tt, $^3J = 6.5$ Hz, $^3J = 4.3$ Hz, 1H), 3.64 ppm (dd, $^3J = 4.3$ Hz, $^2J = 11.7$ Hz, 2H), 3.55 ppm (dd, $^3J = 6.5$ Hz, $^2J = 11.7$ Hz, 2H); AA, $\delta = 1.89$ ppm (s, 3H).

5. Results and Discussion

5.1 Synthesis and characterization of catalysts

5.1.1 Synthesis and characterization of monometallic Pd NPs

The colloidal Pd NPs were synthesized by the reduction of the $PdCl_4^{2-}$ precursor in ethylene glycol using a small batch reactor at different molar ratios of NaOH to Pd (1:1, 2:1, and 4:1) in presence of polyvinylpyrrolidone (PVP) as a stabilizing agent of (Pd/PVP = 1/3 mol/mol) (Section 4.1.1). The presence of a low amount of (PVP) was necessary to protect the formed NPs from aggregation and it is independent on the used NaOH/Pd molar ratios.

Small angle X-ray scattering (SAXS) analysis was used to characterize the synthesized NPs. The SAXS measurements were done directly from the NPs synthesis solution without any pre-treatment. Figure 12a represents the scattering profile of the synthesized Pd NPs at different molar ratios of NaOH:Pd. The scattering profile of Pd_1 (NaOH:Pd = 1:1 mol/mol) is clearly different from Pd_2 or Pd_3 which were prepared at a higher molar ratio. The volume weighted particle radii distribution obtained by fitting of the scattering curve with the IFT method assuming spherical particle shape is shown in Figure 12b. The maximum of the volume weighted particle radii distributions (DvR) was 0.9 and 1 nm for NPs prepared at 4:1 and 2:1 molar ratios of NaOH to Pd respectively (Entries 2-3, Table 14). The maximum is shifted to 3.0 nm (Entry 1, Table 14) and the size distribution increased markedly with decreasing the molar ratio of NaOH:Pd up to (1:1).

It was reported that increasing the basicity of the NPs synthesis solution by increasing the molar ratio of NaOH:Pd led to a smaller particle size [177]. This was attributed to the high reduction rate of metal ions, since the concentration of the metal atoms in the solution is more and thus reaching the critical concentration quickly. This results in a fast nucleation of the metal atoms.

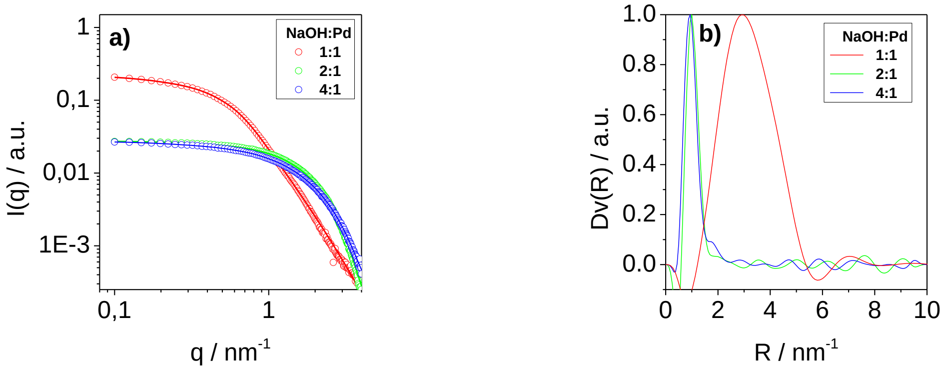

Figure 12. Smeared scattering profiles of Pd NPs prepared at different NaOH:Pd ratios (symbols) and results of curve fitting using the IFT method (solid line) – (a) and the corresponding volume weighted particle radii distributions - (b).

Other techniques which could be used to characterize the synthesized Pd NPs are the powder X-ray diffraction (XRD) and transmission electron microscopy (TEM). In both techniques, the NPs cannot be measured directly from the synthesis solution; pre-treatments were required (in contrast to SAXS).

The XRD pattern of the prepared Pd NPs is shown in Figure 13. All the three prepared NPs showed a diffraction peak at about 40° corresponding to the (111) lattice plane of metallic Pd. An indication of the formation of a larger crystallite size with fcc structure (PDF [00-087-0637]) for Pd_1 (synthesized at a molar NaOH:Pd ratio of 1:1) is the presence of additional diffraction peaks of (200) and (220) lattice planes at ca. 47.5° and 67° respectively. The mean crystallite size of the NPs was calculated according to the Scherer equation (Entries 1, Table 14). In contrast, if the molar ratio of NaOH to Pd increased, a smaller crystallite size with a mean diameter of 2.0 nm for Pd_2 (prepared at 2:1 molar ratio of NaOH to Pd) and 1.8 nm for Pd_3 (prepared at 4:1 molar ratio of NaOH to Pd) were formed (Entries 2-3). These results confirmed the obtained results from SAXS concerning the influence of the NaOH:Pd molar ratio on the particle size.

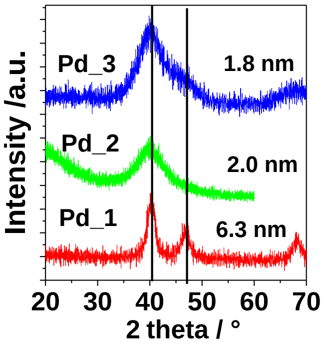

Figure 13. XRD pattern of Pd NPs prepared at different molar ratios of NaOH:Pd of 4:1, 2:1, and 1:1 for Pd_3, Pd_2, and Pd_1 respectively.

The TEM images of the Pd NPs are shown in Figure 14. All the three synthesized Pd NPs possess approximately a spherical shape. The histogram of the particle size distribution derived from TEM images (as inserted in Figure 14) showed that the mean diameter increased as the molar ratio of NaOH:Pd decreased. These findings are comparable with the results obtained from XRD and SAXS. In addition, the histogram of particle size distribution of the synthesized NPs also showed that the width of the particle size distribution increased markedly for Pd_1 (synthesized at the lowest molar ratios of NaOH:Pd = 1:1).

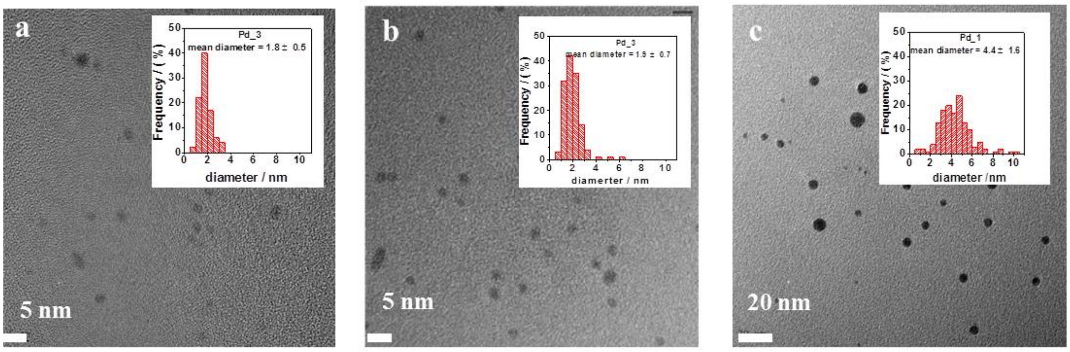

Figure 14. TEM images and the corresponding histograms of the particle size distributions of Pd NPs prepared at different molar ratio of NaOH:Pd of 4:1, 2:1, and 1:1 for a) Pd_3– 4:1 (98 particles), b) Pd_2–2:1(133 particles), and c) Pd_1 – 1:1(144 particles).

The particles size of (Pd_2 or Pd_3) obtained from TEM is in agreement with that obtained using other techniques (XRD and SAXS). In contrast, the particles size for the Pd_1 obtained from TEM is clearly smaller (Entry1, Table 14). This could be attributed to the fact that a volume weighted size distribution was derived from SAXS and XRD while a number weighted particle size distribution was obtained from TEM [178]. However, no significant effects were observed on the size distribution of the synthesized NPs during the sample preparation for XRD and TEM measurements. Thus, all these methods could be used to obtain information about the size of the synthesized NPs in the solution.

Table 14. Characteristics of the prepared nanoparticles.

Entry	NPs	NaOH/Pd [mol/mol]	Rmax(SAXS) [nm]	Dmean(XRD) [nm]	Dmean(TEM) [nm]
1	Pd_1	1:1	3.0	6.3	4.4±1.6
2	Pd_2	2:1	1.0	2.0	1.9±0.7
3	Pd_3	4:1	0.9	1.8	1.8±0.5

5.1.2 Synthesis and characterization of supported monometallic Pd NPs

The heterogeneous catalysts were prepared by the direct colloidal deposition method [96]. In the presented work, the Pd NPs were added slowly using syringe pump at constants flow rate

(10 mL/h) under stirring at atmospheric conditions. The slow addition could provide a better dispersion of the nanoparticles on the surface of the support.

The Pd NPs used in the preparation of heterogeneous catalysts are those named Pd_3 (prepared at a 4:1 molar ratio of NaOH:Pd). The Pd_3 NPs were chosen depending on their catalytic performance in the selective oxidation of HMF which will be discussed later in detail (Section 5.2.1.2).An indication that most of the Pd NPs were deposited onto the support is the change in the color of the solution containing PVP protected Pd NPs (with support in solvent) from dark brown to almost colorless. Depending on the support used, different times were passed till the solution became approximately colorless (Table 15). The deposition of NPs onto titanium oxide (TiO_2) was successfully accomplished using water or ethanol as a solvent in a short time of 1 h. In contrast, a longer time of 24 h was needed for [HT (MG =30, 61, and 70) and (γ-Al_2O_3)] and about 48 h for [KF/Al_2O_3 and ZrO_2/La_2O_3]. Since the deposition of NPs on a KF/Al_2O_3 and a ZrO_2/La_2O_3 in ethanol was unsuccessful, water was used as a solvent. However, the comparison of the deposition times of NPs and the point of zero charge (p.z.c.) of the used support (p.z.c: TiO_2 = 6-7 [179]; ZrO_2/La_2O_3~7 (determined from measurement of the zeta potential, Section 7.1.8, Appendix); γ-Al_2O_3 = 8-9 [179]) showed that no correlation between the deposition time and p.z.c. Similarly, it was previously reported that the Au NPs deposition time did not depend on the p.z.c. of the specific support. Fast Au NPs deposition was observed on TiO_2, while other supports (e.g. γ-Al_2O_3 and ZrO_2) showed longer deposition times [180]. The negative charge of the protecting agent (polyvinylalcohol) was suggested to be a reason for the independence of the Au NPs adsorption time from the p.z.c [180]. Additionally, it was reported that the adsorption of the Au NPs on TiO_2 was better than on ZrO_2 for 2 nm negatively polarized Au NPs at pH < IEP (IEP - isoelectronic point) due to a higher number of positively charged hydroxyl surface groups on TiO_2. It was assumed that the adsorbed layer of ligands, necessary for stabilization of the Au NPs in solution, was destroyed during the adsorption process. Furthermore, various factors could affect the adsorption process of the NPs beside electrostatic interactions e.g. van der Waals interactions [8].

Characteristics of the freshly Pd NPs based materials are summarized in Table 15. BET surface of the Pd catalysts after NPs deposition was slightly lower than the corresponding unloaded support due to a low nominal Pd loading (0.5 w %). These findings are in accordance with the reported literature [126]. The BET surface of a $Pd/KF/Al_2O_3$ catalyst was obviously higher than the unloaded support counterparts. This observation might be ascribed to the loss of KF from the alumina surface which increases the accessibility of the pores for nitrogen (the loss of KF from the alumina surface will be discussed later in details, Section 5.2.2.1). The mean pore size of TiO_2, ZrO_2/La_2O_3, and γ-Al_2O_3 was 17.5, 18, and 7 nm, respectively (see Table 15). Depending on the results, there is no correlation between the BET surfaces, pore volume, or pore diameter and the deposition time. The deposited Pd NPs onto supports are believed to be mainly located on the external surface of the support because of the small pore volume of (ZrO_2/La_2O_3, TiO_2) and the low pore diameter of (γ-Al_2O_3).

Table 15. Characteristics of the freshly prepared Pd NPs based materials.

Entry	Catalyst	Solvent	Time [h]	Pd [wt%]	BET [m^2/g]	Pore volume [mL/g]	Pore size [nm]	d(NPs) [nm]
1	Pd_3 NPs			-	-			1.8 ± 0.5
2	Al_2O_3				220	0.62	7	
3	Pd/Al_2O_3	EtOH	24	0.45	176			2.7 ± 0.6
4	KF/ Al_2O_3				25	0.06 [181]		
5	Pd/KF/ Al_2O_3	EtOH	-					
		H_2O	48	0.6	101			n.d.*
6	TiO_2				50	0.25 [182]	17.5	
7	Pd/TiO_2	EtOH	1	0.53	35			2.1 ± 0.7
		H_2O	1	0.5	35			
8	ZrO_2/La_2O_3				279	0.08	18	
9	$Pd/ZrO_2/La_2O_3$	EtOH	-		252			
		H_2O	48	0.39				2.6 ± 0.5
10	HT_30				147			
11	Pd/HT_30	EtOH	24	0.5	-	n.d.*		2.2 ± 0.4
12	HT_61				25			
13	Pd/HT_61	EtOH	24	0.28	-	n.d.*		2.3 ± 0.7
14	HT_70				14			
15	Pd/HT_70	EtOH	24	0.38	-	n.d.*		2.0 ± 0.6
16	Cal.HT_30				98			
17	Pd/Cal.HT_30	EtOH	24	0.45	-	n.d.*		n.d.*

*** not determined.**

STEM-HAADF images of the supported pre-formed Pd NPs are presented in Figure 15. A reliable finding of Pd on ZrO_2/La_2O_3 could be obtained by element mapping with EDX due to the electron density of the ZrO_2/La_2O_3 support (La: atomic number 57, Zr: atomic number 40) is higher and similar, respectively to the Pd (atomic number 46). A slight increase in the mean diameter of Pd NPs was observed during the deposition of NPs onto different supports by making a comparison between the histogram of the particle size distribution derived from STEM images (inserted in Figure 15) and that for the unsupported Pd NPs (inserted in Figure 15a). The largest increase of Pd NPs was observed on the catalyst containing Al_2O_3 and ZrO_2/La_2O_3 as supports where the mean diameter of Pd NPs was 2.7 and 2.6 nm, respectively (Entries 3 and 9, Table 15).

A slight increase in the particle size after deposition was previously reported [183]. The distributions of Pd NPs were not always homogenous on the used support (STEM images, Figure 15). This might be attributed partly to the presence of the polymeric stabilizing agent PVP. In solution, PVP is able to form larger structures consisting of a great number of entangled PVP chains where the NPs are dispersed [184].

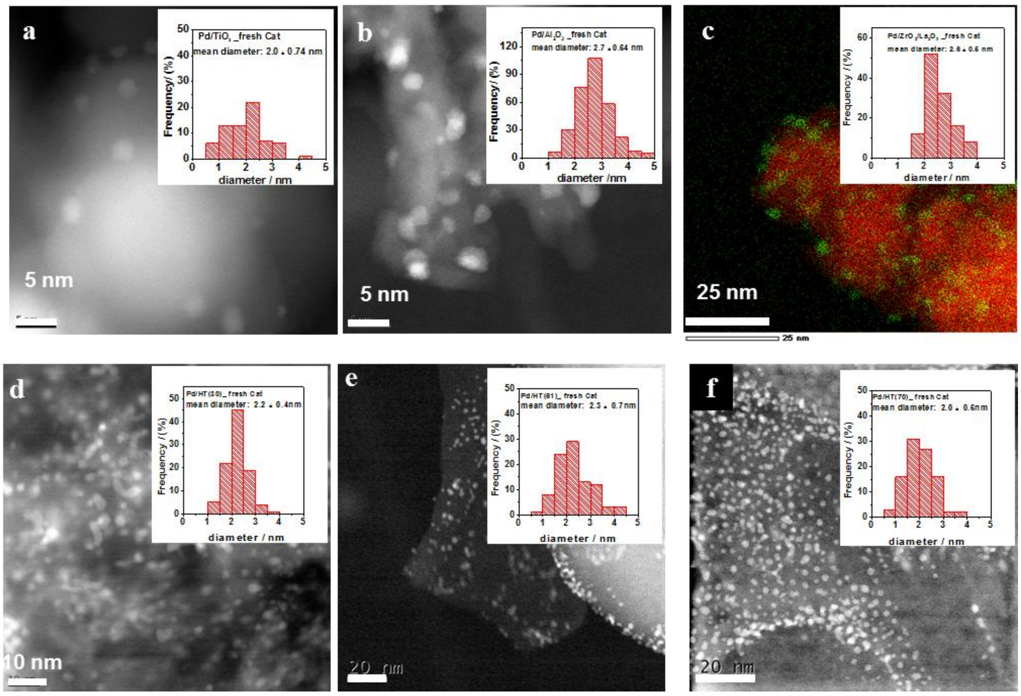

Figure 15. STEM-HAADF images and histogram of the particle size distribution of a)- Pd/TiO_2 (99 particles), b)-Pd/Al_2O_3 (80 particles), c)-Pd/ZrO_2/La_2O_3 (53 particles), d)-Pd/HT_30 (97 particles), e)-Pd/HT_61 (93 particles), f)- Pd/HT_70 (97 particles).

As mentioned before, the heterogeneous catalysts were prepared using PVP stabilized Pd NPs and the Pd NPs might be adsorbed on the support with and without direct metal-support interaction (see Figure 16). To gain information about how the Pd species would dominate on the support, additional experiments were conducted similar to the deposition of Pd NPs onto supports but in the absence of a metal. However, the supports e.g. TiO_2, ZrO_2/La_2O_3 or Al_2O_3 were treated with pure PVP in water for 1 h (15.33 mg PVP in 10 mL water corresponding to 2.3 mL PVP in NPs synthesis solution). The amount of PVP adsorbed on catalyst surface was estimated from the difference of carbon content in the aqueous solution before and after treatment of the support with PVP within 1 h. The results showed that on Al_2O_3, about 50 % of the available PVP amount was adsorbed after 1 h while on titania was only 7 %. No PVP adsorption was detected after 1 h on ZrO_2/La_2O_3. Depending on these results, most of the deposited Pd NPs should be in direct interaction with the TiO_2 (species ii) because the Pd NPs were completely adsorbed on the support after 1 h. On contrary, most of Pd NPs should be embedded in adsorbed PVP (species i) on Al_2O_3 compared to TiO_2 because of the better adsorption of PVP on the Al_2O_3 surface.

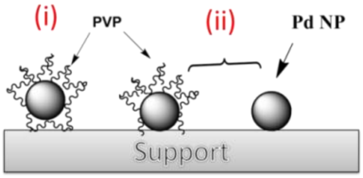

Figure 16. Formal scheme of Pd NPs species on the support surface.

5.1.3 Synthesis and characterization of bimetallic nanoparticles

The bimetallic nanoparticles (Pd-M NPs; M= Ag, Au, or Cu) were synthesized by a successive reduction method [43]. However, a second metal was added slowly by a syringe pump at a constant flow rate (1 mL/h) to the pre-formed PVP stabilized Pd NPs with a nominal molar ratios of Pd:M of 10:1, 4:1 and 2:1. Because of the slow addition of the solution of metal salt, the concentration of metal atom in the synthesis solution will be always low and, therefore, super-saturation of ethylene glycol solution with the metal atoms which leads to the formation of pure metallic NPs by homogeneous nucleation could be avoided. According to the approximate calculations [185, 186] (Section 7.2, Appendix), low amounts of second metal were used to modify the surface of the Pd NPs. Rough calculations showed that the ratio of the added metal atoms (M= Ag, Au, or Cu) to the Pd surface atoms of 16 %, 40 % and 80 % could be obtained by using a 10:1, 4:1, and 2:1 molar ratio of Pd to M, respectively.

If the redox potential of the reducing agent is more negative than the oxidizer, then the reduction will be possible thermodynamically. The difference between the redox potential of the reducer and oxidizer should be higher than 0.3-0.4 eV, otherwise, the reduction will be slow and formation of NPs might not be possible [187]. It was reported that the reduction potential of the metals is not affected by the temperature, in contrast to the oxidation potential of ethylene glycol. However, an increase in the temperature leads to oxidation of the ethylene glycol at a lower potential [188]. In this respect, Pd-Cu nanoparticles were synthesized starting from the pre-formed Pd NPs at 90 °C because the reduction potential of copper (Cu^0/Cu^{2+}= 0.34 eV) is relatively low. Therefore, a high temperature is required to decrease the oxidation potential of ethylene glycol and hence make the difference between the reduction potential of the Cu precursor and the oxidation potential of ethylene glycol big enough to form the NPs [189]. The reduction potential of silver (Ag^{1+}/Au^0 = 0.80 eV) is higher than that for copper but in order to provide a fast reduction of silver, the synthesis of Pd-Ag was carried out at 90 °C [189]. In contrast, the reduction potential of Au (Au^{3+}/Au^0 = 1.52 eV) is clearly higher than those for copper and silver. Thus, room temperature was enough to reduce the gold in ethylene glycol [22].

UV-Vis analysis was used to characterize the prepared bimetallic Pd nanoparticles in solution. An increase in the intensity at nearly identical signal shape was detected when silver or gold content increased in the catalysts. Furthermore, surface plasmon band of Ag or Au NPs were not detected even when high amounts of silver or gold are present (Figure 17 a-b). Based on the literature, the surface plasmon bands of Ag NPs in the bimetallic Pd(core)-Ag(shell) NPs were observed close to 360 nm when more than 10 monolayers of Ag were deposited on the Pd. The band was then shifted to a shorter wavelength when the shell thickness was less than 10 monolayers and disappeared if the thickness of the shell was below three-atomic Ag layers [93]. Previously, the surface plasmon band of Au NPs was detected at 250 nm when the Au ratio was higher than 20 % mol [91]. The UV-Vis spectrum of the Pd-Cu NPs is similar to the Pd NPs. However, the surface plasmon band of Cu NPs were not detected as well which usually appears at 560 nm [175] (Figure 17c). Hence, the results indicate that particles contains only Au, Cu, or Ag NPs are not present in solution, they are always in combination with Pd NPs.

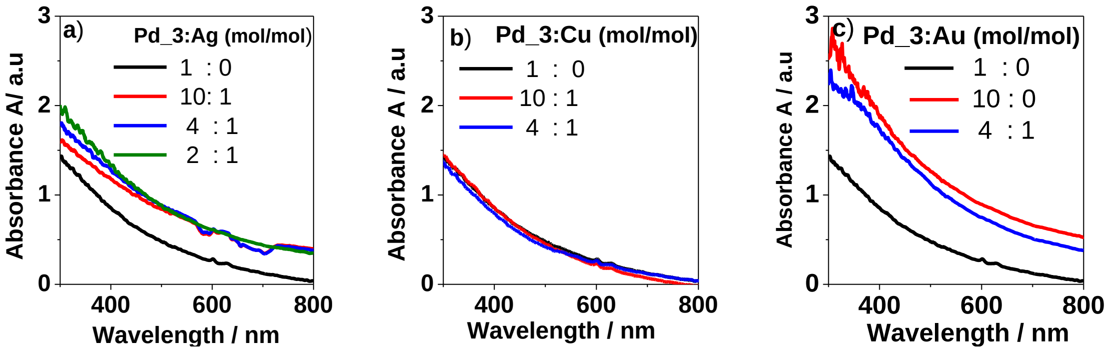

Figure 17. UV-Vis spectra of a) – Pd_3-Ag NPs, b)- Pd_3-Cu NPs, and c)- Pd_3-Au NPs.

The prepared bimetallic nanoparticles were characterized by XRD as well. Figure 18b shows the comparison between the XRD pattern of Pd-Ag NPs and the monometallic Pd_3 NPs counterparts. The prepared bimetallic NPs showed a diffraction peak at about 40° which is attributed to (111) lattice plane of the metallic Pd. No shift of the diffraction peak of the Pd was observed after addition of Ag even when high amounts are used (Pd: Ag = 2:1 mol/mol). Characteristic peaks of neither metallic Ag nor AgO phase were detected.

Based on the reported literature, the position of the diffraction peak of the Pd-Ag NPs with an alloyed structures were found between the Bragg lines of the pure Pd and Ag [80]. Similar observations were observed for those bimetallic Pd-Au or Pd-Cu NPs (Figure 18 b and c).

It is worth to mention that small additional peaks at ca. 47.5° and 67° appeared for the Pd-Ag NPs (Pd:Ag = 4:1 or 2:1 mol/mol) and the Pd-Au NPs (4:1 mol/mol). Since the crystallite sizes of the Pd-Cu NPs (Pd:Cu =4:1 mol/mol) and Pd-Au NPs (Pd:Au =4:1 mol/mol) are similar, these observations might be attributed to a different arrangement of the second metal (Au, Ag or Cu) on the Pd NPs catalysts and not to the formation of larger crystallite sizes as already observed for Pd_1 (Figure 13).

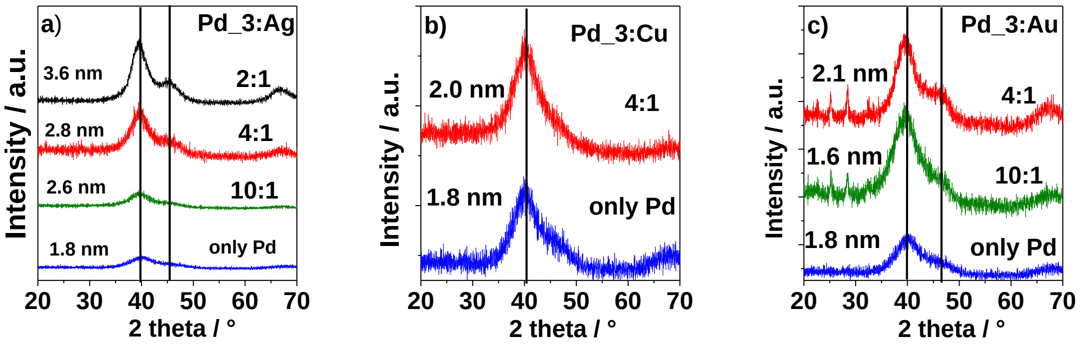

Figure 18. XRD pattern of bimetallic nanoparticles a) Pd_3-Ag NPs, b)- Pd_3-Cu NPs, c)- Pd_3-Au NPs .

The prepared bimetallic nanoparticles which possess 4:1 molar ratio of the Pd to M (M = Ag, Au, or Cu) were additionally characterized by TEM (see Figure 19). Approximately spherical shape of NPs was observed for the bimetallic Pd nanoparticles with Ag or Cu. In contrast, the TEM image of Pd-Au NPs showed aggregated NPs beside the presence of a spherical shape (Figure 19c). The histogram of the particle size derived from TEM images showed that the mean diameter of the particles was bigger for the Pd-Au NPs (2.7 nm) than for the Pd-Ag NPs (2.5 nm) and the Pd-Cu NPs (2.1 nm) (Entries 5 and 10, Table 16). In addition, the width of the particles size distribution increased markedly in all of the prepared bimetallic nanoparticles compared to the Pd_3 monometallic counterparts (inserted in Figure 19).

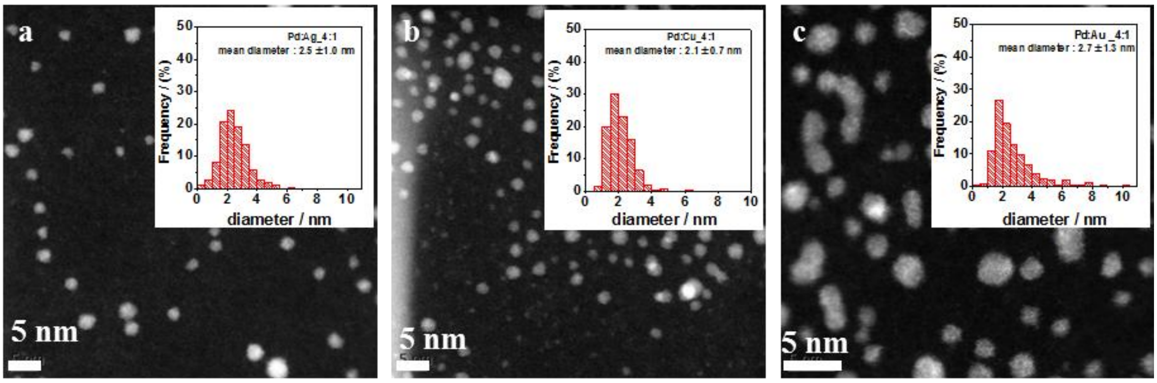

Figure 19. TEM images and the corresponding histograms of the particle size distributions of a) - Pd_3-Ag (4:1), b)- Pd_3-Cu (4:1), and Pd_3-Au (4:1).

Table 16. Characteristics of unsupported mono- and bimetallic nanoparticles.

Entry	NPs	NaOH:Pd [mol/mol]	[1]Pd:M [mol/mol]	Rmax(SAXS) [nm]	Dmean(XRD) [nm]	Dmean(TEM) [nm]
1	Pd_3	4:1	-	0.9	1.8	1.8±0.5
2	Pd-Ag	-	10:1	n.d.*	2.6	n.d.*
3	Pd-Ag	-	4:1	n.d.*	2.8	2.5 ± 1.0
4	Pd-Ag	-	2:1	n.d.*	3.6	n.d.*
5	Pd-Au	-	10:1	n.d.*	1.6	n.d.*
6	Pd-Au	-	4:1	n.d.*	2.1	2.7 ± 1.3
7	Pd-Cu	-	10:1	n.d.*	n.d.*	n.d.*
8	Pd-Cu	-	4:1	n.d.*	2.0	2.1 ± 0.7

[1] nominal molar ratios,* not determined.

5.1.4 Synthesis and characterization of supported bimetallic nanoparticles

The supported bimetallic nanoparticles were prepared using the same procedure for the deposition of the monometallic Pd nanoparticles onto supports. The TiO_2 was chosen as support because of the shortest deposition time compared to the other supports. The deposition of bimetallic NPs onto the titanium oxide (TiO_2) was successfully performed using ethanol as a solvent within 1h which is comparable with those using the monometallic Pd NPs. This means that the addition of a second metal to the Pd NPs didn't affect the deposition behavior. Characteristics of the freshly supported bimetallic NPs are summarized in Table 17. The amount of Pd loading in all prepared catalysts was not so far from a nominal value (0.5 wt %). As observed before, the BET surface of Pd/TiO_2 was slightly decreased compared to the unloaded respective support (Entries 6-7, Table 15). The same is assumed when the bimetallic nanoparticles were deposited. The molar ratio of Pd to M (M = Ag, Au, or Cu) obtained from ICP was not so far from the nominal value. Thus, different molar ratios of Pd to M could be synthesized with the applied method for preparation of the bimetallic NPs.

Table 17. Characteristics of the freshly bimetallic nanoparticles based materials.

Entry	Catalyst	Pd [wt %]	[1]Pd:M [mol/mol]	[2]Pd:M [mol/mol]	d [nm]
1	Pd-Ag/TiO_2	0.45	10:1	8:1	n.d.*
2	Pd-Ag/TiO_2	0.45	4:1	3:1	2.8 ± 1.1
3	Pd-Ag/TiO_2	0.55	2:1	1.4:1	n.d.*
4	Pd-Au/TiO_2	0.47	10:1	9.8:1	n.d.*
5	Pd-Au/TiO_2	0.44	4:1	4.3:1	n.d.*
6	Pd-Cu/TiO_2	0.42	10.1	11.6	n.d.*
7	Pd-Cu/TiO_2	0.40	4:1	3.4:1	n.d.*

[1]nominal molar ratios, [2] experimental determined molar ratios,* not determined.

STEM-HAADF image of titania supported Pd-Ag NPs (Pd:Ag = 4:1 mol/mol) is shown in Figure 20. The histogram of the particle size distributions derived from the image (as inserted in Figure 20) showed that the mean diameter of particles size was 2.8 nm (Entry 2, Table 17), which is slightly bigger than on the unsupported Pd-Ag NPs (Table 16). The small increase in the particle size after the deposition is in comparable with the reported results [183]. The shape of the NPs is approximately spherical as well. In addition, the histogram of the particle size distribution also showed that the width of the particle size distribution increased only slightly in the case of supported Pd-Ag NPs compared to the unsupported NPs counterparts

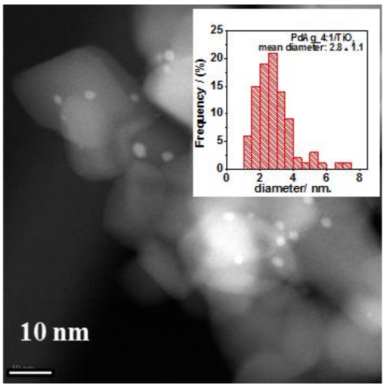

Figure 20. STEM-HAADF images and particle size distributions of Pd-Ag (4:1)/TiO_2 (93 particles).

Beside the morphology and particle size distribution of Pd-Ag NPs (Pd:Ag = 4:1 mol/mol) which were obtained by STEM using a high angle annular dark field (HAADF), EDX analyses of individual particles were recorded. The Pd (La) is overlapped with Ag (Lb), therefore, it is difficult to distinguish between them (Figure 21c). The EDX spectrum of individual particle is presented in Figure 21b. The EDS indicates that the composition of particles seems to be not always homogeneous e.g. the particle 003 shows that the intensity of the peak which is attributed to the Ag is clearly higher than on the particles 002 or 001. This could be used as indication that the ratio of Ag to Pd in the particle 003 is higher than in the other particles. Particles which contain Ag NPs only were not detected.

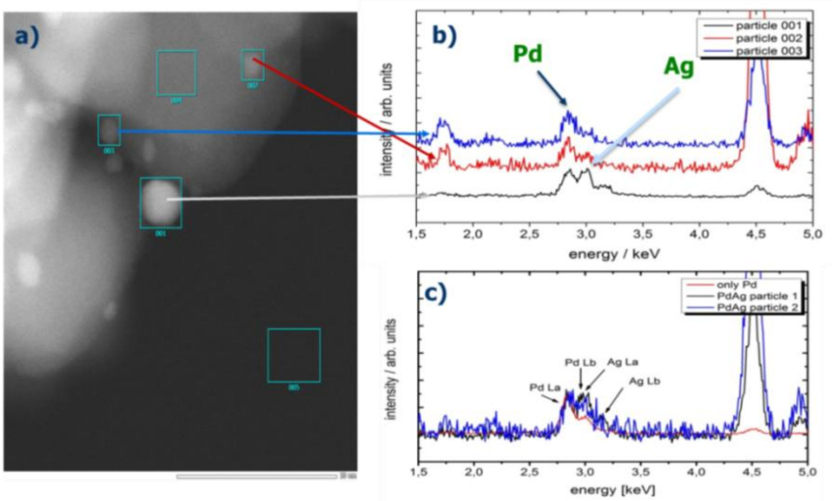

Figure 21. EDX spectra of individual particles of Pd-Ag(4:1)NPs/TiO_2.

XPS analysis was used to obtain information about the electronic structure of the metals on the support before the oxidation reaction (Figure 22). Generally, there are many factors that could affect the position of Pd in XPS spectra such as the electronic interaction of Pd with the support, the size of Pd species and the valence state of Pd where the binding energy of Pd^{2+} (bivalent) is usually higher than that of the metallic Pd [190-192].

In the fresh Pd/TiO_2 catalyst both metallic and bivalent Pd were detected (Figure 22a). The gray area represents the metallic Pd ($3d_{5/2}$ = 335.4 eV, $5d_{3/2}$ = 340.6 eV) while the dark gray area represents the bivalent Pd ($3d_{5/2}$ = 337.0 eV, $3d_{3/2}$ = 342.4 eV).

The addition of the second metal has an influence on the electronic structure of the Pd in the bimetallic catalysts. However, the Pd bivalent was only present in the Pd-Cu NPs catalyst. In contrast, the Pd bivalent was slightly reduced after (Au) addition. The lowest amounts of the Pd bivalent was detected in the Pd-Ag catalysts, (Figure 22a).

The XPS spectrum of Ag 3d electrons is shown in Figure 22b. The binding energy of metallic Ag is very close to that of oxidic Ag. Therefore, it is difficult to distinguish between them [193]. Similarly, the binding energy of metallic Cu is very close to that of Cu $^{+1}$ [194]. Thus, it is difficult to interpret Figure 22c which represents Cu 2p electrons. The XPS spectrum was recorded for Au 4f electrons and showed that gold is present in a metallic form (see Figure 22d).

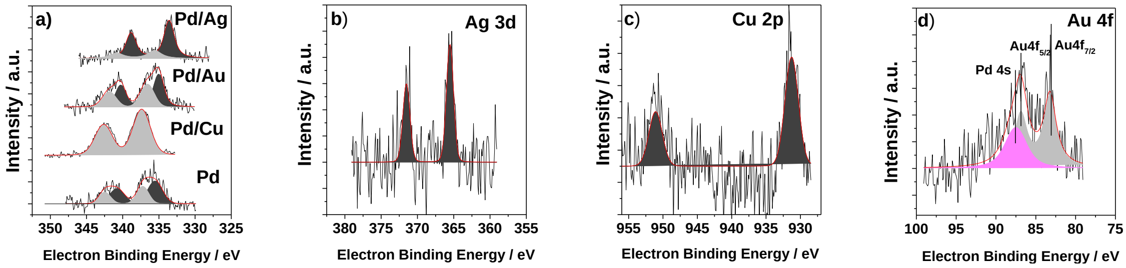

Figure 22. XPS spectra of bimetallic catalyst a)-the Pd3d electrons b)- Ag 3d electrons, c)- Cu 2p electrons, d)- Au 4f electrons from the fresh supported catalyst.

The influence of the amount of the second metal on the electronic structure of the Pd was studied for silver. The XPS spectra for a nominal molar ratio of Pd to Ag (10:1, 4:1, or 2:1 mol/mol) are shown in Figure 23. In all of these catalysts, the amount of bivalent Pd^{2+} is partially reduced, even if low amounts of silver are present in the catalyst (Pd:Ag =10:1 mol/mol). The interpretation of the XPS spectrum of Ag 3d electrons are complicated as mentioned before [193]. Furthermore, the comparison of the Ag 3d electrons for these catalysts showed a small shift of XPS signals. The observed small shift is not clearly understood as well (Figure 23b).

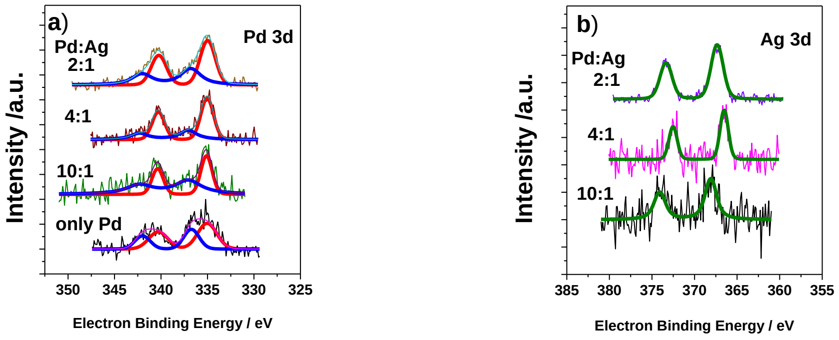

Figure 23. XPS spectra of a)- the Pd3d electrons b)- Ag 3d electrons from the fresh supported catalyst.

5.2 Catalytic oxidation of 5-hydroxymethylfurfural to 2,5-furandicarboxylic acid

5.2.1 5-Hydroxymethylfurfural oxidation on unsupported monometallic Pd NPs

5.2.1.1 Influence of the reaction parameters

The effect of selected reaction parameters such as oxygen flow rate and reaction temperature on the HMF oxidation were studied on unsupported Pd nanoparticles. The experiments were performed by adding 0.5 M NaOH at 1 mL/h. This concentration was chosen, because previous experiments had shown that a higher concentration of NaOH (2 M) at the same addition rate leads to formation of a high amount of side products, while using a lower concentration of NaOH (0.25 M), clearly slows the reaction rate.

- **Effect of the oxygen flow rate on the selective 5-hydroxymethylfurfural oxidation**

Initial experiments showed that the HMF oxidation could be performed under the atmospheric pressure. Therefore, the influence of oxygen flow rate on HMF conversion and products yield was studied (Figure 24).in alkaline aqueous solution using Pd_4 NPs as catalysts (Pd_4 NPs were prepared at 2:1 molar ratio of NaOH to Pd at room temperature for 24 h, Section 4.1.1). The oxygen flow varied between 10 and 115 mL/min. Additionally, the use of compressed air (20 mL/min, corresponding to 4 mL/min oxygen) was also studied

HMF was fully converted after about 2h under oxygen flow rates between 4 and 58 mL/min. After this time, the molar ratio of NaOH:HMF was achieved a 2.5:1 mol/mol. The desired products of HMFCA, FFCA, and FDCA were formed only in minor amounts (4-9 %) at the lowest oxygen flow of 4 mL/min. Products of Cannizzaro reaction (2.5-dihydroxymethylfuran (DHMF) and 5-hydroxymethyl-furan-2-carboxylic acid) and HMF degradation (formic acid and levulinic acid) were previously reported in alkaline solution and in the absence of oxygen [116]. The yield of desired products was improved by increasing the rate of oxygen flow up to 10, 35, or 58 mL/min. At the same tendency, the HMFCA yield increased to 25, 37 and 47 % after 1.5 h. After that, it remained constant independent on the used oxygen flow.

The formation of FFCA with time was approximately independent on oxygen flow rates used (10-58 mL/min) and the maximum yield was 40 % after 2 h. Here, before the FFCA reached its maximum, FDCA started to form. Using the higher oxygen flow of 115 mL/min, the HMF was clearly converted at longer time compared to the others oxygen flow used. The yield of HMFCA was almost constant after 2 h and the formation of FFCA was in minor amounts, therefore, a low yield of FDCA was detected at 115 mL/min O_2 flow. Noteworthy, the carbon mass balance was strongly decreased up to 0.57 after 4 h which was relatively higher in short reaction time (< 1 h, approximately =1) at the highest oxygen flow of 115 mL/min. This might be ascribed to the formation of unwanted side products.

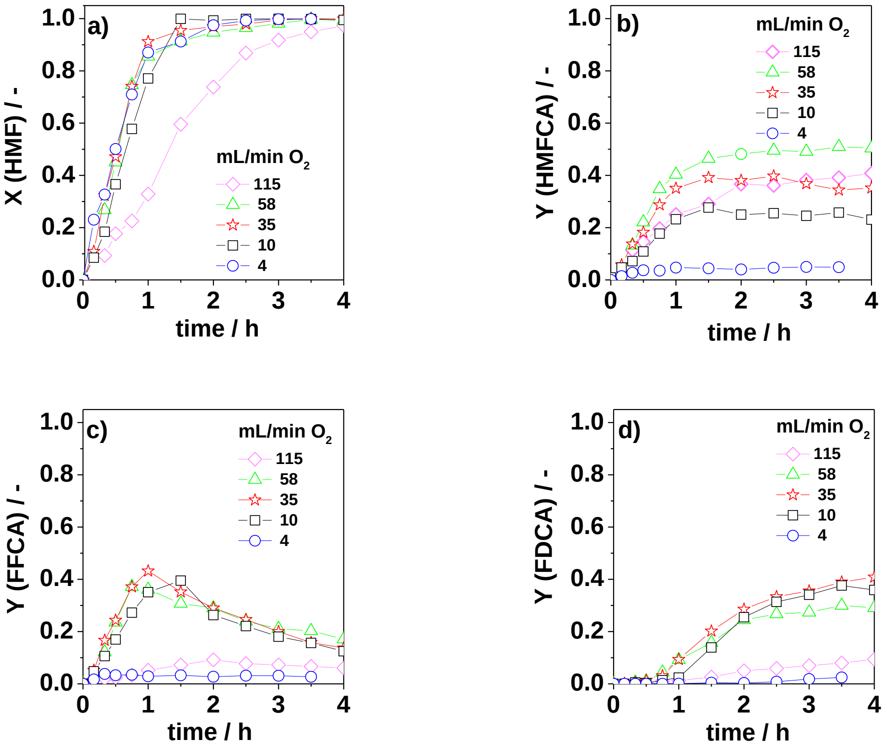

Figure 24. Influence of the O_2 flow rate on HMF oxidation using Pd NPs (Pd_4) as catalyst. Reaction conditions: HMF (0.4 mmol), H_2O (20 mL), HMF:Pd=80 (mol/mol) , 90 °C, (1 mL/h) of aq. NaOH (0.5 M), 4 h as the reaction time.

The presented results show that the catalytic performance of the Pd NPs in HMF oxidations depends on oxygen flow rate (oxygen content in the water phase). A fast deactivation of the Pd NPs was detected at the highest oxygen flow of 115 mL/min. This could be ascribed to a reversible Pd_O_2 adsorption rather than formation of a metal oxide surfaces as previously reported for oxidation of benzyl alcohols [22].

Based on the reported literature, Pd catalysts seem to be more sensitive to high oxygen content than Au based materials. No deactivation of the Au catalyst under high oxygen pressure in strong basic solution was observed [116, 119, 123]. The deactivation of the Pd NPs catalyst was also observed when the oxygen flow was decreased from 58 to 4 mL/min. This might be attributed to blocking of active surface sites by strong adsorption of unwanted byproducts formed mainly from adsorbed substrate (HMF) and intermediate (HMFCA) species. The HMF conversion rate was nearly identical under different oxygen flow rates but the yield of HMFCA was different. This could indicate that byproducts formation and the oxidation of HMF to HMFCA and HMFCA to FFCA might proceed with similar rate. In this case the formation of adsorbed HMF or HMFCA species should be included in the rate determining step. At a certain point of time, the oxidation of FFCA to FDCA proceeds while the yield of HMFCA remained constant. This could be used as an indication that oxidation of the alcohol and the aldehyde moieties might occur on different Pd surface sites. In order to investigate whether the oxidation of FFCA to FDCA occurs without participation of Pd NPs, an additional experiment was performed using FFCA (0.15 mmol) as substrate in the absence of Pd NPs catalyst under identical reaction conditions (35 mL/min O_2, 1 mL/h NaOH (0.5 M) and 90 °C). The results showed that only a minor amount of FFCA was transformed (12 % conversion of FFCA in 6 h) and no FDCA was detected. This result strongly indicates that the Pd NPs catalyze the transformation of FFCA to FDCA even if oxidation of HMFCA was stopped. Therefore, it is believed that oxidation of HMFCA to FFCA and that of FFCA to FDCA happen on different Pd NPs surface sites.

- **Effect of the temperature on the selective HMF oxidation**

Recently, the oxidation of HMF was performed in the presence of carbon supported Pd at 25 °C at oxygen pressure of 6.7 bar. Under these conditions, 79 % FDCA selectivity at full conversion was reported [23]. Therefore, the influence of reaction temperature on HMF oxidation was studied on unsupported Pd_3 NPs (prepared with 4:1 molar ratio of NaOH to Pd at 90 °C for 3 h) in the range 25-90 °C. The rate of HMF conversion was increased as the temperature increased (Figure 25). A time of 24 h was necessary to achieve a complete conversion of HMF at 25 °C. Here, the HMFCA was formed as the main product with 90 % yield. As the temperature was increased up to 50 °C, the HMFCA was still the major product. These results indicate that on Pd NPs the aldehyde group of HMF in the presence of base is more easily oxidized than the alcohol group of HMFCA as observed previously on Au based catalysts [119, 123, 125]. Raising the temperature up to 70 °C, the FDCA was formed as a major product with a good yield. Below 90 °C, the rate of the oxidation of HMFCA to FFCA is obviously slower than the rate of the oxidation of FFCA to FDCA. This behaviour was also observed on Au based catalysts where oxidation of HMFCA to FFCA was considered as rate determining step in HMF oxidation [123, 125]. On contrary, the rate of oxidation HMFCA to FFCA was similar to the rate of the oxidation of FFCA to FDCA at 90 °C. Furthermore, the highest yield of FDCA of 90 % was obtained at 90 °C.

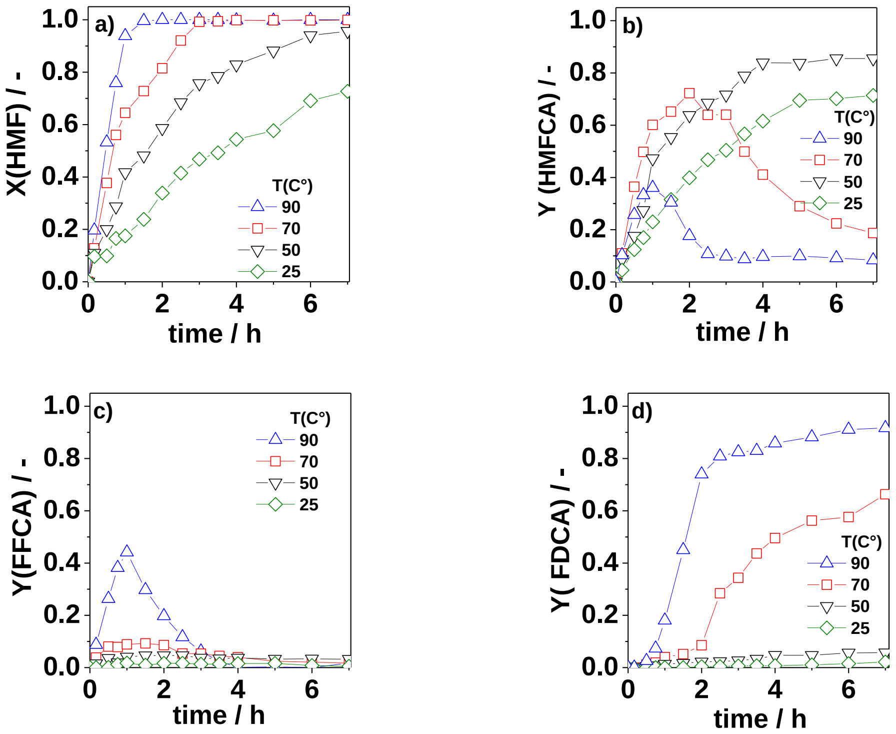

Figure 25. Influence of reaction temperature on the HMF oxidation using Pd_3 NPs as catalyst. Reaction conditions: HMF (0.4 mmol), H_2O (20 mL), HMF:Pd= 100 (mol/mol), (1 mL/h) aq. NaOH (0.5 M), O_2 flow rate = 35 mL/min.

5.2.1.2 Effect of the particle size of Pd NPs

In order to study the influence of particle size on HMF conversion and products yield, the prepared differently sized NPs were applied under the reaction conditions of 35 mL/min oxygen flow, 90 °C with addition of aq. NaOH continuously. The results were summarized in Table 18. The HMF was fully converted within 4 h with the formation of HMFCA in minor amounts (3 %) in the absence of a catalyst. The HMF conversion is obviously lower compared to previous results at low oxygen flow of 4 mL/min but in presence of Pd NPs (Figure 24) [195]. In the absence of the catalyst, compounds of degradation of HMF [levulinic and formic acid] were detected as side products [119]. Using Pd precursor (Na_2PdCl_4) as a catalyst leads to a complete conversion of HMF within 4 h with 10 % HMFCA yield (Entry 2, Table 18). These results indicate that HMF oxidation cannot proceed over Pd^{2+} ions. When the Pd NPs catalyst presented in the reaction solution, a clear decrease of the amount of side products were detected (Entries 3-6, Table 18). An increasing in the particle size of NPs leads to a decrease in the yield of FDCA (Pd_1, d = 4.4 nm) to 81 % (Pd_2, d = 1.9 nm) to 90 % (Pd_3, d = 1.8 nm) (Entries 3-5, Table 18).

Based on the reported literature, the particle size was affecting product distribution using supported Au-Cu NPs. The yield of HMFCA was increased to be higher than yield of FDCA after calcination of catalyst (calcination step was accompanied by an increase in NPs size). The authors stated that the oxidation of HMFCA might be more sensitive to particle size than the oxidation of HMF [119].

It was observed that the reaction solution became slightly yellow colored if the yield of FDCA is high, otherwise, a heavily colored will be observed. The observation of the color of reaction solution was previously reported and the degradation of HMF was suggested as a reason of having a strong coloring [124].

Table 18. Catalytic results of differently sized Pd NPs in HMF oxidation.

Entry	Catalyst	Dmean(TEM) [nm]	X(HMF) [%]	Y(HMFCA) [%]	Y(FFCA) [%]	Y(FDCA) [%]
1	blank	–	>99	3	-	0
2	Na_2PdCl_4	–	>99	10	0	0
3	Pd_1	4.4±1.6	>99	28	0	61
4	Pd_2	1.9±0.7	>99	3	8	81
5	Pd_3	1.8±0.5	>99	8	0	90

Reaction conditions: HMF (0.4 mmol), H_2O (20 mL), HMF:Pd= 100 (mol/mol), O_2 flow rate (35 mL/ min), 90 °C, and 7 h as the reaction time.

Figure 26 shows the temporal evolution of HMF conversion and product yield in the presence of differently sized Pd NPs. The HMF conversion was accomplished within 1.5 h on Pd_3 (mean diameter: 1.8 nm) and Pd_2 (mean diameter: 1.9 nm). While a complete conversion of HMF was obtained in a longer time of (2 h) on Pd_1 (mean diameter: 4.4 nm).

The intermediates HMFCA and FFCA were detected in the initial stage of the oxidation reaction independent of the size of the Pd NPs used. The maximum yield of HMFCA was achieved in a longer time of 2 h for the largest NPs (Pd_1) compared to those NPs which have a smaller particle sizes (Pd_2 and Pd_3) and then the yield of HMFCA remained constant without further oxidation up to 7 h. The maximum yield of FFCA was also achieved in a longer time of 2 h for the large particles compared with those smaller particle sizes (Pd_2 and Pd_3), but FFCA was further oxidized independent on the NPs used (Figure 26c). The highest yield of FDCA of 90 % was obtained when using the smallest particles of NPs (Pd_3, mean diameter =1.8 nm).

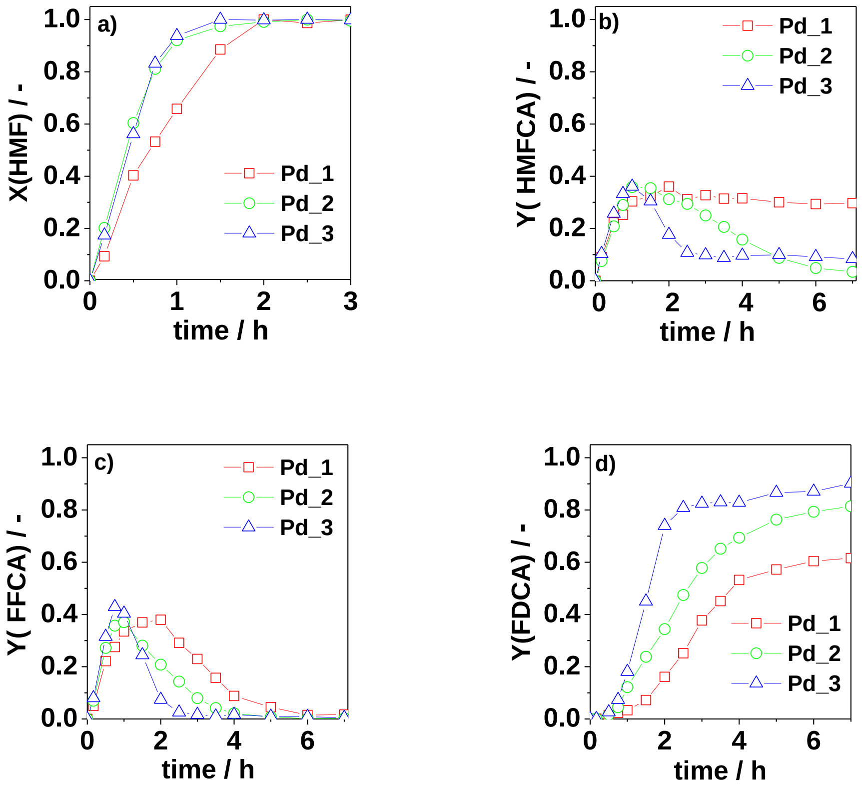

Figure 26. Plots of a)- HMF conversion and yields of b)-HMFCA – c) FFCA – and d) FDCA) versus time on differently sized Pd NPs. Reaction conditions: HMF (0.4 mmol), H_2O (20 mL), HMF:Pd = 100 (mol/mol), O_2 flow rate (35 mL/min), 90 °C, addition of (1 mL/h) aq. NaOH (0.5 M), 7 h as the reaction time.

In general, it is believed that NPs activity was increased as the particle size decreased because of a higher number of surface atoms, and thus a higher amount of coordinately unsaturated metal sites [196-200]. The number of Pd surface atoms (S_{atoms}) was calculated using equations which were given in Section 7.2, Appendix [185, 186].

Table 19 summarizes the mean number of Pd atoms in a single particle (n), the number of Pd atoms in the solution (N_{atoms}), and the number of Pd surface atoms (S_{atoms}) as well.

Table 19. The number of Pd surface atoms.

Entry	Dmean(TEM) [nm]	n	N_{atoms}	S_{atoms}
Pd_1	4.4±1.6	3134	$1.20\text{x}10^{20}$	$3.41\text{x}10^{19}$
Pd_2	1.9±0.7	252		$6.31\text{x}10^{19}$
Pd_3	1.8±0.5	214		$7.54\text{x}10^{19}$

The results showed that formation of FDCA was faster in the presence of smaller particle sizes. A different amount of active surface site of the used NPs might be the reason for the variations in the catalytic performance of the differently sized Pd NPs. It could be observed that with increasing number of active surface sites, deactivation is shifted to longer reaction times.

A rough approximation of the intrinsic TOF was calculated using initial activity (HMF conversion after 10 min) related to the Pd amount used in the oxidation reaction (0.004 mmol) and the Pd dispersion which was estimated from the mean diameter of Pd NPs (Table 14, TEM) divided by 1.12) [20]. TOF values were between 0.06 (Pd_3) and 0.1 s^{-1} (Pd_1). So it is difficult to judge whether the HMF transformation is structure sensitive or not as investigated for the oxidation of benzyl alcohol on supported Pd NPs [20].

Since the Pd NPs prepared were stabilized by PVP, it cannot completely exclude a possible role of PVP. It is believed that the difference in the catalytic performance at short reaction times are independent on the variations of interaction between polymer functional groups and the NPs surface [62]. A black precipitation was observed in the reaction solution independent on the NPs used after the reaction time of 7 h. This could be attributed to the fact that at high basicity of (NaOH:HMF = 8.75: 1 mol/mol) after 7 h part of the protecting agent (PVP) might be lost. Thus, the result suggests depositing the NPs onto carrier materials in order to get catalytic materials with more stable performance.

5.2.1.3 Influence of storing Pd NPs on catalytic performance

As stated before that it is necessary to deposit the Pd NPs onto carrier materials. For this regard, the prepared NPs were tested again in HMF oxidation after several days of their synthesis in order to find out whether they can show the same catalytic results as obtained on the freshly used ones. The synthesized NPs were stored in synthesis solution under atmospheric conditions. The pH solution of synthesized NPs was different because a different molar ratio of NaOH:Pd was used in the NPs synthesis, as follows: pH (Pd_1) = 3.4, pH (Pd_2) = 7.7 and pH (Pd_3) = 11.1. The catalytic performance of stored Pd_1 (storage time = 30 days) was clearly different compared to the corresponding freshly prepared NPs. The capability of NPs to oxidize HMFCA further was decreased after storage (storage time = 30 days) and the amount of side products was clearly increased as well (Entry 1, Table 20). The catalytic performance of the stored Pd_2 (storage time = 3 days), which were prepared at 2:1 molar ratio of the NaOH:Pd was similar to the corresponding freshly prepared one. But when these NPs were tested after 14 days, a higher yield of HMFCA connected with a lower yield of FDCA were observed compared to that on the freshly prepared Pd_2 (Entry 2, Table 20). Interestingly, the stored Pd_3 (storage time = 14 or 30 days), which were synthesized at 4:1 molar ratio of NaOH:Pd, showed an identical catalytic performance, compared to the freshly prepared one (Entry 3, Table 20).

Table 20. Catalytic performance of Pd NPs in HMF oxidation after storage in the synthesis solution.

Entry	NPs	NaOH:Pd	Duration [days]	X(HMF) [%]	Y(FFCA) [%]	Y(HMFCA) [%]	Y(FDCA) [%]
1	Pd_1	1:1	fresh	>99	2	28	61
			30	>99	2	50	7
2	Pd_2	2:1	fresh	>99	0	3	81
			3	>99	1	4	83
			14	>99	6	43	51
3	Pd_3	4:1	fresh	>99	0	8	90
			14	>99	0	4	93
			30	>99	0	10	90

Reaction conditions: HMF (0.4 mmol), H_2O (20 mL), HMF:Pd= 100 (mol/mol), oxygen flow (35 mL/min), (1 mL/h) aq. NaOH (0.5 M) 90 °C, 7h.

SAXS analysis was used for the stored Pd NPs after 14 or 30 days to follow the changes in particle structures (Figure 27). No differences were observed in the scattering profiles between the stored Pd_2 or Pd_3 fractions (storage time = after 14 days) and the freshly prepared NPs counterparts. Since the shape of SAXS profile relies strongly on the particle size of the NPs, the observed identical scattering profiles indicate that no change in the particle size of these NPs during the storage in synthesis solution was observed. However, this observation was expected for Pd_3, where no change in the catalytic performance was observed, but it was unexpected for Pd_2 which showed different catalytic results after storing the NPs (storage time of 14 days). It could be assumed that during this time interval the surface of Pd NPs was affected by a post process. In contrast, a clear difference in scattering profiles of the Pd_2 after storing (storage time = 30 days) was observed compared to the freshly prepared NPs counterparts. The shift of the scattering intensity towards lower q-values for the curve obtained after 30 days refers to a slight increase of particle size with time. The maximum of the volume weighted particle radii distribution which was derived from the fitting of the scattering curve shifted from 3.0 nm to 3.2 nm (as inserted in Figure 27a). Synchronously, the value of the invariant Q was decreased by about 10 % which relies only on volume fraction of the Pd-NPs in the solution [201] and, since no precipitation was observed, the decrease of Q can be explained only by a solution of the Pd NPs. It was reported that the size of Pd NPs in ethylene glycol in presence of the stabilizing agent PVP can be changed by an oxidative etching process. Here, a Cl^-/O_2 pair interacts with the surface of NPs under formation of $[PdCl_4]^{2-}$. Then, the $[PdCl_4]^{2-}$ which is newly formed can again be reduced leading to growth in the particle size [202]. Although the temperature at which the NPs were stored was lower (RT instead of 120 °C), it is believed that such processes could occur during the storage of the NPs, but with significantly lower rates. Furthermore, the results indicate that the extent of such post processes depends strongly on the pH of the solution in which the NPs were stored. The observed decrease in the capability of the NPs to oxidize HMFCA after storing might be explained by interaction of the NPs surface with O_2/Cl^- pairs.

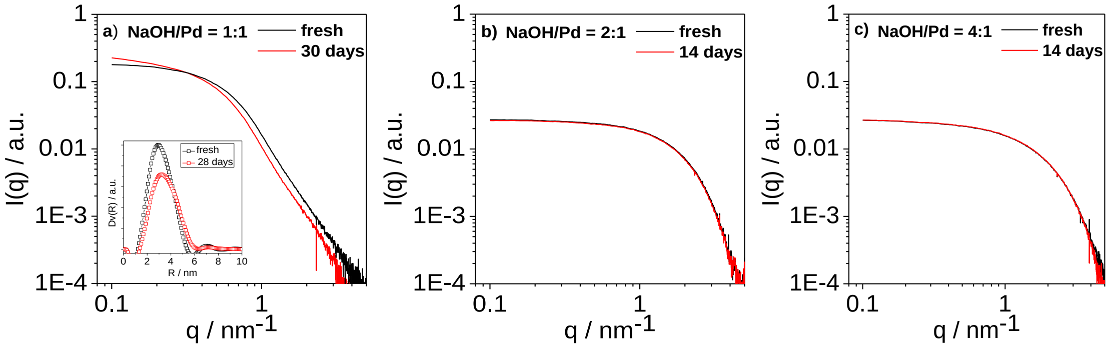

Figure 27. Scattering profiles of freshly synthesized and stored Pd NPs synthesized at different NaOH/Pd ratio a)- 1:1 (Pd_1), b)- 2:1 Pd_2, and c)- 4:1 (Pd_3).

In conclusion, the following factors should be beared in mind for the preparation of heterogeneous catalyst by deposition of pre-formed nanoparticles onto supports. The pre-formed nanoparticles which have larger particle sizes should be deposited directly after synthesis onto the support. Otherwise, the properties of the NPs will change over time. On contrary, NPs with smaller particle sizes (mean diameter ≤ 2.0 nm) can be stable for longer times depending on the media used for synthesis and storage. If the NPs have been synthesized and stored in neutral medium, then the NPs should be deposited directly after synthesis. In our work, NPs which had been synthesized and stored in alkaline solution did not show a change of properties after one month storage time. Thus, it is possible to use them for the preparation of heterogeneous catalysts within this period of time.

5.2.2 HMF oxidation on supported Pd NPs with base addition

5.2.2.1 Effect of the support

The previous results showed that the highest yield of FDCA was obtained with the smallest particle size (Pd_3, mean diameters = 1.8 nm). Therefore, Pd_3 were chosen to deposit onto different supports. The results are summarized in Table 21. Compared to unsupported Pd_3 NPs (Table 18), Pd/HT_30, Pd/KF/Al_2O_3 and Pd/ZrO_2/La_2O_3 yielded FDCA with ≥ 90 % at full HMF conversion (Entries 1-3). The Pd/TiO_2 and Pd/Al_2O_3 catalysts showed clearly a lower FDCA yield and an inferior carbon mass balance compared to other supported Pd catalyst (Entries 4-5). HMFCA was detected in all experiments of supported materials with yields between 1 and 19 % while the yield of FFCA was always lower than 4 %. In order to exclude that the reaction might be proceeded in the presence of unloaded support, additional experiments were carried out under the identical reaction conditions using unloaded supports (Entries 6-8). The HMF was completely converted, but HMFCA was formed with low amounts. Thus, high amounts of unknown products were formed. Similar results were obtained for those experiments, where no catalyst or Pd precursors were used (Entries 1-2, Table 18).

Table 21. Catalytic results of HMF oxidation (X- HMF conversion, Y– product yield) on unloaded supports and Pd/support materials with continuous addition of a homogeneous base (aq. NaOH).

Entry	Catalyst	X (HMF) [%]	Y(FFCA) [%]	Y(HMFCA) [%]	Y(FDCA) [%]	Balance
1	Pd/HT_30	>99	0	2	96	0.98
2	Pd/ZrO_2/La_2O_3	>99	0	7	90	0.97
3	Pd/KF/Al_2O_3	>99	0	7	91	0.98
4	Pd/Al_2O_3	>99	3	9	78	0.90
5	Pd/TiO_2*	>99	2	19	62	0.83
6	ZrO_2/La_2O_3	>99 (5h)	<1	5	<1	0.07
7	Al_2O_3	99 (6h)	<1	5	0	0.06
8	TiO_2	>99 (5h)	1	4	<1	0.06

Reaction conditions: HMF (0.4 mmol), H_2O (20 mL), molar ratio of HMF:Pd = 100, O_2 flow rate = 35 mL/min, 90 °C, (1 mL/h) aq. NaOH addition (0.5 M), 8 h and *7 h as the reaction time.

Figure 28 shows the temporal evolution of HMF conversion and product yield in the presence of differently supported Pd NPs. The HMF was fully converted within 1.5 h on all these catalysts, hence there is no obvious difference between the different catalysts regarding HMF conversion (Figure 28a). Preliminary experiments showed that the rate of HMF conversion and the intermediates (HMFCA and FFCA) transformation were influenced by the rate of base addition.

The intermediates HMFCA and FFCA were also observed in all cases. The maximum yield of HMFCA was observed at slightly earlier times than with FFCA (Figure 28b vs. Figure 28c). The lowest amount of HMFCA was observed for Pd/HT. This could be attributed to the nature of support. Previously, it was reported that the oxidation of hydroxyl group is considered to be the rate determining step on Au/HT (oxidation of HMFCA to FFCA). The intermediate HMFCA is oxidized to FFCA by the formation of metal alcoholate species via metal–hydride shift which was facilitated by the basicity of HT [125]. The HMFCA concentration remained unchanged after 2 h. In contrast, the FFCA intermediate was completely oxidized to FDCA. This was already observed for the unsupported Pd NPs. This observation led to the assumption that the supported Pd NPs lost their capability to oxidize HMFCA completely after 2 h. The loss of catalytic activity for the further oxidation of the intermediate might be caused by the adsorption of the organic molecules which are formed during the reaction on the active site of Pd surface as previously reported on Au/CeO_2 and Au/TiO_2 catalysts [123]. This behavior was already observed for the experiments on unsupported catalyst, where it was assumed that the oxidation of the intermediates HMFCA and FFCA occurred on different surface sites of the catalyst [195]. The same assumption can be applied in the case of supported catalyst.

The fastest formation of FDCA, connected with the highest yield, was observed for Pd/HT_30. Compared to the other materials, FDCA formation began almost immediately after the reaction was started. It was previously reported for Au/HT that the conversion of both intermediates (HMFCA and FFCA) occurred rapidly because of the basicity of the support, and hence resulting in a high yield of FDCA [125]. Additionally, experiments were carried out with FDCA (0.4 mmol) as reactant instead of HMF under the same reaction conditions. In the presence of Pd/ZrO_2/La_2O_3, Pd/TiO_2 or Pd/Al_2O_3 the FDCA stayed constant within the time interval of 5 h. Thus, FDCA degradation can be excluded as a reason for the observed differences in FDCA yield with different supported Pd.

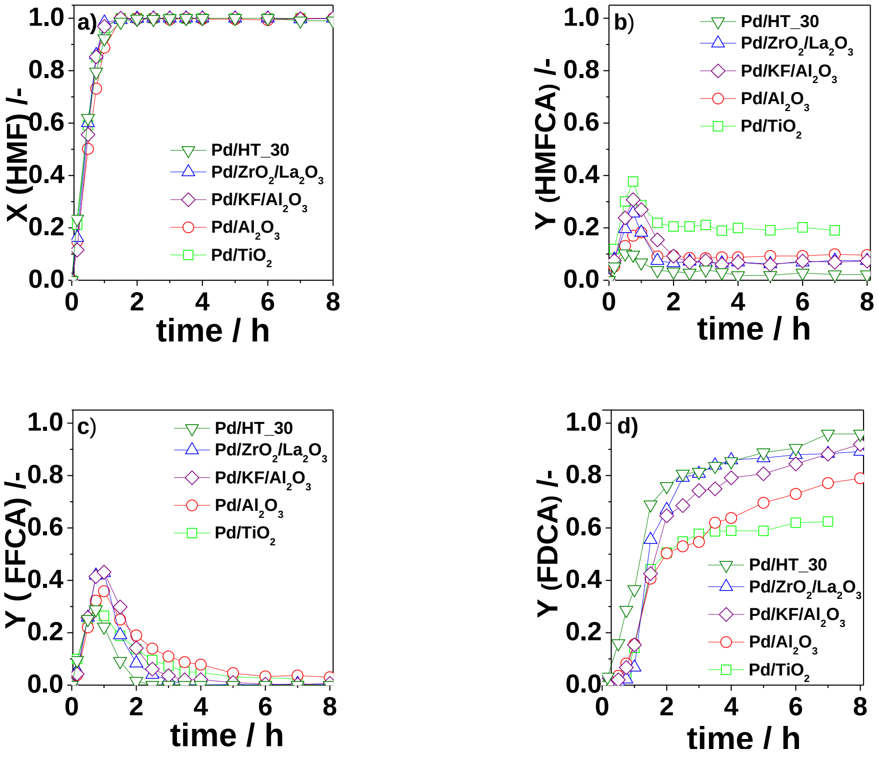

Figure 28. Plots of HMF conversion (a) and product yields (b-d) versus time on Pd/support catalysts (reaction conditions: HMF (0.4 mmol), H_2O (20 mL), HMF:Pd = 100 (mol/mol), O_2 flow rate (35 mL/min), 90 °C, (1 mL/h) aq. NaOH addition (0.5 M).

To study whether the HMF oxidation can be influenced by leached Pd species, the experiments were performed in the presence of the catalysts (Pd/TiO_2, Pd/ZrO_2/La_2O_3). The catalyst was separated from reaction mixture after one hour and the remaining solution was further reacted up to 8 h. The results showed that after catalyst-removal the amount of HMFCA, FFCA and FDCA remain unchanged (Figure 29, Entries a-b).

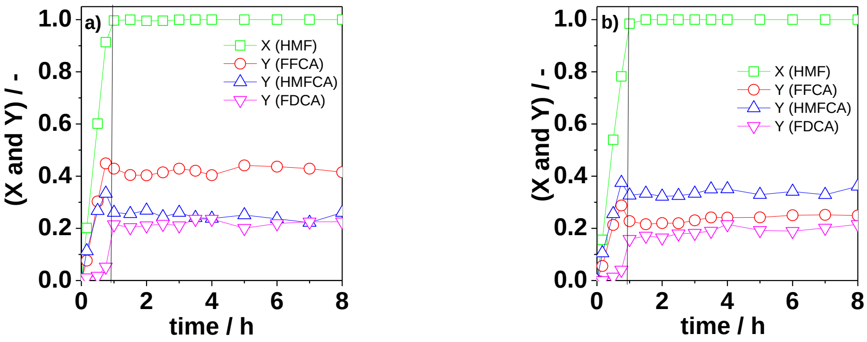

Figure 29. Plot of HMF conversion and products yield of HMF oxidation versus reaction time for a)- Pd/ZrO_2/La_2O_3 and b)- Pd/TiO_2 with (0-1 h) and without solid material (1-8 h) in the reaction mixture. Reaction conditions: HMF (0.4 mmol), H_2O (20 mL), HMF:Pd = 100 (mol/mol), O_2 flow rate (35 mL/min), 90 °C, (1 mL/h) aq. NaOH addition (0.5 M).

The obtained results suggest that either no Pd species leached from the catalyst or the leached amount of Pd species into reaction solution was not catalytically active anymore. The results of atomic absorption spectroscopy analysis (AAS) of the final reaction mixture after 8h showed that about 3 % of Pd leached out into the reaction solution from the Pd/TiO_2 catalyst and about 6 % for the experiment where the Pd/ZrO_2/La_2O_3 was used as catalyst. Since approximately 6 % Pd was detected in the reaction solution where Pd/ZrO_2/La_2O_3 was used catalyst, an additional experiment was therefore proceeded. However, the catalyst was separated from the reaction solution after 8 h and an additional amounts of both intermediates, HMFCA (0.08 mmol) and FFCA (0.156 mmol), were added to the reaction solution. No change in the concentration of these intermediates was observed even after 8 h (Figure 30). Thus, the HMF transformation was catalyzed by the Pd/support materials and not by Pd leached.

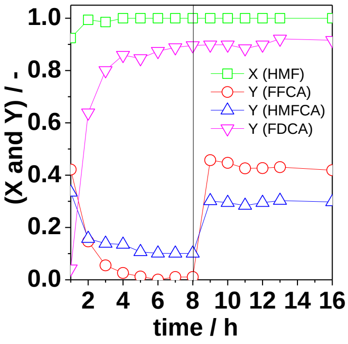

Figure 30. Plot of HMF conversion and products yield of HMF oxidation versus reaction time. Reaction conditions: HMF (0.4 mmol), H_2O (20 mL), Pd/ZrO_2/La_2O_3 catalyst (0-8 h) and without catalyst (8-16 h), HMF:Pd = 100 (mol/mol), O_2 flow rate (35 mL/min), 90 °C, (1 mL/h) aq. NaOH addition (0.5 M).

- **Reusability of the supported monometallic Pd nanoparticle catalysts**

Further experiments were carried out to study the reusability of Pd nanoparticle based material. For this reason, the Pd/ZrO_2/La_2O_3, Pd/TiO_2, and Pd/KF/Al_2O_3 catalysts were tested two or three times under identical experimental conditions using the recycled catalyst. After each experiment the reaction solution was centrifuged in order to remove the catalyst. Then the removed catalyst was washed once with distilled water and dried in the oven at 40 °C. Material loss (by sampling) for a single run was found to be ca. 7 % for Pd/ZrO_2/La_2O_3 and Pd/TiO_2. This value was obtained by weighting the material before and after reaction. Plots of HMF conversion and product yields versus time are shown in (Figures 50-52, Appendix). In all runs, a complete conversion HMF was within 1.5 h and the intermediate FFCA was completely oxidized to FDCA. In contrast, the oxidation of the intermediate HMFCA stayed constant after reaction times longer than 2 h in first run. The same observation was observed in the second and third runs regarding the HMFCA intermediate. These findings suggest that the loss of capability to oxidize HMFCA is a reversible effect. However, a slight decrease in the yield of FDCA was observed for each run. Table 21 summarizes the results of different runs after 8 h reaction time. For the Pd/ZrO_2/La_2O_3 catalyst, the yield of FDCA decreased slightly from 90 % in the 1st to 86 % in the 3rd run. In the same tendency, the FDCA yield was also decreased for Pd/TiO_2 (62 % → 54 %). It should be mentioned that Pd leaching from ZrO_2/La_2O_3 support decreased as the number of runs increased (6 % in 1st run, 3 % in 3rd run). The difference in FDCA yields between the first and the second run was larger on Pd/KF/Al_2O_3 catalyst (91 → 55 %). In all cases, an increase in HMFCA yield was detected as the number of runs increased. As reported, a slight decrease of the FDCA yield with an increasing number of runs was observed for catalyst Au/CeO_2 [123]. Pt-Bi/C catalyst showed a stable catalytic performance in HMF oxidation using $NaHCO_3$ as base [124].

Table 22. Results of reusability tests on Pd/support catalysts with continuous addition of homogeneous base; X (HMF) = 100%.

Catalyst	First use			Second use			Third use		
	Y% HMFCA	Y% FFCA	Y% FDCA	Y% HMFCA	Y% FFCA	Y% FDCA	Y% HMFCA	Y% FFCA	Y% FDCA
Pd/ZrO_2/La_2O_3	7	0	90	12	0	87	12	2	86
Pd/KF/Al_2O_3	7	0	91	43	0	55	-	-	-
Pd/TiO_2*	19	2	62	19	2	59	26	0	54

Reaction Conditions: HMF (0.4 mmol), H_2O (20 mL), HMF/Pd = 100 (mol/mol), O_2 flow rate: 35 mL/min, 90 °C, (1 mL/h) aq. NaOH addition (0.5 M), reaction time: 8 h (*7 h).

X-ray diffraction pattern of TiO_2, ZrO_2/La_2O_3, Al_2O_3, and KF/Al_2O_3 before and after Pd loading and after HMF oxidation are shown in Figure 31. Diffraction peaks of metallic Pd NPs were not observed because of the low Pd loading (0.5 wt %). No change of the diffraction pattern for TiO_2, ZrO_2/La_2O_3 and Al_2O_3 after deposition of Pd was observed and even also after the HMF oxidation in alkaline solution at 90 °C. A very broad signal was detected for those catalysts where Al_2O_3 and ZrO_2/La_2O_3 was used as support. This might be due to a small particle size and/or a high portion of amorphous phase. However, the diffraction pattern clearly changed after Pd loading and during HMF oxidation in the case of Pd/KF/Al_2O_3 catalyst (Figure 31d). The alumina structure stayed intact and during HMF oxidation a new phase of PdF_4 phase (PDF-Nr. 070-0717) was observed instead of the K_3AlF_6 phase (PDF-Nr. 000-0615) which was detected after Pd NPs deposition. In addition, new peaks were detected which are attributed to a K_2O phase (PDF-Nr. 013-0373). Thus, these variations of the phase compositions could be the reason for the observed changes in the catalytic performance in the 2nd run of the catalyst (FDCA yield: 1st use 91 %; 2nd use 55 %) and the high amounts of catalyst loss (33 %) in a single experiment of HMF oxidation as well.

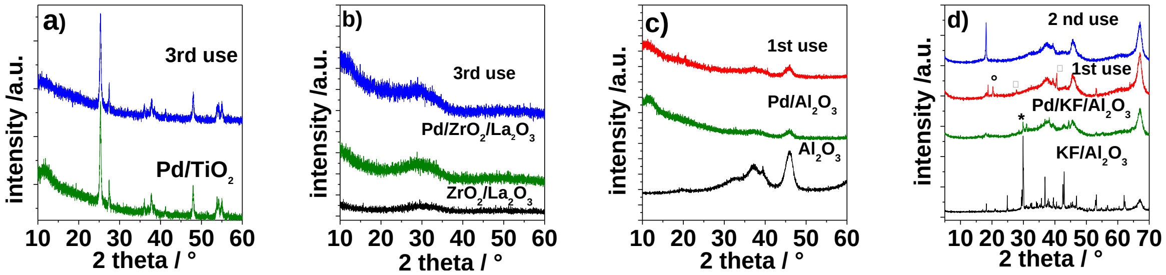

Figure 31. Influence of Pd NPs deposition and HMF oxidation on the XRD pattern of the Pd/support materials a)-TiO_2, b)-ZrO_2/La_2O_3. c)-Al_2O_3, and d)-KF/Al_2O_3 (*-K_3AlF_6, □-K_2O, ○-PdF_4).

The SEM images of the ZrO_2/La_2O_3 support with the images after Pd loading ($Pd/ZrO_2/La_2O_3$) and after using this catalyst in HMF oxidation are compared (Figure 32). No change of the morphology of the $Pd/ZrO_2/La_2O_3$ during the HMF oxidation was observed.

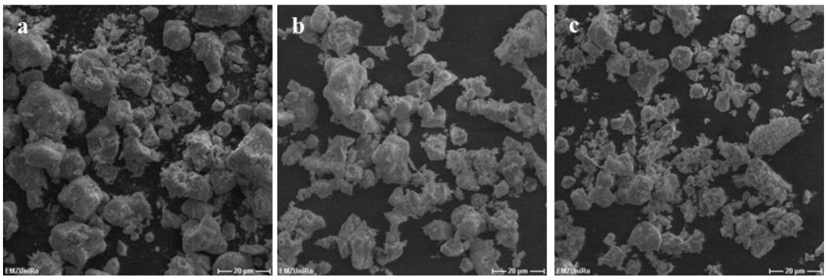

Figure 32. SEM images of (a) of the ZrO_2/La_2O_3 support, (b) $Pd/ZrO_2/La_2O_3$ (after Pd nanoparticle deposition and (c) after applying $Pd/ZrO_2/La_2O_3$ the catalyst three times in HMF oxidation.

The effect of HMF oxidation on the structure of Pd NPs on different supports was additionally studied by TEM. Figure 33 shows STEM-HAADF images of Pd/TiO_2, Pd/Al_2O_3, and $Pd/ZrO_2/La_2O_3$ catalysts after utilization in the HMF oxidation. As mentioned before, element mapping with EDX was used for $Pd/ZrO_2/La_2O_3$ to get more reliable results since the electron density of the ZrO_2/La_2O_3 support (La: atomic number 57, Zr: atomic number 40) is higher and similar compared to Pd (atomic number 46), respectively. The histograms of particle size distribution were derived from the images of each catalyst (as inserted in Figure 33). An increase in the mean diameter of the particles and width distribution of Pd-NPs for the catalyst after HMF oxidation was observed for Pd/TiO_2 (2.1 to 2.9 nm), Pd/Al_2O_3 (2.7 to 4.4 nm) and for ZrO_2/La_2O_3 (2.6 to 4.2 nm) compared to fresh catalysts. The values of the mean diameter of Pd NPs after use in HMF should be considered as approximations, because a large part of the Pd particles have not a spherical shape anymore. Thus, not only change in the particles size was observed but also in the shape of the Pd particles during HMF oxidation. The change of shape was mainly caused by aggregation of the formerly deposited small NPs. The occurrence of aggregations was also dependent on the used catalyst or more precisely on the used support. The strongest aggregation was observed for Al_2O_3. In the case of the ZrO_2/La_2O_3 support, the aggregated Pd seemed to be more elongated. The stronger aggregation on Al_2O_3 than on ZrO_2/La_2O_3 could come from the variations of the surface charge in basic solution (pH=10) derived from the negative zeta potential of ZrO_2/La_2O_3 support (-43 mV) compared with that for Al_2O_3 (24 mV). Such elongated Pd structures were previously observed when the polyvinylpyrrolidone (PVP) was substituted by a molecular stabilizer by means of a phase transfer to toluene at 100 °C [203].

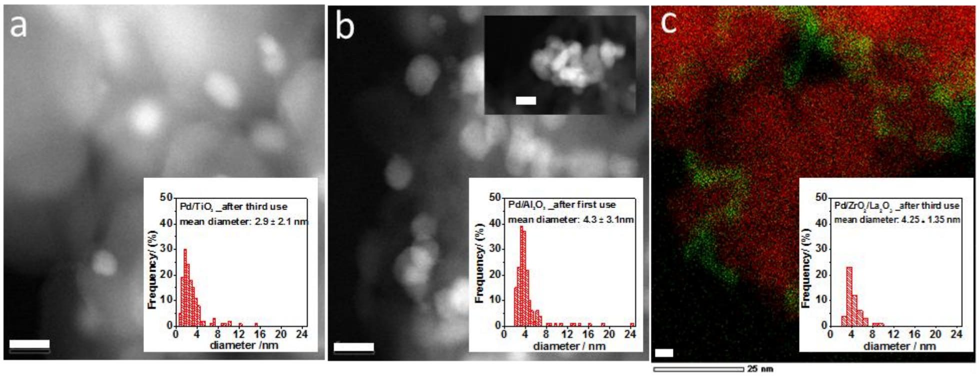

Figure 33. STEM-HAADF images of the used catalyst a)- Pd/TiO_2 (after 3 used, 144 particles), b)- Pd/Al_2O_3 (after 1 used, 177 particles) inserted in b shows the structure of a large Pd aggregate, scale bar: 5nm) and c)- EDX mapping for Pd/ZrO_2/La_2O_3 (after third used, 50 particles).

XPS analysis was used to characterize the fresh and used catalysts in order to obtain information about the electronic structure of the Pd NPs on the support before and after HMF oxidation. Figure 34 presents the XPS spectra of the fresh and used Pd/TiO_2 and Pd/ZrO_2/La_2O_3 catalysts. As mentioned before, the binding energy of Pd^{2+} (bivalent) is higher than for metallic Pd [190-192]. In fresh Pd/TiO_2 catalyst both metallic and bivalent Pd were detected (Figure 34a). The grey area represents the metallic Pd ($3d_{5/2}$ = 335.4 eV, $5d_{3/2}$ = 340.6 eV). While the dark gray area represents the bivalent Pd ($3d_{5/2}$ = 337.0 eV, $3d_{3/2}$ = 342.4 eV). The bivalent Pd was partly reduced for the used catalysts. This result was derived from the increasing intensity of the peak area of metallic Pd compared with to the bivalent one. The XPS spectra of Pd/ZrO_2/La_2O_3 catalyst are shown in Figure 34 (b -c). The interpretation of the Pd3d spectra was complicated for the Pd/ZrO_2/La_2O_3 catalyst because of the overlap of peaks of Pd3d and Zr3p. Nevertheless, it was possible to determine the maximum of the $Pd3d_{3/2}$

peak (340.4 eV for the fresh sample, 341.4 eV after use). The Pd3p$_{1/2}$ electrons were additionally recorded (Figure 34c). In both samples (fresh and utilized), the maximum was observed at 558.6 eV. This indicates that the most part of Pd is metallic and that the electronic structure of the Pd NP is not changed by the oxidation reaction Figure 34 (b-c). As mentioned before, the identical Pd NPs were used to prepare heterogeneous catalysts (Pd/TiO$_2$ and Pd/ZrO$_2$/La$_2$O$_3$. Thus, the presence of the bivalent Pd in the XPS spectra of Pd/TiO$_2$ and its absence in the case of Pd/ZrO$_2$/La$_2$O$_3$ indicates the influence of the support on the electronic structure of the deposited Pd NPs.

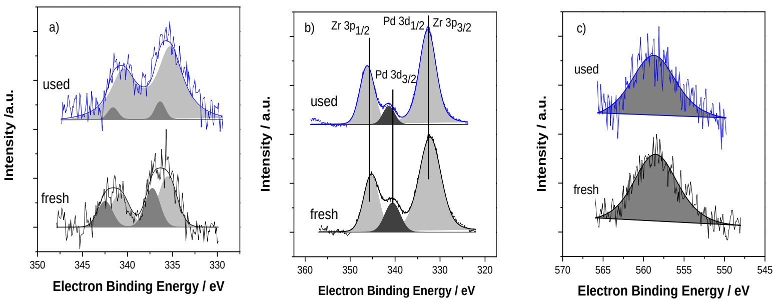

Figure 34. XPS spectra of a) the Pd3d electrons from the fresh and used (3x) Pd/TiO$_2$ catalysts, b) the Zr3p and Pd 3d electrons and c) the Pd3p electrons from the fresh and used (3x) Pd/ZrO$_2$/La$_2$O$_3$ catalysts.

Previously, it was reported that the interactions between the Pd clusters and TiO$_2$ are strong [190]. Ti2p electrons were additionally recorded for the used and fresh catalysts to confirm this strong interaction in our studies (Figure 35). For the fresh catalyst only a Ti^{4+} peak was detected but in the used catalyst the XPS signal is composed of peaks of Ti^{4+} and Ti^{3+}. Obvious evidence from the interaction of Pd NPs with the TiO$_2$ support is the presence of Ti^{3+} during HMF reaction. Furthermore, such interactions might be the reason for the short time deposition during the preparation of Pd/TiO$_2$, hence a faster adsorption of the Pd NPs on TiO$_2$ compared to the other supports.

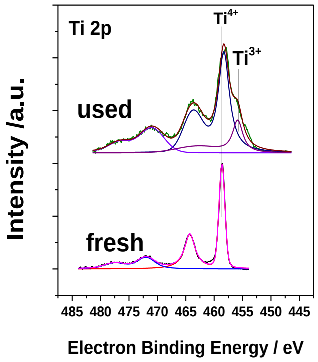

Figure 35. XPS spectra of the Ti2p electrons from the fresh and used (3x) Pd/TiO$_2$ catalyst.

Previously, it was proposed that molecular oxygen has an indirect role in HMF oxidation by scavenging the electrons deposited onto the supported metal particles (Pt and Au based materials) [129]. The peak of the bivalent Pd species decreased during the HMF oxidation as shown in Figure 34a. This might be occurred because the Pd NPs accept electrons which were liberated during HMF oxidation. The formation of Ti^{3+} during the reaction might be explained as follows: Since the formation of byproducts is relatively high in the HMF oxidation on Pd/TiO_2 catalyst. These byproducts might block active surface sites of the catalyst, hence, to make them inaccessible for molecular oxygen. Therefore, electrons which are released during the oxidation reaction might be transferred from the NPs to the support, thus, to reduce Ti^{4+} partly to Ti^{3+} in TiO_2.

It is worth mentioning that not only a low amount of Pd leached onto the support was observed during the oxidation reaction, but also a decrease of the amount of PVP on the support surface. This was evident by a lower amount of nitrogen on the support surface after the reaction (Table 23). This might be caused by the degradation of PVP. Those NPs which were formerly firmly embedded in the polymer could immigrate to the support surface or into the liquid phase. On the support surface they could undergo e.g. aggregation reactions, and thus form aggregated Pd structures, as already observed in the STEM images (Figure 33). Since good adsorption of PVP was observed for alumina, the amount of Pd NPs which are embedded in adsorbed polymer should be the highest. However, the largest aggregated Pd structures were observed for the alumina support after HMF oxidation. Differences in surface charge between the supports ZrO_2/La_2O_3 and Al_2O_3 in basic solution are indicated by the more negative zeta potential of the respective support (pH 10: -43 mV compared to pH 10: -24 mV). This could be another reason for a lower degree of aggregation of Pd NPs on ZrO_2/La_2O_3 compared to Al_2O_3. Degradation of PVP could use as an interpretation for comparable catalytic performance in the recycling experiments, despite the observed Pd leaching. Surface sites formerly blocked by PVP might become accessible during these processes. The low differences in FDCA yield between the consecutive runs in the recycling experiments might be attributed to the formation of Pd aggregates composed of formerly smaller particles. In such structures the Pd NPs would only lose a small part of their surface. Thus, large parts of the previous structure should still remain intact

Table 23. Composition of the near-surface region of the fresh and used catalysts (by XPS).

Entry	Catalyst		Pd	N	Ti
1	Pd/TiO_2	fresh	0.009	0.039	1
2		used (3x)	0.008	0.014	1
			Pd	N	Zr
3	Pd/ZrO_2/ La_2O_3	fresh	0.194	0.295	1
4		used (3x)	0.112	0.129	1

5.2.2.2 Influence of modified palladium nanoparticles on HMF oxidation

The formation of the highest amount of side products during the HMF oxidation was obtained for Pd/TiO_2. However, this support showed the strongest interaction with Pd NPs. This strong interaction led to a decrease of changes in the Pd structure and in the particle size of NPs, and also to a decrease of the amount of Pd leaching during the oxidation reaction in alkaline aqueous solution. Thus, these observations have been considered as promising results for our further studies concerning the modification of the surface of Pd nanoparticles with the addition of a second metal. The modification could lead to a decrease of side product formation as observed on monometallic Pd/TiO_2 catalyst (Section 5.2.2.1). The pre-formed Pd NPs (mean diameter =1.8 nm) were modified by adding a second metal to obtain bimetallic Pd-M NPs (M = Ag, Cu, or Au). The prepared bimetallic catalysts were used in the HMF oxidation under the identical reaction conditions. Titania supported Pd-Cu NPs catalyst (4:1 molar ratio of Pd to Cu) showed a superior catalytic performance and resulted in 93 % FDCA yield at full HMF conversion (Entry 3) which is better compared to those experiments on the Pd-Cu catalyst (Pd:Cu = 10:1 mol/mol) catalyst and monometallic Pd counterpart as well (Entries 1-2, Table 24). Previously, it was reported that an alloyed Au-Cu/TiO_2 gave a higher FDCA yield compared to monometallic Au catalyst counterparts. It was attributed to the presence of the second metal (copper) in the active site of the catalyst [119]. A higher yield of FDCA (≥ 86 %) was also obtained using Pd-Ag catalysts (10:1 or 4:1 molar ratio of Pd to Ag) compared to the monometallic Pd catalyst (Entries 4-5, Table 24), whereas an obvious decrease of FDCA yield to 50 % was observed for the Pd-Au catalyst (Pd:Au = 4:1 mol/mol) (Entry 6).

Based on the XPS results (Section 5.1.4), we cannot attribute the difference in the catalytic performance of the bimetallic Pd catalysts to the oxidation state of the Pd NPs. As described before, the addition of the second metal changed the oxidation state of the Pd NPs. In the case of copper addition only Pd bivalent is present, while the addition of Au led to a reduction of Pd^{2+} slightly. The lowest amount of Pd bivalent was observed when Ag was present in the catalyst. However, the results showed that a similar activity was observed for all these bimetallic catalyst. Higher yields of FDCA connected with lower amount of side products were obtained for Pd-Cu and Pd-Ag catalysts. It was assumed that the second metal (Ag or Cu) was located near the surface of nanoparticles and therefore has changed the surface structure of the NPs. The addition of gold showed a worse catalytic behaviour compared to the other bimetallic (Pd-Ag and Pd-Cu) and even to monometallic Pd catalysts. This could be attributed to the high activity of gold which led to an increased activity of the catalyst for HMF degradation pathways rather than oxidation of the reactants.

Table 24. Catalytic results of HMF oxidation (X- HMF conversion, Y – product yield) on Pd-M/support materials with continuous addition of a homogeneous base (aq. NaOH).

Entry	Catalyst	[1]Pd:M mol/mol	X (HMF) %	Y(FFCA) %	Y(HMFCA) %	Y(FDCA) %	Balance
1	Pd/TiO_2*	-	>99	2	19	62	0.83
2	$Pd\text{-}Cu/TiO_2$	10:1	>99	0	20	80	1
3	$Pd\text{-}Cu/TiO_2$	4:1	>99	0	0	93	0.93
4	$Pd\text{-}Ag/TiO_2$	10:1	>99	0	0	86	0.86
5	$Pd\text{-}Ag/TiO_2$	4:1	>99	1	1	88	0.90
6	$Pd\text{-}Au/TiO_2$	4:1	>99	1	15	50	0.66

Reaction conditions: HMF (0.4 mmol), H_2O (20 mL), molar ratio HMF/ Pd = 100, O_2 flow rate = 35 mL/min, 90 °C, (1 mL/h) aq. NaOH addition (0.5 M), 8 h and *7 h as the reaction time, [1]nominal molar ratios.

Figure 36 shows the comparison of the temporal evolution of HMF conversion and product yield in the presence of $Pd\text{-}Cu/TiO_2$ and monometallic Pd/TiO_2 catalysts. HMF was fully converted within 1.5 h in all three used catalysts (Figure 36a). As mentioned before, the rate of HMF conversion is affected by the rate of base addition. The intermediates HMFCA and FFCA were detected in the initial stage of the oxidation reaction independent on the used catalyst. The maximum concentration of both intermediates was achieved approximately at the same time around 1 h after start of the reaction, for all the used catalysts. The lowest concentration of HMFCA of 28 % at 1 h was obtained with $Pd\text{-}Cu/TiO_2$ (Pd:Cu = 4:1 mol/mol). The presence of higher Cu amounts (Pd:Cu= 4:1 mol/mol) led to an increase of the catalyst ability for the oxidation of the intermediate HMFCA completely (Figure 36b). The FFCA was oxidized to FDCA within 4 h for all the used catalysts (mono- and bimetallic catalyst) (Figure 36c). This was observed for the unsupported monometallic catalyst. The difference in the yields of the HMFCA intermediate led to different yields of FDCA. The highest yield of FDCA in combination with the lowest amount of side products (derived from carbon mass balance) was obtained with Pd-Cu/TiO_2 (Pd:Cu= 4:1 mol/mol) catalyst (Figure 36d).

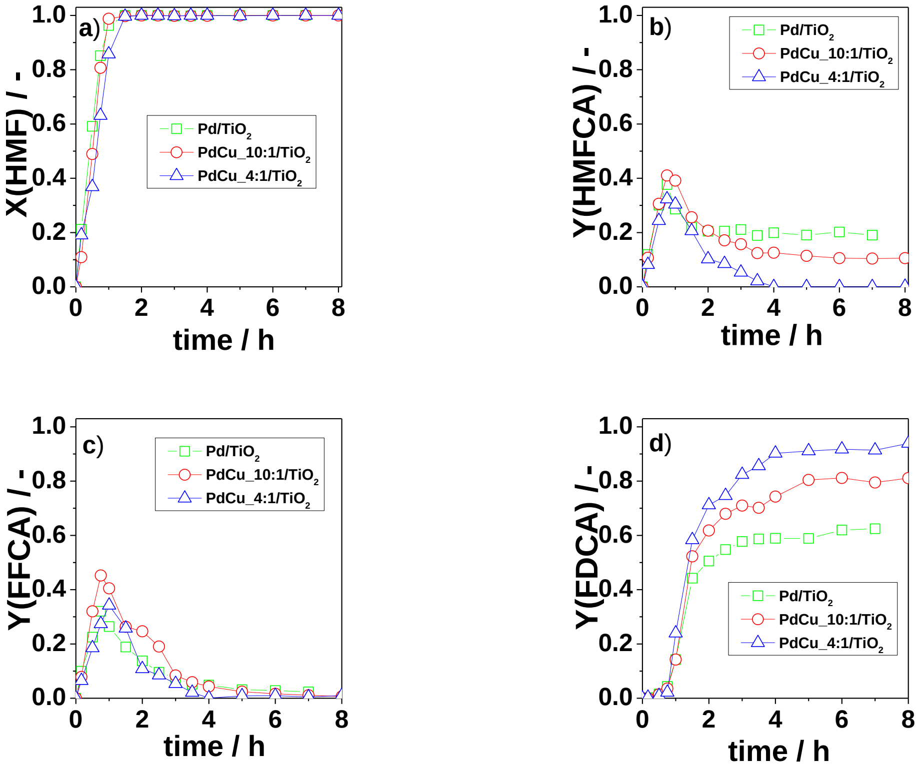

Figure 36. Plots of HMF conversion (a) and product yields (b-d) versus time on Pd/TiO_2 and Pd-Cu/TiO_2 catalysts. Reaction conditions: HMF (0.4 mmol), H_2O (20 mL), HMF:Pd = 100 (mol/mol), O_2 flow rate (35 mL/min), 90 °C, (1 mL/h) aq. NaOH addition (0.5 M).

Figure 37 shows the comparison of the temporal evolution of HMF conversion and product yield in the presence of Pd-Ag/TiO_2 catalyst with the monometallic Pd/TiO_2. HMF was fully also converted within 1.5 h with all three used catalysts (Figure 37a). The intermediates HMFCA and FFCA were detected in the initial stage of the oxidation reaction independent of the used catalyst. The intermediate HMFCA was achieved its maximum at the time interval of 1 h for all catalysts. An increase in the silver content in the catalyst led to increased oxidation rate of HMFCA. Thus, the lowest concentration of HMFCA of 10 % at 1h was detected for Pd-Ag/TiO_2 (Pd: Ag = 4:1 mol/mol) (Figure 37b). The HMFCA was completely oxidized on Pd-Ag catalyst, but the transformation of HMFCA was stopped after 2h on monometallic counterparts. FFCA was completely oxidized to FDCA within 4 h on all the used catalyst (Figure 37c). Before the concentration of both intermediates (FFCA and HMFCA) reached the maximum, FDCA started to form. A higher yield of FDCA ≥ 86 % was obtained with Pd-Ag/TiO_2 catalysts (Pd:Ag = 10:1 or 4:1 mol/mol) (Figure 37d).

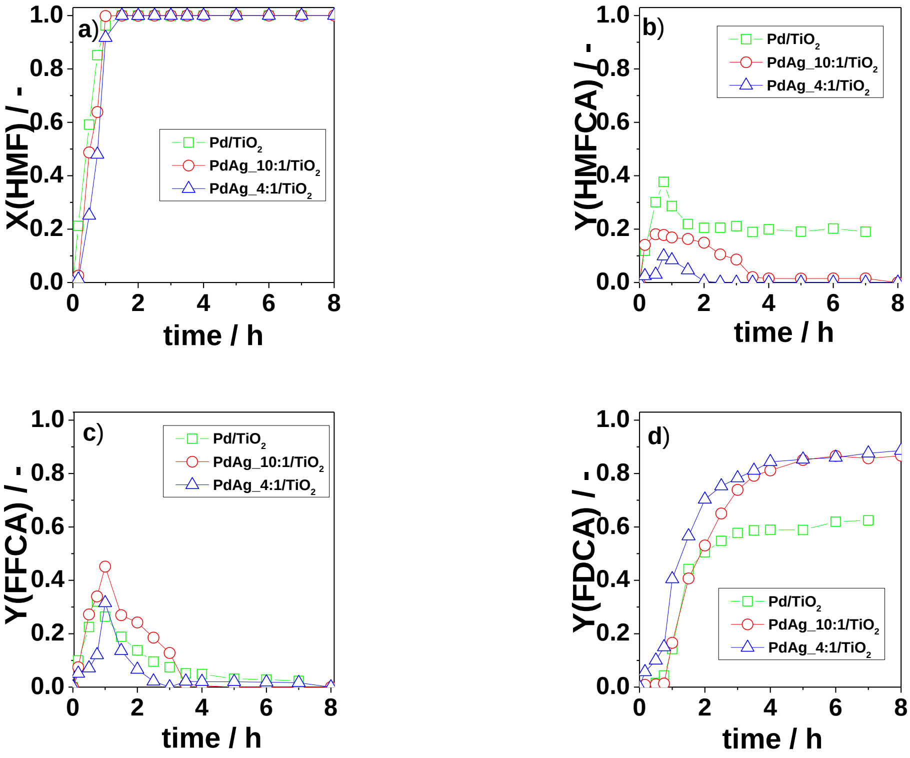

Figure 37. Plots of HMF conversion (a) and product yields (b-d) versus time on Pd/TiO_2 and Pd-Ag/TiO_2 catalysts. Reaction conditions: HMF (0.4 mmol), H_2O (20 mL), HMF:Pd = 100 (mol/mol), O_2 flow rate (35 mL/min), 90 °C, (1 mL/h) aq. NaOH addition (0.5 M).

In conclusion, the addition of the second metal Ag or Cu to monometallic Pd catalyst increased the capability of the catalyst to oxidize the HMFCA completely which is considered as a critical step in HMF oxidation. Moreover, it prevents the catalyst from fast deactivation which was observed for the monometallic Pd catalysts. Furthermore, the amounts of byproducts were clearly reduced compared to monometallic Pd/TiO_2. Thus, a change of the electronic and geometric structure of the active site of the catalyst compared to the monometallic catalyst were suggested as a reason [204].

5.2.3 HMF oxidation on supported monometallic Pd NPs without base addition

5.2.3.1 Effect of the support

Recently, a high yield of FDCA (≥ 99) was obtained by the oxidation of HMF in base free aqueous solution on an Au/HT catalyst under an ambient oxygen pressure at 90 °C [125]. However, the HMF oxidation was performed without addition of a base to obtain information about the behavior of the Pd NPs based materials in base free solution.

Table 25 summarizes the results which were obtained after a reaction time of 8 h. No conversion of HMF was observed if the bare HT_30 support was used as catalyst (Entry 1, Table 25). This is in accordance with previously reported results [127]. If the Pd/hydrotalcite used as catalysts, the HMF was converted with formation of the desired products of HMFCA, FFCA, and FDCA (Entries 2-5, Table 25). The highest FDCA yield (95 %) with a complete HMF conversion was obtained on Pd/HT_30 (Entry 2). The achieved FDCA yield is almost comparable to that obtained on an Au/HT catalysts (99 %) without base addition [125].

After thermal treatment of the unloaded HT_30 support (at 300 °C in an O_2/Ar flow) prior to the Pd NPs deposition, a decreased FDCA yield (73 %) was observed (Entry 3). The yield of FDCA on the Pd/HT_61 and Pd/HT_70 materials were 66 % (at 96 % of the HMF conversion) and 52 % (at 88 % of the HMF conversion), respectively. In addition, larger yields of HMFCA and FFCA could be detected in addition to FDCA. The hydrotalcite supports differ in their Mg to Al ratio which increases from HT_30 to HT_70 (Table 26).

For a Pd/KF/Al_2O_3, conversions of HMF of 60 % were detected, but with only 3 % FDCA yield in respect to the other desired products e.g. HMFCA and FFCA (Entry 6). In the case of a Pd/Al_2O_3, a lower HMF conversion of 10 % was obtained (Entry, Table 25). Al_2O_3 is classified as an amphoteric support and the basic properties of the KF/Al_2O_3 appeared because of the presence of KF in the catalysts. This might be a reason for achieving a higher HMF conversion on Pd/KF/Al_2O_3 than on Pd/Al_2O_3 [205]. The HMF conversion of 26 % was obtained on Pd/ZrO_2/La_2O_3 (Entry 8, Table 25). It was reported that La_2O_3 has basic properties but it is available in this catalysts only with 7 wt % with the respect to neutral properties of ZrO_2 [206].

Table 25. Catalytic results of HMF oxidation (X-HMF conversion, Y-product yield) on different Pd NPs/support catalysts without addition of homogeneous base.

Entry	Catalyst	X(HMF) %	Y(FFCA) %	Y(HMFCA) %	Y(FDCA) %	Balance
1	HT_30	0	0	0	0	
2	Pd/HT_30	>99	0	2	95	0.97
3	Pd/Cal.HT_30	98	3	3	73	0.80
4	Pd/HT_61	96	19	4	66	0.92
5	Pd/HT_70	88	25	10	52	0.98
6	Pd/KF/Al_2O_3	60	15	30	3	0.80
7	Pd/Al_2O_3	10	3	2	3	0.80
8	Pd/ZrO_2/La_2O_3	26	6	4	1	0.42

Reaction conditions: HMF (0.4 mmol), H_2O (20 mL), HMF: Pd= 100 (mol/mol), O_2 flow rate: 35 mL/ min, 90 °C, and 8 h as the reaction time.

Because the hydrotalcite supported pre-formed Pd NPs showed the best catalytic performances, the temporal evaluation of the reaction mixture on these materials was studied in detail. Figure 38 shows plots of HMF conversion and product yields versus reaction time for the Pd NPs/hydrotalcite catalysts. As mentioned before, the hydrotalcite supports differ in their Mg to Al ratio which will be shown later in Table 26. The increase in the molar ratio of Mg:Al is shown in this order: Pd NPs/HT_71 > Pd NPs/HT_61 > Pd NPs/HT_30. On the Pd NPs/HT_30, HMF was completely converted after about 4 h. The HMF oxidation on the Pd NPs/HT_61 and the Pd NPs/HT_70 was clearly slower and incomplete even within 8 h; however, it is assumed that it will be completed if the reaction time is extended to longer than 8 h. The yield of the intermediate HMFCA on all three catalysts is low (about 10 %) which is clearly different compared to other supported catalysts (Figure 28). The time in which the maximum HMFCA yield was obtained shifted from 0.75 h on Pd NPs/HT_30 to about 3 h on Pd NPs/HT_70. Larger differences between the three catalysts were found in the temporal evaluation of the FFCA and the FDCA yield. For the most active catalyst of Pd NPs/HT_30, the yield of FFCA showed a maximum within 1.3 h (30 %). On the contrary, the maximum value of FFCA yield on the Pd NPs/HT_61 and Pd NPs/HT_70 was obtained clearly at longer reaction time of 3 h. The formation of FDCA was also much faster on Pd NPs/HT_30 than on the other materials. Generally, differences in the HMF conversion and product yield between the Pd NPs/HT_61 and the Pd NPs/HT_70 are low in comparison to Pd NPs/HT_30 catalyst. Both of them have a higher number of Mg atoms than the number of Al atoms. Table 26 shows that the molar ratio of Mg:Al after deposition of the Pd NPs in ethanol and after oxidation reaction of HMF in water was changed to be lower

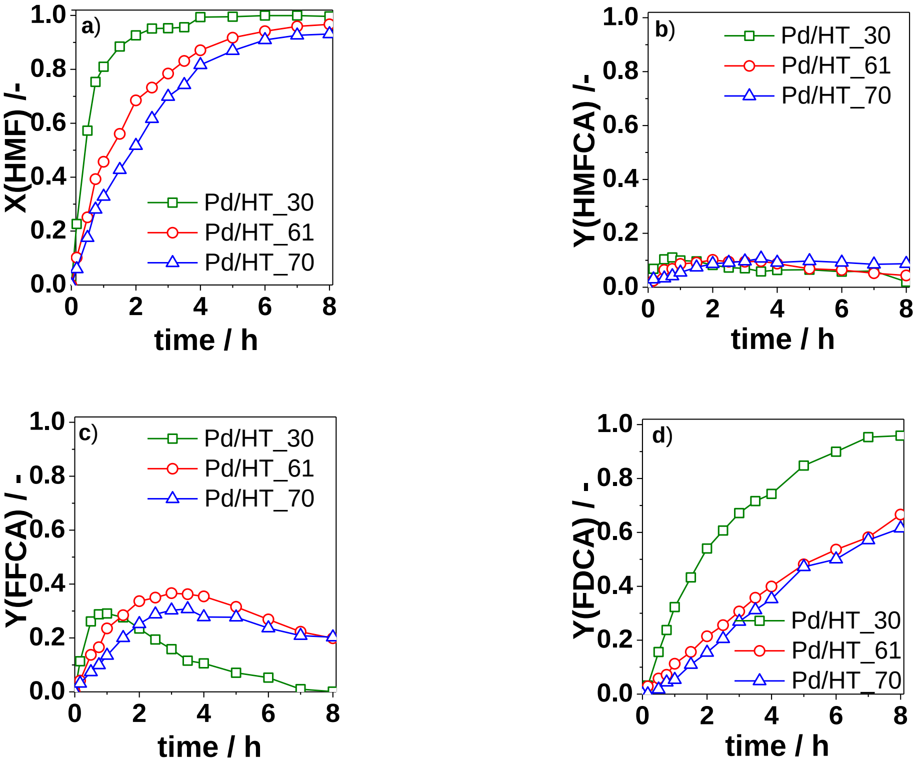

Figure 38. Plot of HMF conversion a) and products formation of HMF oxidation (b-d) versus time for Pd-NPs/hydrotalcite catalysts. Reaction conditions: HMF (0.4 mmol), H_2O (20 mL), HMF:Pd = 100 (mol/mol), 35 mL/min O_2 flow rate, 90 °C, 8 h as the reaction time.

- **Catalyst stability and reusability**

Reusability studies without addition of homogenous were performed for Pd/HT_30, Pd/Cal.HT_30, and Pd/HT_70. The catalysts were recovered using the same produces which was used with others catalyst (Section 5.2.2.1).

The catalytic results are displayed in Figure 39. For all three materials, HMF conversion and FDCA yield decreased strongly with increasing number of runs while the yield of the intermediates HMFCA and FFCA increased. The formation of undesired side products under these conditions was generally low.

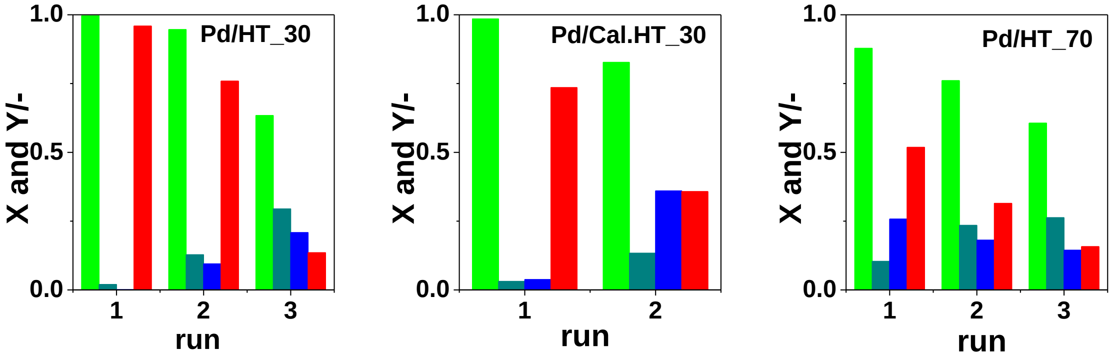

Figure 39. Reusability study using Pd/HT catalysts without base addition; a)- Pd/HT_30, b)- Pd/Cal.HT_30 and c)- Pd/HT_70. Reaction conditions: HMF (0.4 mmol), H_2O (20 mL), HMF:Pd = 100 (mol/mol), 35 mL/min O_2, 90 °C, 8 h as the reaction time, 🟩 X(HMF), ■ Y(HMFCA), 🟦 Y(FFCA) and 🟥 Y(FDCA).

The basic properties of the hydrotalcite are considered as a key factor for the formation of high performance materials which can be tuned via changing the molar ratio of M^{2+} to M^{3+}[207]. With increasing the amount of Mg, the total number of basic sites increases [208, 209].

One can assume that the formation of FDCA not only depends on basicity of the support but also on other parameters because the material with the highest number of basic sites (Pd/HT_70) gave the lowest catalytic performance. The particle size of Pd NPs deposited on the hydrotalcites is almost identical (Table 15). This result suggests that differences in the Pd NPs structure will not be the main reason for differences in catalytic performance between the different Pd/hydrotalcites. Moreover, the Pd content in the post reaction mixture, determined by AAS, is one order lower than the Pd amount measured at presence of homogenous base what indicates marginal Pd leaching (Table 26). However, the Mg/Al ratio of the support is believed to have an impact (Table 26). The hydrotalcite support loses Mg already during the Pd NPs deposition. This process continues if the material will be utilized in HMF oxidation, e.g. the HT_30 has lost the Mg almost completely after the third run. The loss of Mg is furthermore confirmed by the pH value of the post reaction mixture which was clearly higher than could be expected from an aqueous FDCA solution (Table 26). This implies that the results strongly depend on the amount of Mg which is leached into the reaction mixture. Mg leaching is also considered as a reason for a low catalytic stability of the materials.

Table 26. Results of elemental analysis of Pd NPs/hydrotalcite catalysts and of the post reaction mixture.

Entry	Catalyst	Pd [wt %]	Mg:Al [mol/mol]	Mg:Al [mol/mol]	pH[c]	Pd[c] [mg/mL]
1	Pd/HT_30	0.52	0.56	0.34[a]		
	first use	n.d.*	n.d.*	-	7.2	4.2×10^{-5}
	second use	0.54	n.d.*	0.11[b]	7.2	n.d.*
	third use	0.70	n.d.*	0.02[b]	6.7	n.d.*
2	Pd/HT_61	0.28	2.45	1.96[a]		
	first use	n.d.*	n.d.*	1.28[b]	6.9	8.7×10^{-5}
3	Pd/HT_70	0.38	2.7	3.20[a]		
	first use	n.d.*	n.d.*	2.23[b]	6.8	6.3×10^{-5}
	third use	0.47	n.d.*	1.5[b]	n.d.*	n.d.*

[a] after Pd NP deposition, [b] after HMF oxidation, [c] post reaction mixture, *not determined.

The assumption of alterations in the support structure is further supported by XRD studies. X-ray powder pattern of Pd/HT samples are shown in Figure 40.

The unloaded hydrotalcites show only diffraction pattern of a hydrotalcite phase (PDF- Nr. 51-1525). Using the Scherrer formula, the mean crystallite size determined from the most intensive peak at 10° amounted to (10 nm for HT_30), (38 nm for HT_61), and (40 nm for HT_70). The structure of the HT_30 support already started to change during NPs deposition. Besides the peak already mentioned, new peaks appeared which display the formation of an AlOOH phase (PDF –Nr. 49-0133). The peak intensity of the AlOOH phase increases when the sample is utilized in HMF oxidation while that of the hydrotalcite phase decreases. After the third use the hydrotalcite phase has completely disappeared. However, beside peaks from the AlOOH phase new XRD peaks are visible which can be attributed to the formation of an aluminum hydroxide phase (PDF-Nr. 77-0114).

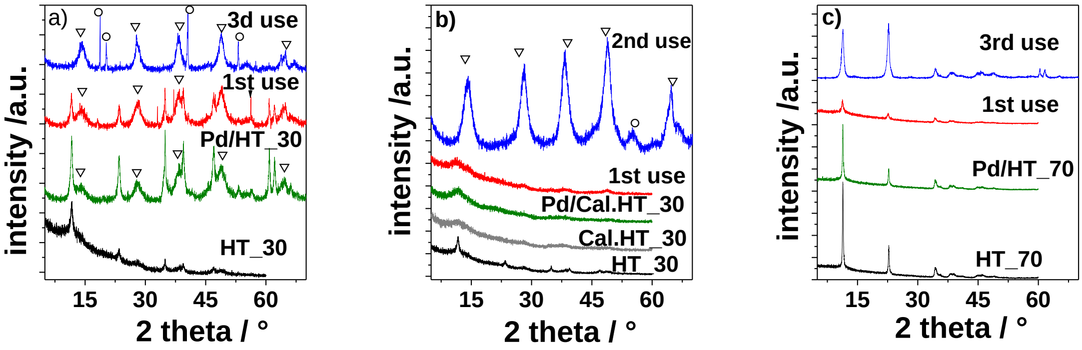

Figure 40. Influence of Pd NPs deposition and HMF oxidation on the XRD pattern of a)- Pd/HT_30, b)- Pd/Cal. HT_30 and c)- Pd/HT_70 (∇ - AlOOH, ○ - $Al(OH)_3$).

If the HT_30 support is calcined at 300 °C, the peaks from the hydrotalcite structure is clearly broader which indicate an amopherization during calcinations (Figure 40b). The shape of the powder pattern after its first utilization in HMF oxidation is almost identical to the pattern of the material after calcinations. However, after its second use, only peaks of an AlOOH phase were detected which was already observed for the Pd/HT_30. For Pd/HT_70 the alterations are lower. But even here, a clear broadening of the line can be observed after third use which could be again interpreted as an indication of a beginning structural change.

In conclusion, the HMF oxidation could proceed on Pd based materials in base free solution. However, enhanced reaction rates were observed when supports with basic properties were used. But, the stability of the basic support limits the recyclability of the catalyst.

5.2.4 Catalytic oxidation of glycerol to lactic acid

5.2.4.1 Effect of bimetallic catalysts on the glycerol oxidation

It has been shown that the modification of the surface of palladium NPs with an additional of metal e.g. Ag or Cu led to a decrease of side product formation and prevents the monometallic Pd catalyst from a fast deactivation during the HMF oxidation reaction [115]. Therefore, the titania supported bimetallic Pd-Ag NPs and Pd-Cu NPs were applied in the selective oxidation of glycerol (GLY).

Initially, a glycerol oxidation was carried out in the absence of catalyst using 5 mmol of aq. GLY solution in a 2:1 molar ratio of NaOH:GLY at 60 °C. Under these conditions only a very low GLY conversion was evident (Entry 1, Table 27). In the presence of homogenous catalyst precursors, a slightly higher, yet low GLY conversion has been observed (Entries 2-4, Table 26). However, a molar ratio of GLY:metal (500:1) was necessary to promote the reaction. These results indicated that homogenous Pd^{2+}, Ag^{+} or Cu^{2+} catalyst are not suitable for efficient GLY oxidation. In presence of mono- and bimetallic palladium-nanoparticles on solid TiO_2 support (Pd/TiO_2 or $Pd\text{-}M/TiO_2$), the GLY conversion was clearly superior. The GLY conversion was about 42 % on monometallic Pd/TiO_2 (Entry 5, Table 27). In the case of bimetallic $Pd\text{-}M/TiO_2$ catalysts (M = Ag or Cu), the glycerol conversion was clearly improved. The best result was achieved using the $Pd\text{-}Ag/TiO_2$ catalyst (Pd:Ag = 4:1 mol/mol) (Entries 6-9, Table 27). The bimetallic $Pd\text{-}Cu/TiO_2$ catalysts showed clearly a lower lactic acid (LA) selectivity and an inferior carbon mass balance compared to monometallic Pd/TiO_2 and bimetallic $Pd\text{-}Ag/TiO_2$ (Entries 8-9, Table 27). The obtained results could be explained based on the results from XPS analysis (Section 5.1.4) with the respect to the active second metal. XPS analysis showed that the oxidation state of the Pd is different in these catalysts. A bivalent Pd species was present in Pd-Cu catalyst while Pd-Ag mostly consisted of a metallic Pd. In the case of monometallic catalyst, Pd/TiO_2 showed both metallic and bivalent Pd species. Besides LA, the other main product of glycerol oxidation on both monometallic Pd/TiO_2 catalyst and bimetallic $Pd\text{-}M/TiO_2$ catalyst was glyceric acid (GLYA) occurring in a range between 17 and 27 %. Other products [glycolic (GOA), tartonic (TA), and oxalic acid (OXA)] were detected in minor amounts < 6 %.

The molar carbon mass balance varied between 0.63 and 0.83 in the experiments performed in presence of mono- or bimetallic catalysts. A relatively low molar carbon mass balance in a GLY oxidation was previously observed. Different reasons were considered: a)-polymerization of reaction products to polymers which are undetectable by HPLC analytical method, b)- adsorption of reaction products onto the support, and c) the sequential oxidation of the C-3 and C-2 products to CO_2 and formic acid [210].

Table 27. GLY oxidation over titania supported bimetallic nanoparticles.

Entry	Catalyst	[1]Pd:M mol/mol	X %	S %					
			GLY	GLYA	LA	GOA	TA	OXA	Balance
1	blank	-	2	3	85	7	n.d.*	n.d.*	0.95
2	[2]Na_2PdCl_4	-	6	3	10	18	n.d.*	17	0.48
3	[2]$AgNO_3$	-	24	2	4	23	n.d.*	6	0.35
4	$CuCl_2$	-	11	12	-	28	n.d.*	5	0.45
5	Pd/TiO_2	-	42	28	45	3	n.d.*	n.d.*	0.76
6	$Pd\text{-}Cu/TiO_2$	10:1	76	24	32	2	5	1	0.64
7	$Pd\text{-}Cu/TiO_2$	4:1	78	26	29	3	3	2	0.63
8	$Pd\text{-}Ag/TiO_2$	10:1	78	20	51	2	4	1	0.78
9	$Pd\text{-}Ag/TiO_2$	4:1	88	18	56	2	6	1	0.83

Reaction conditions: (5 mmol, 0.5 M) glycerol, GLY:Pd=5000 (mol/mol), [2]GLY:Pd=500 (mol/mol), NaOH:GLY= 2:1 (mol/mol), 800 rpm, 5 h, 60 °C, 10 mL total volume of the reaction solution. *not detected, [1] nominal ratio.

5.2.4.2 Effect of silver content on the GLY oxidation

The results showed that the bimetallic Pd-Ag catalyst is more active and selective catalyst compared to monometallic Pd or Pd-Cu catalyst. Furthermore, the LA selectivity increased when silver content increased in the catalyst. Therefore, the Pd-Ag catalyst with a high amount of Ag (Pd:Ag =2:1 mol/mol) was prepared and compared with the other monometallic Pd and bimetallic Pd-Ag catalysts in GLY oxidation.

The initial activity of mono and bimetallic catalyst after 30 min was calculated according to the following formula [(mol GLY consumed per nominal mol metal (Pd+Ag) per hour)]. The initial activity of monometallic Pd/TiO_2 catalyst of 2294 (Entry 1, Table 28) was clearly higher compared to the bimetallic $Pd\text{-}Ag/TiO_2$ catalysts. Regarding the bimetallic catalyst, the initial activity was decreased as the silver content in the catalysts increased (Entries 2-4, Table 28). It was reported that Ag is less active than Pd in the oxidation of benzyl alcohol [81] and glycerol [80]. Concerning the LA selectivity, the bimetallic Pd-Ag catalysts with a nominal ratio of (10:1 or 4:1 mol/mol) showed a higher LA selectivity compared to the monometallic Pd NPs based material (Entries 2-3). However, a further increase of the Ag content in the catalyst (Pd:Ag=2:1) led to a drop in LA selectivity below 52 % (Entry 4). The other main product of glycerol oxidation on both Pd/TiO_2 and Pd-Ag/TiO_2 was GLYA which was formed in between 8 and 15 %. Other products [glycolic (GOA), tartonic (TA), oxalic (OXA), formic (FA), and acetic acid (AA)] were detected with a very low selectivity.

Previous studies reported that a Pd/C catalyst efficiently promotes the oxidation of GLY to GLYA in alkaline solution with selectivity >60 % [24, 26]. Additionally, dihydroxyacetone (DHA) was found to be the main product by oxidation of GLY on an alloyed bimetallic Pd-Ag/C catalyst (molar Ag:Pd ratio 1:1) in the absence of base [80]. Thus, this indicates that product selectivity is not only influenced by the active metal but also depends on other reaction parameters.

Table 28. Glycerol oxidation on titanium oxide supported Pd and Pd-Ag catalysts.

Entry	Catalyst	Initial activity	X[%]	S [%]							
			GLY	GLYA	LA	GOA	TA	OXA	FA	AA	Balance
1	^{1}Pd	2294	96	9	67	1.4	3	n.d	n.d	n.d	0.80
2	^{1}Pd-Ag (10:1)	1180	97	7	78	1.5	3	1	2	2	0.94
3	^{1}Pd-Ag (4:1)	963	98	9	77	2	5	2	<1	1	0.97
4	^{1}Pd-Ag (2:1)	463	98	14	51	1	5.6	1	2	1	0.75

Reaction conditions: (5 mmol, 0.5 M) GLY, GLY:Pd=5000 (mol/mol), NaOH:GLY= 2:1 (mol/mol), 800 rpm, 5 h, 100 °C, 10 mL total volume of the reaction solution.*not detected, $^1TiO_2$ as support.

- **Reusability of the supported catalyst in the GLY oxidation**

In order to obtain information about the catalytic stability of the Pd and Pd-Ag based materials, the Pd/TiO_2, Pd-Ag (10:1)/TiO_2, Pd-Ag (4:1)/TiO_2, and Pd-Ag (2:1)/TiO_2 catalysts were reused under the applied reaction conditions of 5 bar oxygen pressure, 2:1 molar ratio of NaOH to GLY at 100 °C. Concerning this matter, the catalysts were recovered following the same produce which was previously used for other catalysts in the HMF oxidation (Section 5.2.2.1). GLY conversion and product selectivity are presented in Figure 41.

For Pd/TiO_2 catalyst, a dramatic decrease in the glycerol conversion and lactic acid selectivity from 66 % at 97 % glycerol conversion in first run to 17 % at 47 % glycerol conversion in third run has been observed. At the same time, an increased formation of glyceric acid (GLYA) from 9 % to 30 % was detected. Similar behavior was observed in the case of bimetallic Pd-Ag catalyst with 10:1 molar ratio of Pd to Ag. The LA selectivity was likewise decreased from 77 % at 98 % GLY conversion in first run to 57 % at 62.9 % GLY conversion in third run in conjunction with an increased amount of GLYA (8 % to 32 %).

Surprisingly, as the silver content increased in the catalyst, the bimetallic catalyst became more stable and recyclable under the same reaction conditions. It was observed a slight decrease of GLY conversion with a constant LA selectivity of 77 % on Pd-Ag (4:1)/TiO_2 and 50 % for Pd-Ag (2:1)/TiO_2, respectively, over three runs. The observed slight decrease of the GLY conversion might be attributed to the loss of the materials during the washing steps. This was detected by the weighting of the catalyst before and after the washing. Within the limits of sensitivity of ICP, no Pd or Ag species had leached into solution in the case of bimetallic Pd-Ag catalysts. Noteworthy, about 0.1 wt % Pd species was detected in the solution where monometallic Pd catalyst was used.

It is know that the Pt-group (e.g. Pt and Pd) suffers from a fast deactivated by oxygen [98]. However, the presented findings could be attributed to that an increasing in the silver content in the catalyst led to prevent the poisoning of Pd site by oxygen (irreversible deactivation). This results the possibility of reusing the catalyst. Previously, it was reported that a bimetallic Au-Pt/TiO_2 catalyst was more stable compared to monometallic counterparts [32]. It was stated that the interaction of Au with Pt avoided the agglomeration of Au particles and the poisoning of Pt site by oxygen as well.

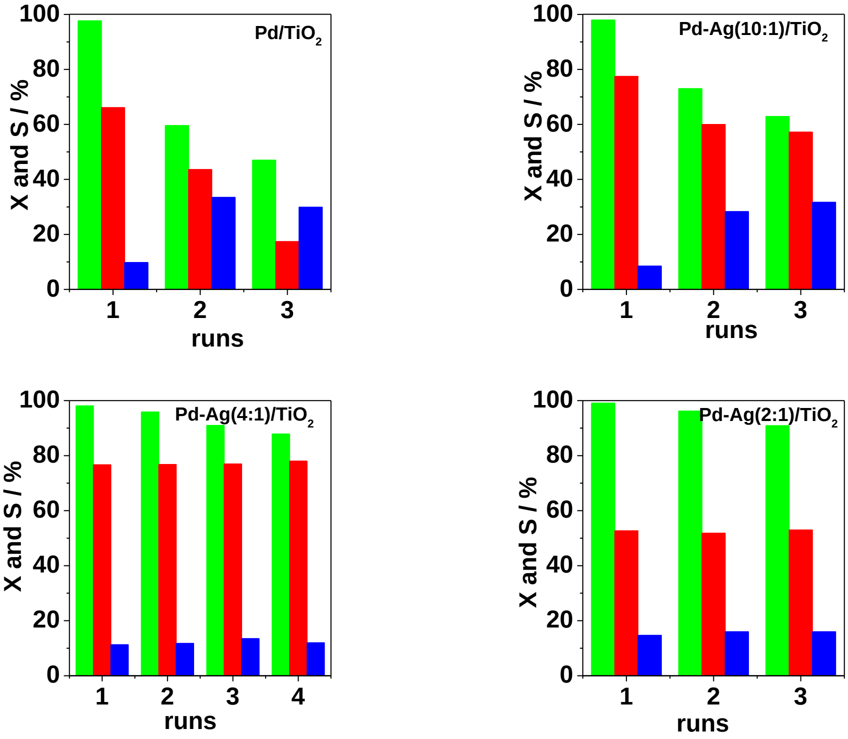

Figure 41. Recycling of the catalysts in GLY oxidation. Reaction conditions: GLY (5 mmol, 0.5M), V_{total}=10 mL, GLY:Pd = 5000:1 (mol/mol), NaOH:GLY = 2:1(mol/mol), 5 h, and at 100 °C, 🟩 X% (GLY), 🟦 S% (GLYA), 🟥 S% (LA).

The recycled Pd-Ag (4:1)/TiO_2 catalyst was characterized by STEM-HAADF and compared with the fresh catalyst (Figure 42). The histogram of particle size distribution derived from STEM images showed that the mean size and width of size distribution of Pd-Ag NPs on TiO_2 increased after utilization of the catalyst in GLY oxidation from 1.8 in fresh catalyst to 4.0 nm after the first run. In both cases the NPs have approximately a spherical shape.

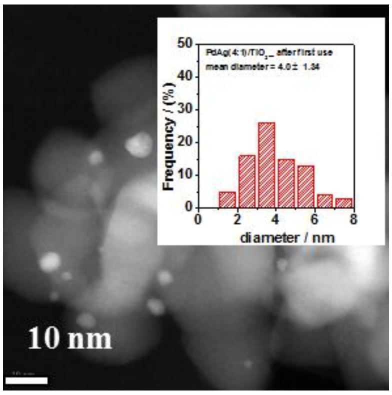

Figure 42. STEM-HAADF images and particle size distributions of Pd-Ag (4:1)/TiO_2 (82 particles) used in GLY oxidation.

In order to obtain information about the electronic structure of the Pd and Ag in the catalysts, the Pd-Ag/TiO_2 catalysts were characterized by XPS after using them in a GLY oxidation. Figure 43 a represents XPS spectrum of Pd3d electrons for the Pd-Ag/TiO_2 (Pd:Ag= 10:1 and 4:1 mol/mol).catalysts. Here, Only Pd in metallic state ($3d_{5/2}$ = 335.4 eV, $5d_{3/2}$ = 340.6 eV) was observed and all bivalent Pd species was reduced during glycerol oxidation. As mentioned before, the binding energy of oxidic and metallic Ag is very close to each other and hence it is not possible to distinguish between one or the other species by XPS [193]. Thus, no clear information could be obtained from Figure 43b.

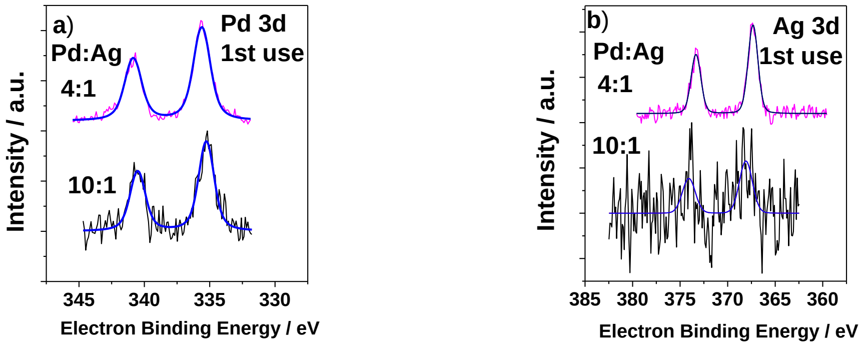

Figure 43. XPS spectra of a)- Pd 3d and b)-Ag 3d of the used Pd-Ag/TiO_2 catalysts.

The amount of the polyvinylpyrrolidone (PVP) stabilizer on the surface of the catalyst was clearly decreased on Pd-Ag evident by a decreased N to metal ratio (Table 29). This might be due to PVP degradation or desorption as already observed during HMF oxidation (Section 5.2.2.1). Degradation of PVP might also serve as explanation for comparable catalytic behavior in the reusability experiments, despite the increasing in the particle size of Pd NPs. Surface sites previously blocked by PVP might become accessible during these processes as already shown in a HMF oxidation (Section 5.2.2.1).

Table 29. Composition of the near-surface region of the fresh and used catalysts (by XPS).

Entry	Catalyst		Pd	Ag	N	Ti
1	Pd-Ag (10:1)/TiO_2	fresh	0.0078	0.0017	0.035	1
		used (1x)	0.0066	0.0011	0.022	1
2	Pd-Ag (4:1)/TiO_2	fresh	0.0064	0.00136	0.038	1
		used (1x)	0.0094	0.0032	0.0086	1

5.2.4.3 Influence of the reaction parameters on GLY oxidation

A high lactic acid (LA) selectivity of 77 % was obtained on a Pd-Ag catalyst (Pd:Ag = 4:1 mol/mol) which additionally showed a stable catalytic performance when the catalyst was recycled. Therefore, this catalyst was chosen to study the effect of reaction parameters on a GLY oxidation in comparison with its monometallic Pd counterparts under varying reaction conditions.

- **Effect of the temperature**

The reaction temperature was studied in the range 30-120 °C on monometallic Pd and bimetallic Pd-Ag catalysts (Pd:Ag = 4:1 mol/mol) under the applied reaction conditions of 5 bar as oxygen pressure and in the presence of base (NaOH to GLY= 2:1 mol/mol).

Figure 44 shows the temporal evolution of GLY conversion and products distributions at different temperatures on the Pd/TiO_2 catalyst (Entries a-c). The rate of GLY conversion increased as the temperature increased (Figure 44a). At 30 °C, GLY conversion was lower than 20 % even after prolonged reaction times of 32 h. Previously, it was reported that the activity of Au/C catalyst was higher than that on Pd/C at 30 °C. This was attributed to a fast poisoning of Pd surface by oxygen at low temperature. However, at elevated temperatures up to 60 °C, the Pd/C became more active and the effect of poisoning less pronounced [29]. The LA selectivity increased as the reaction temperature increased up to about 70 % at 120°C. At 30 °C, the selectivity of LA formation decreased with increasing GLY conversion but it seemed to be nearly independent of the GLY conversion at higher temperatures. Regarding the GLYA selectivity, it was detected as the major product at 30 °C in 55 %.

(Figure 44, Entries d-f) shows the temporal evolution of GLY conversion and product distribution at different temperatures on the Pd-Ag/TiO_2 catalyst. The conversion of GLY increased also as the temperature increased. At 30 °C, the GLY conversion was much higher when Pd-Ag/TiO_2 was used as catalyst (77 % GLY conversion in 32 h) compared to monometallic Pd catalysts. This result indicates that the presence of Ag in the Pd catalyst might lead to increased resistance of Pd catalyst from poisoning by oxygen at low temperature. In terms of LA selectivity, it was increased as the temperature increased up to 100 °C and seems to be also independent of GLY conversion.

At higher temperature of 120 °C, the LA selectively maintained constant of 77 % (Figure 44e). Regarding GLYA, at 30 °C also it was detected as a main product with 35 % selectivity and was likewise independent of the GLY conversion (Figure 44f).

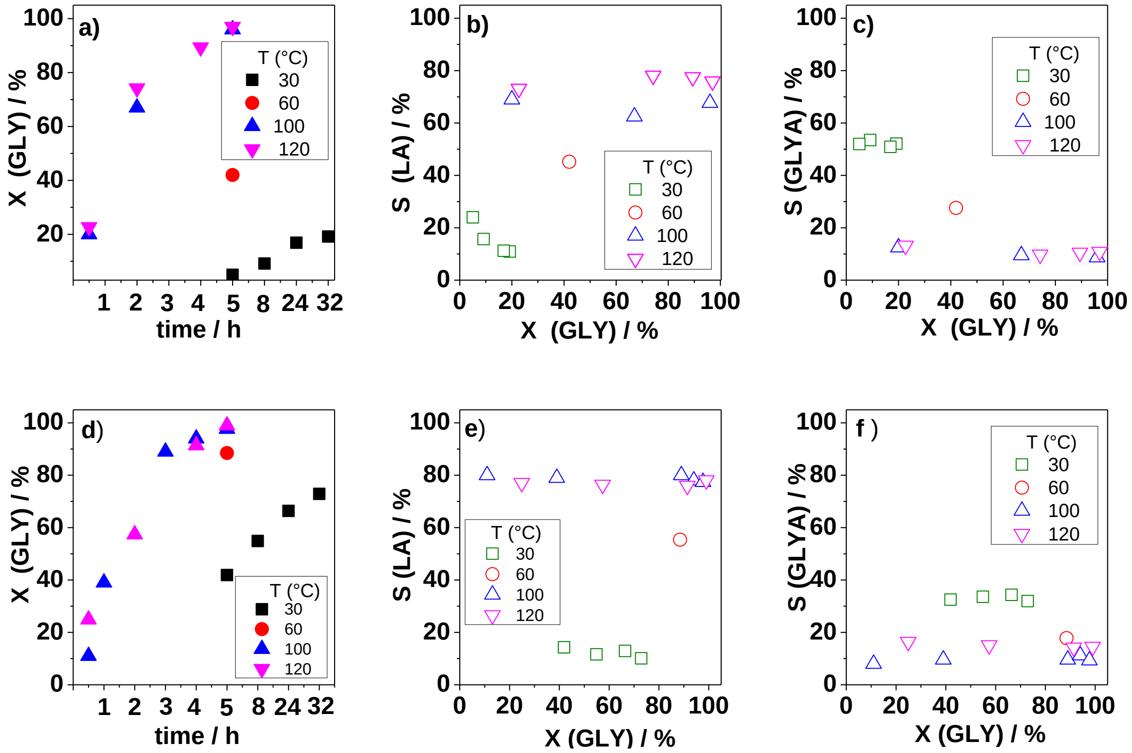

Figure 44. Plots of GLY conversion versus time, LA and GLYA selectivity versus GLY conversion under different temperatures on Pd/TiO$_2$ (a-c) and on PdAg(4:1)/TiO$_2$ (d-f) as catalysts, GLY (5 mmol, 0.5M) V$_{total}$ =10mL, GLY/Pd = 5000:1 (mol/mol), NaOH:GLY= 2:1 (mol/mol), pO$_2$ = 5 bar.

In conclusion, a high temperature of 100 °C is required to produce lactic acid with high yield on Pd or Pd-Ag catalysts. Similarly, it was reported that the temperature has an impact on the LA selectivity in alkaline or acidic solution [33, 35].

- **Effect of the NaOH/GLY ratio**

Previously, it was reported that the nature and concentration of base is crucial in the GLY oxidation [211]. Therefore the influence of base concentration was studied on a Pd-Ag (4:1)/TiO$_2$. In base free solution, no conversion of GLY was detected even after 5h. This result confirmed the necessity of the presence of base to initiate the oxidation of GLY on the heterogeneous metal surface and hence depicts the first step of the alcohol oxidation mechanism., The dehydrogenation of the alcohol group does not occur in absence of base as previously reported [212, 213].

The influence of base on GLY conversion and product selectivity is shown in Figure 45. If a 1:1 molar ratio of NaOH to GLY was used, a GLY conversion of 80 % was obtained after 5 h. The same degree of GLY conversion was achieved for the 2:1 and 4:1 ratios but clearly at a shorter time of 2.5 h. A Low conversion of GLY at low base concentration was previously associated with the consumption of base during the oxidation reaction [155].

The highest LA selectivity (77 %) was obtained for the experiment where a 2:1 molar ratio of NaOH to GLY was used. However, when the reactions were performed with (1:1) or (4:1) molar ratios of NaOH to GLY, selectivity of LA dropped to 69 % and 62 %, respectively. A reason for the lower selectivity of lactic acid formation at low molar ratio of NaOH to GLY was previously suggested by Roy et al. [155]. It was attributed to the complete consumption of base preventing the conversion of pyruvaldehyde to lactic acid. A lower LA selectivity at higher molar ratio of NaOH to GLY might be due to competing oxidation pathway of GLY to glyceric acid on the expense of lactic acid formation (the reaction pathways will be explained vide infra, Section 5.2.4.4). This assumption was drawn from the selectivity of the other oxygenated products e.g. glyceric acid (7 %), tartonic acid (9 %), glycolic acid (4 %), oxalic acid (13 %) and acetic acid (1 %) which were higher compared to those obtained at lower molar ratio of base to GLY.

Based on the reported literatures, a high molar ratio of base to GLY of (4:1) was required to obtain a high selectively of LA on Au/CeO_2, Au-Pt/TiO_2, and Au-Pt/CeO_2 catalysts [32-34].

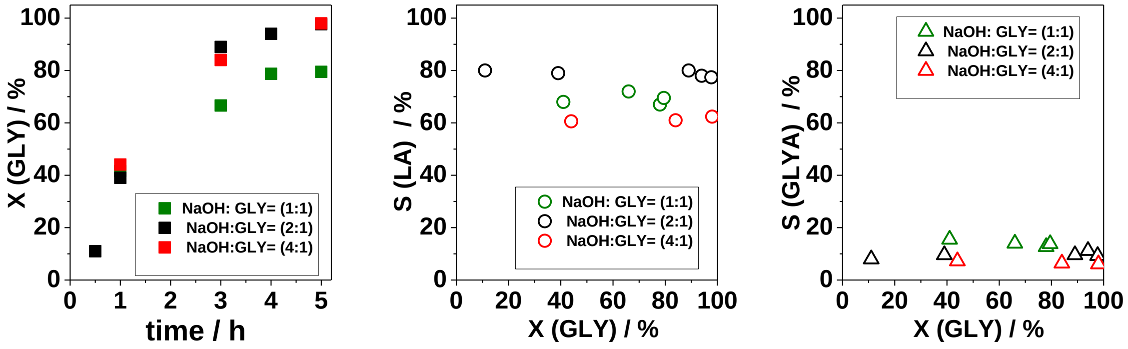

Figure 45. Plots of a) - GLY conversion with time, b) – LA selectivity versus GLY conversion and c) - GLYA selectivity versus GLY conversion for different molar NaOH/GLY ratio, using Pd-Ag (4:1)/TiO_2, GLY (5 mmol, 0.5 M, V_{total}=10 mL, molar ratio GLY/Pd = 5000, pO_2 = 5 bar, at 100 °C.

- **Effect of the O_2 pressure**

The effect of oxygen pressure on a GLY conversion and product selectivity was studied as well. In the case of Pd/TiO_2 catalysts, the GLY conversion and LA selectivity increased as O_2 pressure increased from 1.5 (X (GLY) = 50 %, S (LA) = 40 %) to 5 bar (X(GLY) = 98 %, S(LA)= 65 %) (Figure 46a). When the oxygen pressure was increased up to 10 bar both GLY conversion and LA selectivity dropped dramatically and GLYA was detected as a main product (43 %).

This might be attributed to the deactivation of the Pd catalyst at high oxygen pressure by a (Pd_O_2) adsorption as already suggested in HMF oxidation when a high oxygen flow rate was introduced. A strong decrease of conversion with increasing oxygen pressure was also observed on PVP-Pd NPs in benzyl alcohol oxidation. It was ascribed to formation of a metal oxide surface [22].

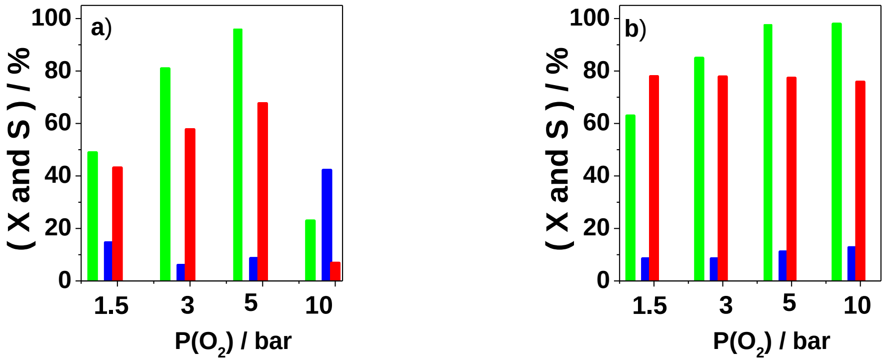

Figure 46. Influence of oxygen pressure on GLY conversion and product selectivity on a)-Pd/TiO_2 and b)-Pd-Ag (4:1)/TiO_2. Reaction conditions: GLY (5 mmol, 0.5M), V_{total}=10 mL, GLY:Pd = 5000:1 (mol/mol), NaOH:GLY = 2:1(mol/mol), and 100 °C). 🟩 X (GLY), 🟦 Y (GLYA), 🟥 Y (LA).

Similarly, the conversion of GLY increased as the oxygen pressure increased from 1.5 up to 5 bar on Pd-Ag (4:1)/TiO_2 and at higher oxygen pressure of 10 bar the catalyst was still intact and no deactivation of the catalyst was observed as already seen on monometallic Pd/TiO_2.(Figure 46b). Regarding the selectivity of LA and GLYA, both of them were almost independent on the oxygen pressure (Figure 46b). Similarly, it was reported that GLY conversion was increased as oxygen pressure was increased from 1 up to 5 bar and LA selectivity was likewise found to be quiet independent on oxygen pressure (74-80 %) using Au-Pt/nCeO_2 as catalyst [33].

Consequently, the presented results indicate that the addition of Ag to Pd NPs prevents the catalyst from deactivation at high oxygen pressure.

5.2.4.4 Proposed reaction pathway of the selective GLY oxidation

It was reported that the pathway of glycerol (GLY) oxidation to glyceric acid (GLYA) and lactic acid (LA) are different on Au-Pt/TiO_2 and Au/CeO_2 catalysts [32, 34].

In order to gain insight whether the over-oxidation and C-C bond cleavage products, which were detected during the performed catalytic experiments on Pd and Pd-Ag, are produced from glyceric acid or lactic acid pathway, additional experiments were conducted, using aqueous lactic acid (LA) (0.4 mmol, 9 mL) in the presence of Pd-Ag/TiO_2 (4:1) as catalyst under 5 bar oxygen pressure at 100 °C. The results showed that the amount of lactic acid remained constant within 5 h (reaction time). This observation led us to the conclusion that the other degradation products ought to stem from the glyceric acid rather from the lactic acid pathway. Previously, it was reported that (5 %) of lactic acid was converted to oxalic, tartonic, and acetic acid on Au-Pt/CeO_2 using the same oxygen pressure and temperature but at higher amount of catalyst (680:1 mol/mol) and base concentration (NaOH:GLY= 4:1 mol/mol) [33].

An experiment was also performed using DHA as reactant (5 mmol, 9 mL) instead of GLY (5 bar oxygen pressure at 100 °C) in the presence of Pd-Ag/TiO_2 (4:1) catalyst in base-free solution. The results showed that the conversion of DHA was very low (8 %) which indicates that DHA seems to be very stable in base-free solution. When the same experiment was performed with base-addition (NaOH:DHA= 2:1 mol/mol), a complete conversion of DHA to LA (>90 % yield) within 5 h has been detected. The same result was obtained in the basic solution in the absence of the Pd-Ag/TiO_2 catalyst. Thus, these results indicate that conversion of DHA to LA is a homogeneous reaction catalyzed by hydroxyl ion (OH^-) and no negative effect was observed on this conversion if the catalyst was added to the reaction solution.

Recently, it was reported a reaction mechanism for the aerobic oxidation of GLY to DHA in base free aqueous solution on a Pd-Ag/C. This mechanism is proposed to be a dehydrogenation mechanism where the glycerol and the oxygen are activated on the catalyst surface [214]. On this catalyst, the secondary OH group of GLY had much higher reactivity compared to the other OH groups. However, the primary hydroxyl group of GLY is adsorbed on the surface of Ag site. The secondary alcohol group of GLY was attacked by atomic oxygen activated on the Pd site to break the C-H bond and the carbonylic product (DHA) is formed by the separation of O-H bond.

Our results showed that the presence of base is necessary to initiate the oxidation of GLY on Pd-Ag/TiO_2 catalyst (Section 5.2.4.3). However, the DHA will be in equilibrium with its tautomeric from glyceraldehyde (GLYHD) in an alkaline solution [32].

Further catalytic oxidation of this intermediate [GLYHD = DHA] may deliver glyceric acid (GLYA). On contrary, the base-catalyzed dehydration of (GLYHD=DHA) produced the 2-hydroxypropenal and pyruvaldehyde [32]. A 1,2-hydride shift of the keto-enol tautomerization intermediates leads to form lactic acid (LA) (Scheme 9).

A high yield of LA can be obtained only if the rate of dehydration reaction of both intermediates DHA and GLYHD is faster than their oxidation. Other oxygenated products e.g. tartonic acid (TA), glycolic acid (GOA), oxalic acid (OXA), formic acid (FA), and acetic acid (AA) could be formed via glyceric acid pathway since lactic acid proved to be highly stable under the applied reaction conditions.

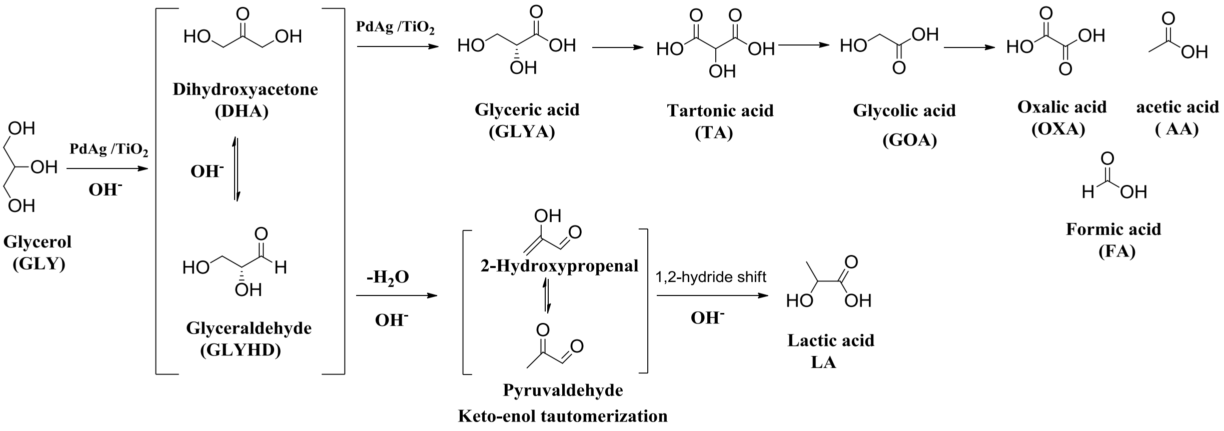

Scheme 9. Proposed reaction pathway of glycerol oxidation.

In conclusion, the results showed the possibility obtaining a relatively high yield of lactic acid by oxidation of glycerol over Pd and Pd-Ag catalysts using a low amount of the catalyst and a low amount of base.

6. Conclusion

Differently sized PVP-stabilized Pd NPs (mean diameter =1.8-4.4 nm) were prepared in ethylene glycol at different molar ratios of NaOH:Pd. When the molar ratio of NaOH:Pd increased (in the NPs synthesis solution), a smaller particle size of NPs was formed.

The synthesized monometallic Pd NPs were applied in HMF oxidation. The highest yield of FDCA (90 %) was obtained with the smallest particle size of Pd NPs (mean diameter =1.8 nm). The oxygen content in the liquid phase has an impact on the catalytic performance of Pd NPs. Therefore, the oxygen flow rate should be adjusted carefully in order to obtain a high yield of FDCA. The Pd NPs were quickly deactivated if the oxygen flow rate was far from the optimum. However, the deactivation might be due to a block of the active surface sites by side products formation, if the oxygen content in liquid phase was too low (oxygen flow rate too low). While the deactivation might be caused by the interaction of the Pd surface with oxygen (Pd_O_2), if the oxygen content in liquid phase was too high (oxygen flow rate too high).

The catalytic performance of the stored Pd NPs in the same synthesis solution at atmospheric conditions was influenced by the pH of NPs synthesis solution. However, the catalytic performances of Pd NPs synthesized and stored in strongly alkaline medium remained unchanged after up to one month. An obvious loss of the catalytic performance was observed when the NPs were synthesized and stored in a neutral or acidic medium.

The heterogeneous supported catalysts were prepared by colloidal deposition of pre-formed Pd nanoparticles onto carrier materials. The prepared catalysts were applied in the aerobic oxidation of HMF in aqueous solution under an atmospheric oxygen pressure at 90 °C with and without addition of homogenous base.

With the addition of a homogeneous base, the yield of FDCA is influenced by the support. The strongest interaction of Pd NPs with the support was observed with TiO_2. This strong interaction might be the reason for the lower changes of the particle size and the shape of NPs during HMF oxidation in the Pd/TiO_2 catalyst. Furthermore, it might be also responsible for fewer amounts of Pd species in the post reaction solution compared to other catalysts e.g. $Pd/ZrO_2/La_2O_3$ or Pd/Al_2O_3. Although Pd/TiO_2 catalyst has a lot of advantages, a lower yield of FDCA was observed. This might be explained by a stronger adsorption of the substrate (HMF) and reaction intermediate (e.g. HMFCA) on the catalyst surface. This could lead to a blocking of active surface sites during the initial stage of the reaction (evident by the lower carbon mass balance).

High yields of FDCA connected with a relatively stable catalytic performance were obtained on Pd/ZrO_2/La_2O_3 catalysts. Generally, two different types of deactivation were observed: i) - a reversible short-term deactivation by a blocking of active surface sites of Pd and ii)-an irreversible long-term deactivation by alterations in Pd structure and by Pd leaching. The change in the particle size and shape of the NPs on the support surface during the HMF oxidation could result from the aggregation of the formerly isolated small NPs. The catalytic performance was not strongly affected by the changes in Pd structures because the surface of the small Pd NPs in the formed aggregates stayed largely intact.

The modification of the surface of Pd nanoparticles by adding a second metal (Ag or Cu) led to an increase in the capability of the catalyst to oxidize the HMFCA completely. Hence, it prevents the catalyst from a fast deactivation during the HMF oxidation which was observed for the monometallic Pd catalysts. Furthermore, the amounts of byproducts were clearly reduced compared to monometallic Pd/$TiO_{2.}$ These observations could be attributed to changes of the electronic and geometric structure of the active site of the bimetallic catalysts compared to the monometallic catalyst.

Without the addition of a homogeneous base, high FDCA yields can only be obtained if hydrotalcites are used as supports. The activity of the Pd/hydrotalcite supports is influenced by the Mg/Al ratio. Beside the basicity of the support, the results of characterization also indicate that the formation of FDCA is closely connected with Mg leaching from the support into the solution, thus making the solution alkaline.

Titania supported Pd and Pd-Ag catalysts are active and selective catalysts in the selective oxidation of GLY to lactic acid (LA). The selectivity of LA is influenced both, by the reaction parameters and by silver content in the catalysts. A high selectivity of LA connected with a relatively stable catalytic performance was obtained on Pd-Ag catalyst which has a nominal molar ratio of Pd to Ag (4:1). The monometallic Pd catalyst was deactivated if the oxygen pressure was too high, the deactivation might be caused by the interaction of the Pd surface with oxygen. Thus, the addition of silver to Pd catalyst led to an increase in the stability of the catalyst at a high oxygen pressure. Furthermore, the amount of metal leaching was reduced when the silver was present in the catalyst.

7. Appendix

7.1 Parameters of the analytical methods

7.1.1 Powder X-ray diffraction

XRD patterns were measured on a Theta/Theta diffractometer (X'Pert Pro from Panalytical, Almelo, Netherlands) with CuKα radiation (λ=0.15418 nm, 40 KV, 40 mA) and a X'Celerator RTMS Detector. The alignment was checked by use of a silicon standard. The data were recorded in a 2 theta range from 5 -70°. The solid prepared material was directly submitted to XRD but in the case of NP in solution the following steps were required to obtain a solid material. Here, 5 mL of the synthesis solution of NPs was washed once with acetone and centrifuged at 5800 rpm until the organic phase was no long colored. Afterwards, the solid residual was dried with air at ambient temperature and then scratched from the tube wall.

7.1.2 Transmission electron microscopy

TEM measurements were made at 200 kV by using a JEM-ARM200F (JEOL) instrument. The microscope was equipped with a JED-2300 (JEOL) energy-dispersive X-ray spectrometry (EDXS) instrument for chemical analysis. TEM images of materials were obtained at 200kV with a JEM-ARM200F (JEOL Ltd). For TEM measurements, the solid materials were submitted directly to TEM but in the case of NP in synthesis solution the following steps were required, here, 100 µl of the colloidal solution of NP was mixed with an excess of acetone and centrifuged. The solid residual was dissolved in methanol and a drop of this mixture was deposited on a holey carbon supported Cu grid (mesh 300). Finally, the grid was dried in vacuum.

7.1.3 Scanning electron microscopy

Scanning electron microscopy (SEM) images of materials were obtained at 200kV with a JEM-ARM200F (JEOL Ltd) which is aberration-corrected by a CESCOR (CEOS). High-angle annular dark field (HAADF) imaging was operated with a spot size of 6c (approximately 0.13 nm) and a 40 µm condenser aperture. The samples were deposed on holey carbon supported Cu-grids (mesh 300) and transferred to the microscope.

7.1.4 Small-angle X-ray scattering

The measurement of SAXS were carried out with a Kratky-type instrument (SAXSess, Anton Paar, Austria) operated at 40 kV and 50 mA in slit collimation using a two-dimensional CCD detector (T = −40 °C). The 2D scattering pattern was converted into a one-dimensional scattering curve as a function of the magnitude of the scattering vector $q = (4\pi/\lambda)\sin\left(\frac{\theta}{2}\right)$ with SAXS Quant Software (Anton Paar). A Göbel mirror was used to convert the divergent polychromatic X-ray beam into a collimated line-shaped beam of Cu Kα radiation (λ = 0.154 nm). Slit collimation of the primary beam was applied in order to increase the flux and to improve the signal quality. Scattering curves were obtained as the average of 120 measurements monitored over 5 seconds. Scattering profiles of the Pd NP were obtained by subtraction of the detector current and the scattering of the solvent from the scattering profiles of the Pd nanoparticles. From the scattering curves the volume-weighted size distribution was obtained by indirect Fourier transformation (IFT) [215] using the program GIFT (implemented in PCG software package, Version 2.02.05, university Graz).

7.1.5 X-ray photoelectron spectroscopy

The measurements were performed with an ESCALAB 220iXL (Thermo Fisher Scientific) with monochromatic Al Kα radiation (E = 1486.6 eV). The samples were fixed on a stainless steel sample holder with double adhesive carbon tape. For charge compensation a flood gun was used, the spectra were referenced to the C1s peak at 284.8 eV. The error range for the determination of the electron binding energy is estimated as ± 0.2 eV. After background subtraction the peaks were fitted with Gaussian-Lorentzian curves to determine the positions and the areas of the peaks. The surface composition was calculated from the peak areas divided by the element- specific Scofield factor and the transmission function of the spectrometer.

7.1.6 UV-Vis spectroscopy

UV-Vis spectra were recorded with Avater Ava light -DH-S-BAL combined with deuterium and halogen light source in the range of 200-700 nm. UV-Vis spectra were recorded with Avatec Ava light -DH-S-BAL combined with deuterium and halogen light source in the range of 200-700 nm. For UV/Vis analysis of the nanoparticles, a 100 µL of the synthesis solution were diluted by 10 mL of ethanol.

7.1.7 Atomic spectroscopy

AAS instrument is a computerized routine atomic absorption and emission-spectrometer for flame AAS, with two-beam optics (Deuterium lamp and hollow Kate lamp), 6-fach lamp changer, burner system for air /acetylene and nitrous oxide/acetylene and security of gas supply. By using an AAS-A Analyst 300 from Perkin Elmer, the samples contains Pd, Au, Mg, and Al were determined to obtain e.g. metal loading, molar ratio of (Pd to Au) or (Mg to Al), leaching of metal into solution. For the NPs in solution, 500 µl of the corresponding synthesis solution were filled in a glass tube. Afterwards, the solution was heated up for 1h until the ethylene glycol was evaporated, where a solid Pd-Au NPs was then dissolved by acid before AAS measurements. For the solid materials, the measurement was done after pulping the solid by sulphuric acid and potassium bisulfate. In order to determine the metal amount in the reaction solution, 10 mL of the post reaction mixture were mixed with 10 mL aqua regia before being analyzed by AAS. ICP was used for materials contain bimetallic catalyst Pd-Ag, the molar ratio of Pd to Ag to determine e.g. the metal loading in the catalyst, and leaching of palladium and silver into the solution

7.1.8 Zeta potential measurements

The zeta potential was measured with a Zeta Sizer 3000 HS (Malvern Instrument) at 25°C. To measure the Zeta potential 5 mg of the ZrO_2/La_2O_3 support were added to 20 mL pH buffer solutions with pH value of 4 (Mettler Toledo), 7 or 10 (Hanna Instruments). Before measurement of the zeta potential, the three suspensions were treated for 15 min in an ultrasonic bath. The following results were obtained (results of two measurements):
pH= 4: 4.7 and 4.1 mV, pH=7: 0.3 and 0.1 mV, and pH=10: - 43.9 and -42.7 mV
Additionally, the Zeta potential of the alumina support at pH=10 was also measured using the same procedure as applied for ZrO_2/La_2O_3.pH=10: -23.6 and -23.9 mV

7.2 Rough calculations of the ratio of the added metal atoms (Ag, Au, or Cu) to the Pd surface atoms

The number of Pd atoms in the solution (N_{atoms}) was calculated by:

$$N_{atoms} = N_A \text{ x } \text{mol (Pd)} \tag{28}$$

N_A = Avogadro’s number, and 10 mL of Pd NPs (20 mM).

The number of second metal atoms (Ag, Au, or Cu) in the solution ($'N_{atoms}$) was calculated by:

$$'N_{atoms} = N_A \text{ x } \text{mol (M)} \tag{29}$$

Herein, 1, 2.5, and 5 mL of 20 mM metal salt containing solution (M= Ag, Au, or Cu) was added to 10 mL Pd NPs containing solution (ethylene glycol, pH=11).

The mean number of Pd atoms in a single particle is approximated according to the following equation, assuming a spherical particle shape [185]:

$$n = \frac{0.5\,\pi\, N_A\, d_m^3}{3V_m} \tag{30}$$

Herein, d_m = the mean diameter (m), V_m = the molar volume of Pd; $V_m = 8.56 \text{x} 10^{-6}$ m^3/mol. The atom number (n) for Pd_1 ($d_m = 4.4 \text{x} 10^{-9}$ m, derived from TEM) = 3134 for Pd_2 ($d_m = 1.9 \text{x} 10^{-9}$ m, derived from TEM) = 252 and for Pd_3 ($d_m = 1.8 \text{x} 10^{-9}$ m, derived from TEM) = 214.

The total number of atoms in a single particle N_1, the number of the atoms per shell N_2 and the percentage of the surface atoms in a single particle are theoretically calculated by equations (31-33).

The total number of atoms in a single particle (N_1) was calculated by [186] :

$$N_1 = 1/3\,(2\,m - 1)(5\,m^2 - 5\,m + 3) \qquad (31)$$

Herein, m = the number of shells.

The number of the atoms per shell (N_2) was calculated by [186]:

$$N_2 = 10\,m^2 - 20\,m + 12 \qquad (32)$$

Then, the surface atom in a single particle was formulated as:

$$R\,(\%) = \frac{N_2}{N_1}\ x\ 100 \qquad (33)$$

Table 30. The surface atoms in a single particle.

Entry	m	N_1	N_2	R %
1	1	1	1	100.0
2	2	13	12	92.3
3	3	55	42	76.4
4	4	147	92	62.6
5	5	309	162	52.4
6	6	561	252	44.9
7	7	923	362	39.2
8	8	1415	492	34.8
9	9	2057	642	31.2
10	10	2869	812	28.3

The number of Pd surface atoms was calculated by:

$$\text{The number of Pd surface atoms} = \frac{N_{atoms}\ x\ R}{100} \qquad (34)$$

Table 19 summarizes the mean atoms number of Pd in a single particle (n), the number of Pd atoms in solution (N_{atoms}), and the number of Pd surface atoms (S_{atoms}) as well.

The ratio of the added metal atoms (Ag, Au, or Cu) to the Pd surface atoms was formulated as:

$$S_M\,(\%) = \frac{'N_{atoms}}{\text{The number of Pd surface atoms}} \text{ x } 100 \tag{35}$$

Table 31. The ratio of the added metal atoms to the Pd surface atoms.

Entry	Pd:M	$'N_{atoms}$	S_M (%)
1	1:10	$1.2\text{x}10^{19}$	16
2	4:1	$3.01\text{x}10^{19}$	40
3	2:1	$6.02\text{x}10^{19}$	80

The number of Pd surface atoms= $7.54\text{X}10^{19}$

7.3 Calibration curves of the components in HMF oxidation

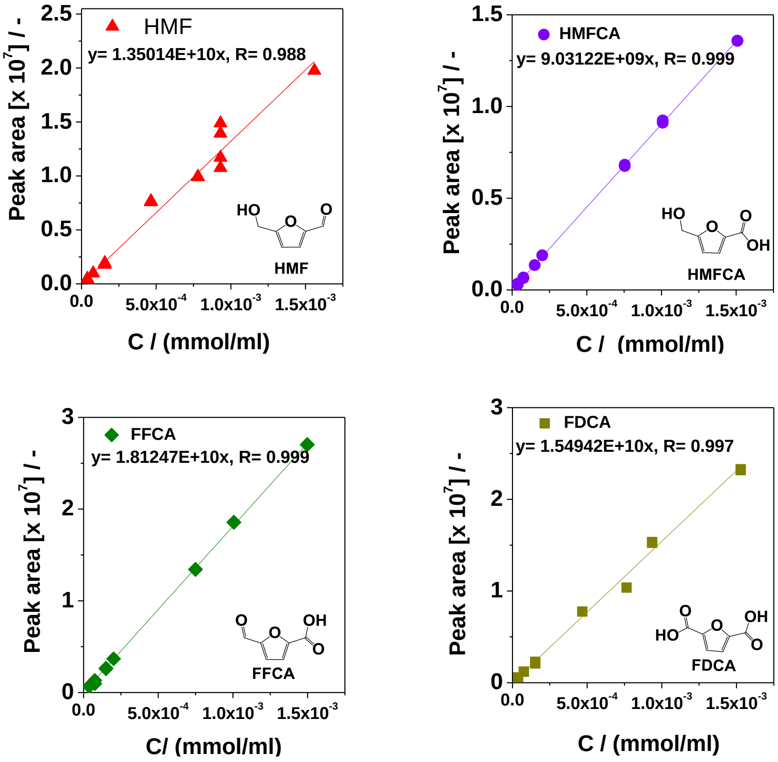

Figure 47. Calibration curves of the components in HMF oxidation.

7.4 Calibration curves of the components in GLY oxidation

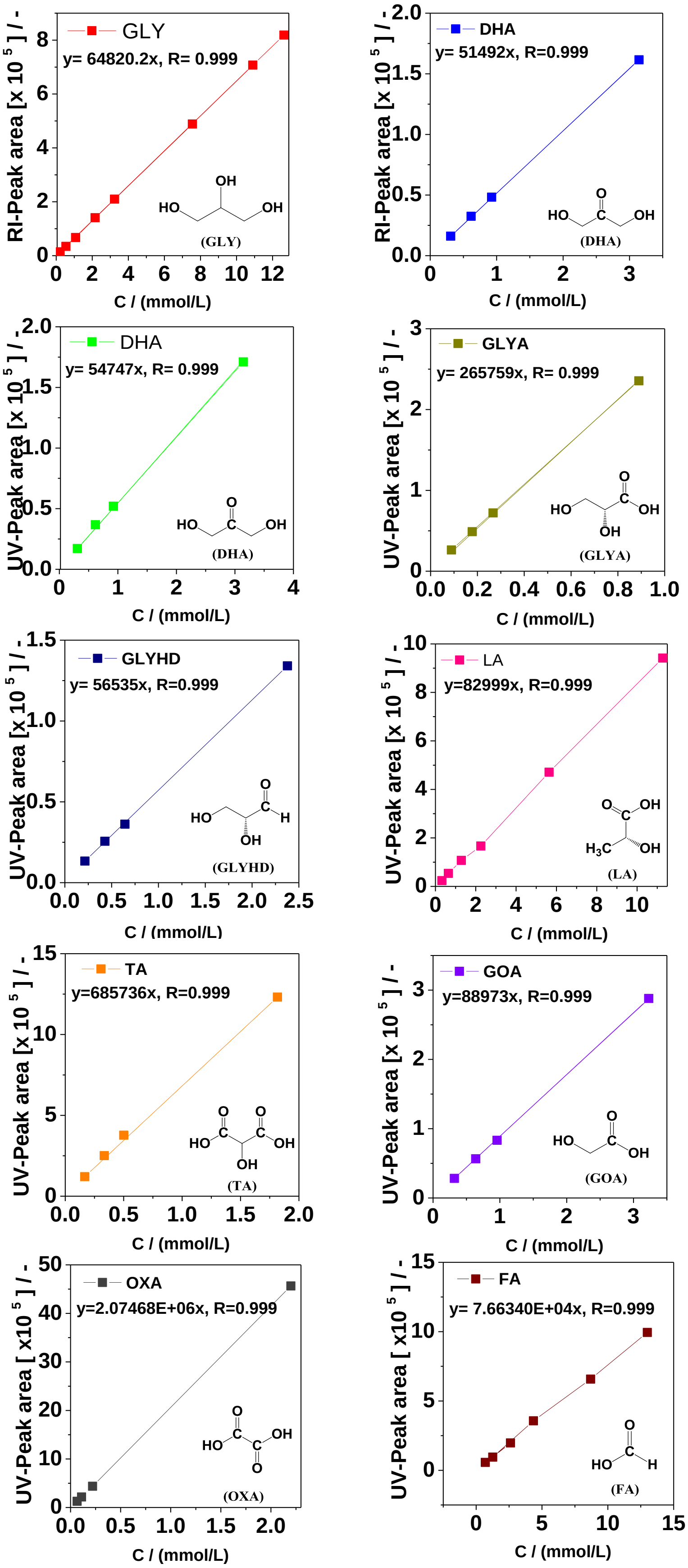

Figure 48. Calibration curves of the components in GLY oxidation.

7.5 Comparison between the 1H-NMR spectrum and UV-HPLC chromatogram in GLY oxidation

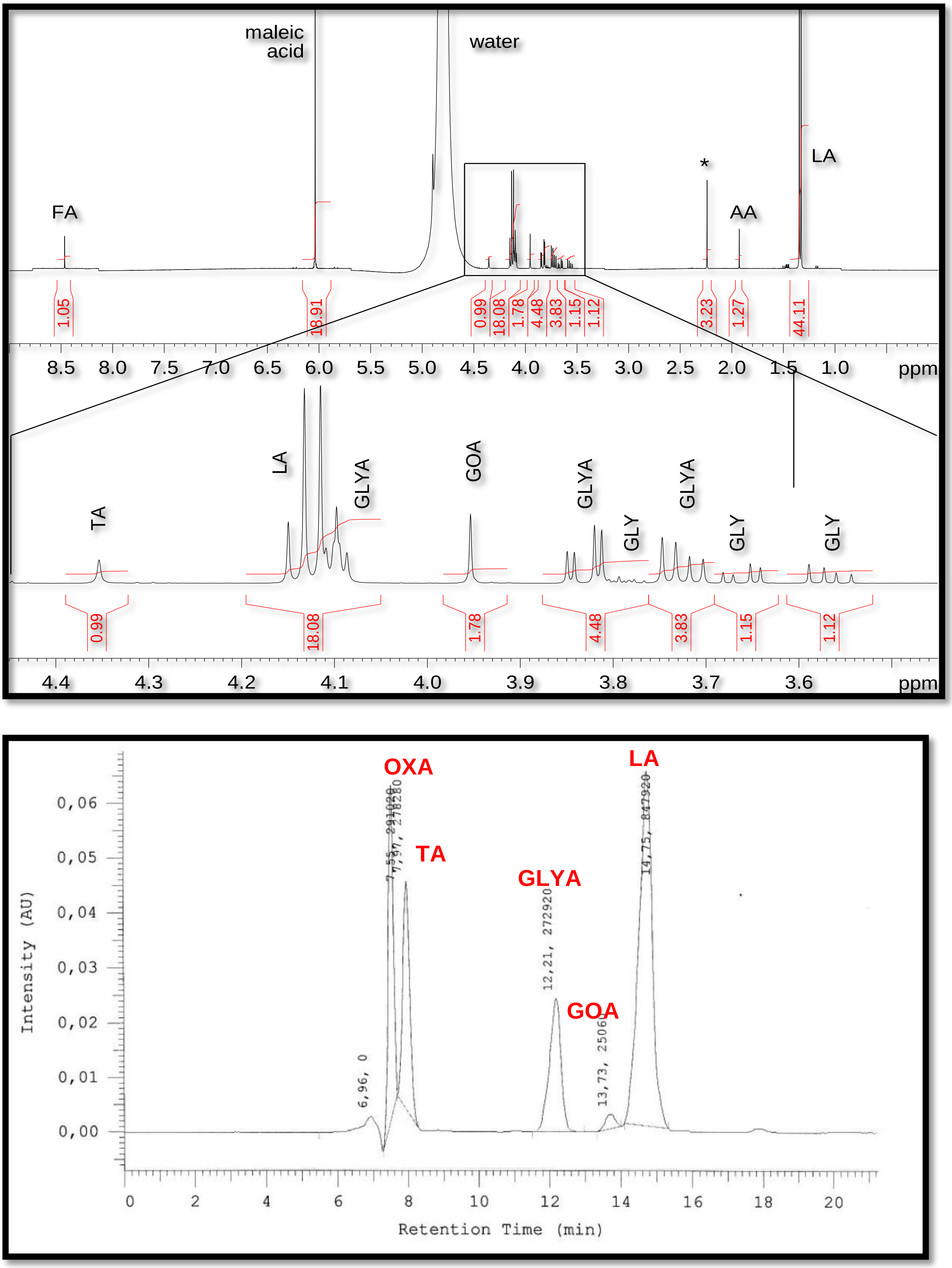

Figure 49. 1H-NMR spectrum and UV-HPLC chromatogram in GLY oxidation at 100 °C, GLY (5 mmol, 0.5 M), V_{total}= 10 mL, GLY:Pd = 5000:1 (mol/mol), NaOH:GLY = 2:1 (mol/mol), pO_2 = 5 bar.

7.6 Reusability of the catalysts in HMF oxidation with addition of homogenous base

A) - using Pd/ZrO_2/La_2O_3.

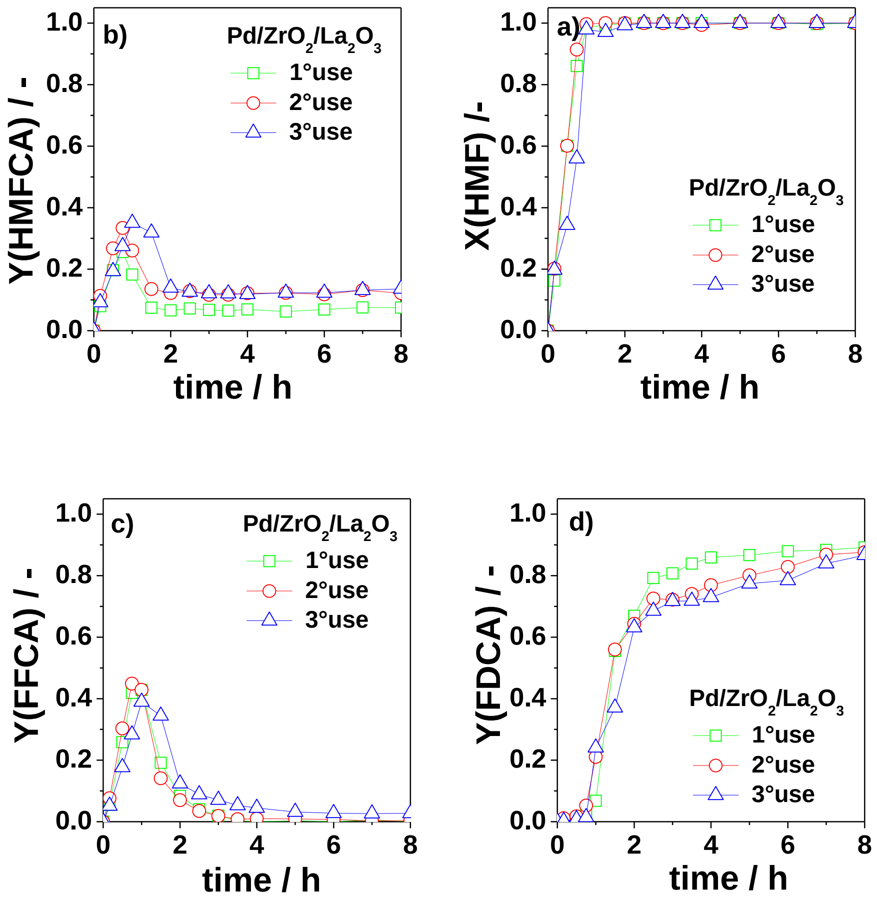

Figure 50. Plots of HMF conversion (a) and product yields (b-c) versus time on Pd/ZrO_2/La_2O_3 catalysts. Reaction conditions: HMF (0.4 mmol), H_2O (20 mL), HMF:Pd = 100 (mol/mol), O_2 flow rate (35 mL/min), 90 °C, (1 mL/h) aq. NaOH addition (0.5 M), 8 h as the reaction time.

B) - using Pd/TiO_2.

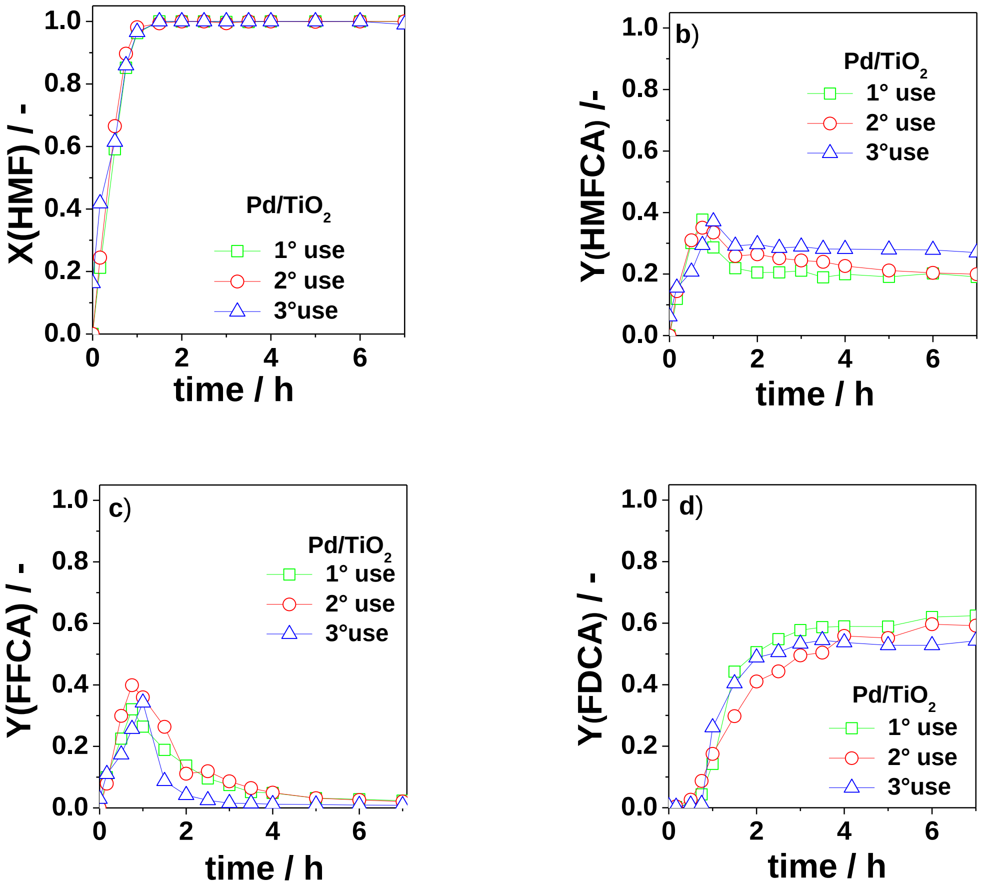

Figure 51. Plots of HMF conversion (a) and product yields versus reaction time on Pd/TiO_2 catalysts. Reaction conditions: HMF (0.4 mmol), H_2O (20 mL), HMF:Pd = 100 (mol/mol), O_2 flow rate (35 mL/min), 90 °C, (1 mL/h) aq. NaOH addition (0.5 M), 8 h as the reaction time.

C) - using Pd/KF/Al_2O_3.

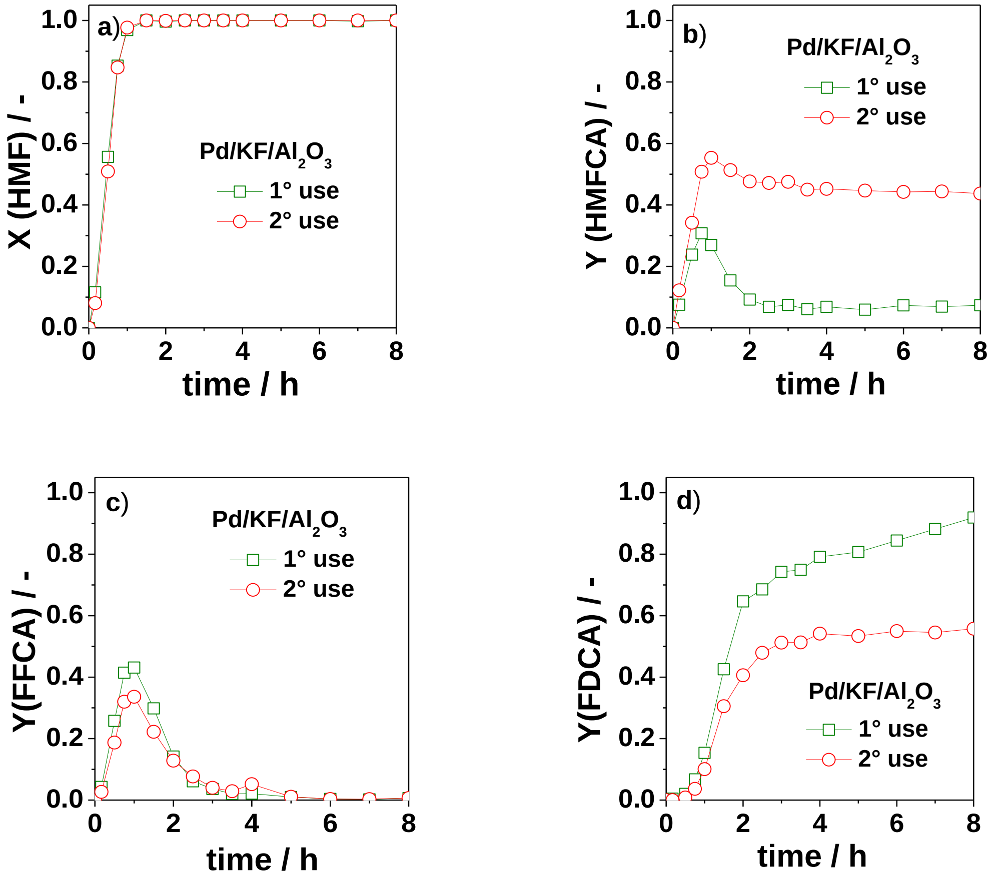

Figure 52. Plots of HMF conversion (a) and product yields (b-d) versus time on Pd/KF/Al_2O_3 catalysts. Reaction conditions: HMF (0.4 mmol), H_2O (20 mL), HMF/Pd = 100 (mol/mol), O_2 flow rate (35 mL/min), 90 °C, (1 mL/h) aq. NaOH addition (0.5 M), 8 h as the reaction time.

8. References

[1] R. A. Van Santen, P. W. N. M. van Leeuwen, J. A. Moulijn, B. A. Averill, Elsevier, Netherlands, **2000**.

[2] J. M. Campelo, D. Luna, R. Luque, J. M. Marinas, A. A. Romero, *ChemSusChem*, **2009**, *2*, 18-45.

[3] F. Pinna, *Catal. Today*, **1998**, *41*, 129-137.

[4] R. Banerjee, P. A. Crozier, *J. Phys. Chem. C*, **2012**, *116*, 11486-11495.

[5] C. J. Jia, F. Schuth, *Phys. Chem. Chem. Phys.*, **2011**, *13*, 2457-2487.

[6] B. Corain, G. Schmid, N. Toshima, Elsevier, Netherland, **2011**.

[7] J. Croy, S. Mostafa, J. Liu, Y. Sohn, H. Heinrich, B. Cuenya, *Catal. Lett.*, **2007**, *119*, 209-216.

[8] J. D. Grunwaldt, C. Kiener, C. Wögerbauer, A. Baiker, *J. Catal.*, **1999**, *181*, 223-232.

[9] C. Moreau, M. N. Belgacem, A. Gandini, *Top. Catal.*, **2004**, *27*, 11-30.

[10] M. Kröger, U. Prüße, K. D. Vorlop, *Top. Catal.*, **2000**, *13*, 237-242.

[11] C. Rasrendra, J. Soetedjo, I. Makertihartha, S. Adisasmito, H. Heeres, *Top. Catal.*, **2012**, *55*, 543-549.

[12] S. G. Wettstein, D. M. Alonso, E. I. Gürbüz, J. A. Dumesic, *Curr. Opin. Chem. Eng.*, **2012**, *1*, 218-224.

[13] T. Werpy, G. Petersen, US Department of Energy report, http://www.osti.gov/bridge/, **2004**.

[14] A. Gandini, M. N. Belgacem, *Prog. Poly. Sci.*, **1997**, *22*, 1203-1379.

[15] S. S. Yazdani, R. Gonzalez, *Curr. Opin. Biotechnol.*, **2007**, *18*, 213-219.

[16] Y. J. Wee, J. N. Kim, H. W. Ryu, *Food Technol. Biotechnol.*, **2006**, *44*, 163-172.

[17] K. Mori, T. Hara, T. Mizugaki, K. Ebitani, K. Kaneda, *J. Am. Chem. Soc.*, **2004**, *126*, 10657-10666.

[18] M. Mifsud, K. V. Parkhomenko, I. W. C. E. Arends, R. A. Sheldon, *Tetrahedron*, **2010**, *66*, 1040-1044.

[19] W. Hou, N. A. Dehm, R. W. Scott, *J. Catal.*, **2008**, *253*, 22-27.

[20] B. Feng, Z. Hou, H. Yang, X. Wang, Y. Hu, H. Li, Y. Qiao, X. Zhao, Q. Huang, *Langmuir*, **2009**, *26*, 2505-2513.

[21] Z. Ma, H. Yang, Y. Qin, Y. Hao, G. Li, *J. Mol. Catal. A: Chem.*, **2010**, *331*, 78-85.

[22] H. Alex, N. Steinfeldt, K. Jähnisch, S. Hübner, M. Bauer, *Nanotechnol. Rev.*, **2014**, *3*, 99-110.

[23] S. E. Davis, L. R. Houk, E. C. Tamargo, A. K. Datye, R. J. Davis, *Catal. Today*, **2011**, *160*, 55-60.

[24] N. Dimitratos, J. Lopez-Sanchez, D. Lennon, F. Porta, L. Prati, A. Villa, *Catal. Lett.*, **2006**, *108*, 147-153.

[25] T. F. Blackburn, J. Schwartz, *J. Chem. Soc., Chem. Commun.*, **1977**, *5*, 157-158.

[26] R. Garcia, M. Besson, P. Gallezot, *Appl. Catal. A: General*, **1995**, *127*, 165-176.

[27] G. Giachi, W. Oberhauser, M. Frediani, E. Passaglia, L. Capozzoli, L. Rosi, *J. Poly. Sci. Part A: Poly. Chem.*, **2013**, *51*, 2518-2526.

[28] H. T. Tan, Y. Chen, C. Zhou, X. Jia, J. Zhu, J. Chen, X. Rui, Q. Yan, Y. Yang, *Appl. Catal. B: Environ.*, **2012**, *119–120*, 166-174.

[29] C. L. Bianchi, P. Canton, N. Dimitratos, F. Porta, L. Prati, *Catal. Today*, **2005**, *102–103*, 203-212.

[30] W. C. Ketchie, M. Murayama, R. J. Davis, *J. Catal.*, **2007**, *250*, 264-273.

[31] G. L. Brett, Q. He, C. Hammond, P. J. Miedziak, N. Dimitratos, M. Sankar, A. A. Herzing, M. Conte, J. A. Lopez-Sanchez, C. J. Kiely, D. W. Knight, S. H. Taylor, G. J. Hutchings, *Angew. Chem. Int. Ed.*, **2011**, *50*, 10136-10139.

[32] Y. Shen, S. Zhang, H. Li, Y. Ren, H. Liu, *Chem.–A Eur. J.*, **2010**, *16*, 7368-7371.

[33] R. K. P. Purushothaman, J. van Haveren, D. S. van Es, I. Melián-Cabrera, J. D. Meeldijk, H. J. Heeres, *Appl. Catal. B: Environ.*, **2014**, *147*, 92-100.

[34] P. Lakshmanan, P. P. Upare, N. T. Le, Y. K. Hwang, D. W. Hwang, U. H. Lee, H. R. Kim, J. S. Chang, *Appl. Catal. A: General*, **2013**, *468*, 260-268.

[35] J. Xu, H. Zhang, Y. Zhao, B. Yu, S. Chen, Y. Li, L. Hao, Z. Liu, *Green Chem.*, **2013**, *15*, 1520-1525.

[36] E. Derouane, *Cat. Tech.*, **2001**, *5*, 214-225.

[37] A. Z. Fadhel, P. Pollet, C. L. Liotta, C. A. Eckert, *Mol.*, **2010**, *15*, 8400-8424.

[38] E. Skrzyńska, J. Ftouni, J. S. Girardon, M. Capron, L. J. Duhamel, J. F. Paul, F. Dumeignil, *ChemSusChem*, **2012**, *5*, 2065-2078.

[39] J. Lyklema, *Bull. Pol. Acad. Sci.*, **2005**, *53*, 317-322.

[40] D. H. Everett, *Pure Appl. Chem.*, **1972**, *31*, 579.

[41] A. N. Shipway, E. Katz, I. Willner, *ChemPhysChem*, **2000**, *1*, 18-52.

[42] G. Schmid, Elsevier, Netherland, **2008**.

[43] N. Toshima, T. Yonezawa, *New J. Chem.*, **1998**, *22*, 1179-1201.

[44] V. K. LaMer, R. H. Dinegar, *J. Am. Chem. Soc.*, **1950**, *72*, 4847-4854.

[45] L. D. Pachón, G. Rothenberg, *Appl. Organomet. Chem.*, **2008**, *22*, 288-299.

[46] M. Faraday, *Philos. Trans. R. Soc. London*, **1857**, *147*, 145-181.

[47] J. Turkevich, P. C. Stevenson, J. Hillier, *Discuss. Faraday Soc.*, **1951**, *11*, 55-75.

[48] J. Turkevich, G. Kim, *Sci.*, **1970**, *169*, 873-879.

[49] J. Turkevich, *Gold Bull.*, **1985**, *18*, 86-91.

[50] F. Fievet, J. P. Lagier, M. Figlarz, *MRS Bull.*, **1989**, *14*, 29-34.

[51] F. Fievet, J. P. Lagier, B. Blin, B. Beaudoin, M. Figlarz, *Solid State Ion.*, **1989**, *32–33, Part 1*, 198-205.

[52] H. Hirai, Y. Nakao, N. Toshima, *J. Macromol. Sci.: Part A-Chem.*, **1979**, *13*, 727-750.

[53] T. Teranishi, M. Miyake, *Chem. Mater.*, **1998**, *10*, 594-600.

[54] E. Ramirez, S. Jansat, K. Philippot, P. Lecante, M. Gomez, A.M. Masdeu-Bultó, B. Chaudret, *J. Organomet. Chem.*, **2004**, *689*, 4601-4610.

[55] C. Bock, C. Paquet, M. Couillard, G. A. Botton, B. R. MacDougall, *J. Am. Chem. Soc.*, **2004**, *126*, 8028-8037.

[56] J. Yang, T. C. Deivaraj, H. P. Too, J. Y. Lee, *Langmuir*, **2004**, *20*, 4241-4245.

[57] M. T. Reetz, W. Helbig, *J. Am. Chem. Soc.*, **1994**, *116*, 7401-7402.

[58] A. Fukuoka, A. Sato, K. Y. Kodama, M. Hirano, S. Komiya, *Inorg. Chimica Acta*, **1999**, *294*, 266-274.

[59] J. Park, J. Joo, S. G. Kwon, Y. Jang, T. Hyeon, *Angew. Chem. Int. Ed.*, **2007**, *46*, 4630-4660.

[60] L. S. Ott, R. G. Finke, *Coord. Chem. Rev.*, **2007**, *251*, 1075-1100.

[61] H. Bönnemann, K. S. Nagabhushana, R. M. Richards, Wiley-VCH Verlag GmbH & Co. KGaA, Weinheim, **2008**.

[62] Y. Borodko, S. M. Humphrey, T. D. Tilley, H. Frei, G. A. Somorjai, *J. Phys. Chem. C*, **2007**, *111*, 6288-6295.

[63] D. A. Tomalia, A. M. Naylor, W. A. Goddard, *Angew. Chem. Int. Ed.*, **1990**, *29*, 138-175.

[64] R. M. Crooks, M. Zhao, L. Sun, V. Chechik, L. K. Yeung, *Acc. Chem. Res.*, **2000**, *34*, 181-190.

[65] L. Balogh, D. A. Tomalia, *J. Am. Chem. Soc.*, **1998**, *120*, 7355-7356.

[66] J. Cookson, *Platinum Met. Rev.*, **2012**, *56*, 83-98.

[67] D. G. Gálvez, P. Nolis, K. Philippot, B. Chaudret, P. W. N. M. van Leeuwen, *ACS Catal.*, **2012**, *2*, 317-321.

[68] C. S. Weisbecker, M. V. Merritt, G. M. Whitesides, *Langmuir*, **1996**, *12*, 3763-3772.

[69] J. C. Love, L. A. Estroff, J. K. Kriebel, R. G. Nuzzo, G. M. Whitesides, *Chem. Rev.*, **2005**, *105*, 1103-1170.

[70] D. V. Leff, L. Brandt, J. R. Heath, *Langmuir*, **1996**, *12*, 4723-4730.

[71] P. Herves, M. P. Lorenzo, L. M. Liz-Marzan, J. Dzubiella, Y. Lu, M. Ballauff, *Chem. Soc. Rev.*, **2012**, *41*, 5577-5587.

[72] L. Djakovitch, K. Köhler, J. G. d. Vries, Wiley-VCH Verlag GmbH & Co. KGaA, Weinheim, **2008**.

[73] S. Sawoo, D. Srimani, P. Dutta, R. Lahiri, A. Sarkar, *Tetrahedron*, **2009**, *65*, 4367-4374.

[74] J. Baumgrad, Dissertation, Universität Rostock, **2014**.

[75] A. K. Santra, D. W. Goodman, *J. Phys.:Condensed Matter*, **2003**, *15*, 31-62.

[76] J. H. Sinfelt, Wiley, New York, **1983**.

[77] S. Nishimura, Y. Yakita, M. Katayama, K. Higashimine, K. Ebitani, *Catal. Sci. Technol.*, **2013**, *3*, 351-359.

[78] C. H. Christensen, B. Jørgensen, J. Rass-Hansen, K. Egeblad, R. Madsen, S. K. Klitgaard, S. M. Hansen, M. R. Hansen, H. C. Andersen, A. Riisager, *Angew. Chem. Int. Ed.*, **2006**, *45*, 4648-4651.

[79] A. Safavi, H. Kazemi, S. Momeni, M. Tohidi, P. K. Mehrin, *Int. J. Hydrogen Energy*, **2013**, *38*, 3380-3386.

[80] S. Hirasawa, Y. Nakagawa, K. Tomishige, *Catal. Sci. Technol.*, **2012**, *2*, 1150-1152.

[81] L. F Liotta, A. M Venezia, G. Deganello, A. Longo, A. Martorana, Z. Schay, L. Guczi, *Catal. Today*, **2001**, *66*, 271-276.

[82] Z. Y. Shih, C. W. Wang, G. Xu, H. T. Chang, *J. Mater. Chem. A*, **2013**, *1*, 4773-4778.

[83] S. Hu, L. Scudiero, S. Ha, *Electrochimica Acta*, **2012**, *83*, 354-358.

[84] H. Zhang, T. Watanabe, M. Okumura, M. Haruta, N. Toshima, *Nat. Mater*, **2012**, *11*, 49-52.

[85] D. Xu, Z. Liu, H. Yang, Q. Liu, J. Zhang, J. Fang, S. Zou, K. Sun, *Angew. Chem. Int. Ed.*, **2009**, *48*, 4217-4221.

[86] J. H. Sinfelt, *J. Catal.*, **1973**, *29*, 308-315.

[87] R. Ferrando, J. Jellinek, R. L. Johnston, *Chem. Rev.*, **2008**, *108*, 845-910.

[88] C. Tojo, M. de Dios, M. A. López-Quintela, *J. Phys. Chem. C*, **2009**, *113*, 19145-19154.

[89] D. I. Garcia-Gutierrez, C. E. Gutierrez-Wing, L. Giovanetti, J. M. Ramallo-López, F. G. Requejo, M. Jose-Yacaman, *J. Phys. Chem. B*, **2005**, *109*, 3813-3821.

[90] V. Mazumder, M. Chi, K. L. More, S. Sun, *Angew. Chem. Int. Ed.*, **2010**, *49*, 9368-9372.

[91] Y. Mizukoshi, T. Fujimoto, Y. Nagata, R. Oshima, Y. Maeda, *J. Phys. Chem. B*, **2000**, *104*, 6028-6032.

[92] M. G. Weir, M. R. Knecht, A. I. Frenkel, R. M. Crooks, *Langmuir*, **2009**, *26*, 1137-1146.

[93] M. Michaelis, A. Henglein, P. Mulvaney, *J. Phys. Chem.*, **1994**, *98*, 6212-6215.

[94] N. Toshima, Y. Wang, *Chem. Lett.*, **1993**, *22*, 1611-1614.

[95] N. Toshima, Y. Wang, *Adv. Mater.*, **1994**, *6*, 245-247.

[96] H. Bönnemann, G. Braun, W. Brijoux, R. Brinkmann, A. S. Tilling, K. Seevogel, K. Siepen, *J. Organomet. Chem.*, **1996**, *520*, 143-162.

[97] J. Schäffer, V. A. Kondratenko, N. Steinfeldt, M. Sebek, E.V. Kondratenko, *J. Catal.*, **2013**, *301*, 210-216.

[98] B. R. Cuenya, *Thin Solid Films*, **2010**, *518*, 3127-3150.

[99] J. Hagen, Wiley, Germany, **2008**.

[100] D. Astruc, Wiley-VCH Verlag GmbH & Co. KGaA, Germany, **2008**.

[101] G. F. Froment, Springer, Netherlands, **1982**.

[102] C. H. Bartholomew, *Appl. Catal. A: General*, **2001**, *212*, 17-60.

[103] M. Besson, P. Gallezot, *Catal. Today*, **2000**, *57*, 127-141.

[104] S. Keav, J. Barbier, D. Duprez, *Catal. Sci. Technol.*, **2011**, *1*, 342-353.

[105] J. A. Lopez-Sanchez, N. Dimitratos, C. Hammond, G. L. Brett, L. Kesavan, S. White, P. Miedziak, R. Tiruvalam, R. L. Jenkins, A. F. Carley, D. Knight, C. J. Kiely, G. J. Hutchings, *Nat. Chem.*, **2011**, *3*, 551-556.

[106] C. Aliaga, J. Y. Park, Y. Yamada, H. S. Lee, C. K. Tsung, P. Yang, G. A. Somorjai, *J. Phys. Chem. C*, **2009**, *113*, 6150-6155.

[107] N. Long, M. Ohtaki, M. Nogami, T. Hien, *Colloid Poly. Sci.*, **2011**, *289*, 1373-1386.

[108] J. Monzó, M. T. M. Koper, P. Rodriguez, *ChemPhysChem*, **2012**, *13*, 709-715.

[109] A. M. Venezia, L. F. Liotta, G. Pantaleo, V. La Parola, G. Deganello, A. Beck, Z. Koppány, K. Frey, D. Horváth, L. Guczi, *Appl. Catal. A: General*, **2003**, *251*, 359-368.

[110] R. M. Rioux, H. Song, J. D. Hoefelmeyer, P. Yang, G. A. Somorjai, *J. Phys. Chem. B*, **2004**, *109*, 2192-2202.

[111] G. A. Loraine, *Water Environ. Res.*, **2008**, *80*, 373-379.

[112] A. Varga, N. A. Brunelli, M. W. Louie, K. P. Giapisb, S. M. Hailea, *J. Mater. Chem.*, **2010**, *20*, 6309-6315.

[113] H. Ning, J. Song, M. Hou, D. Yang, H. Fan, B. Han, *Sci. China Chem.*, **2013**, *56*, 1578-1585.

[114] A. A. Rosatella, S. P. Simeonov, R. F. M. Frade, C. A. M. Afonso, *Green Chem.*, **2011**, *13*, 754-793.

[115] B. Siyo, M. Schneider, J. Radnik, M. M. Pohl, P. Langer, N. Steinfeldt, *Appl. Catal. A: General*, **2014**, *478*, 107-116.

[116] Y. Y. Gorbanev, S. K. Klitgaard, J. M. Woodley, C. H. Christensen, A. Riisager, *ChemSusChem*, **2009**, *2*, 672-675.

[117] S. E. Davis, M. S. Ide, R. J. Davis, *Green Chem.*, **2013**, *15*, 17-45.

[118] K. R. Vuyyuru, P. Strasser, *Catal. Today*, **2012**, *195*, 144-154.

[119] T. Pasini, M. Piccinini, M. Blosi, R. Bonelli, S. Albonetti, N. Dimitratos, J. A. Lopez-Sanchez, M. Sankar, Q. He, C. J. Kiely, G. J. Hutchings, F. Cavani, *Green Chem.*, **2011**, *13*, 2091-2099.

[120] K. Yutaka, T. Miura, S. Eritate, T. Komuro, Patents, US20110092720 A1, **2011**.

[121] P. Verdeguer, N. Merat, A. Gaset, *J. Mol. Catal.*, **1993**, *85*, 327-344.

[122] W. Partenheimer, Vladimir V. Grushin, *Adv. Synth. Catal.*, **2001**, *343*, 102-111.

[123] O. Casanova, S. Iborra, A. Corma, *ChemSusChem*, **2009**, *2*, 1138-1144.

[124] H. A. Rass, N. Essayem, M. Besson, *Green Chem.*, **2013**, *15*, 2240-2251.

[125] N. K. Gupta, S. Nishimura, A. Takagaki, K. Ebitani, *Green Chem.*, **2011**, *13*, 824-827.

[126] Y. Gorbanev, S. Kegnæs, A. Riisager, *Top. Catal.*, **2011**, *54*, 1318-1324.

[127] Y. Gorbanev, S. Kegnæs, A. Riisager, *Catal. Lett.*, **2011**, *141*, 1752-1760.

[128] B. Zope, S. Davis, R. Davis, *Top. Catal.*, **2012**, *55*, 24-32.

[129] S. E. Davis, B. N. Zope, R. J. Davis, *Green Chem.*, **2012**, *14*, 143-147.

[130] G. Arzamendi, E. Arguiñarena, I. Campo, S. Zabala, L. M. Gandía, *Catal. Today*, **2008**, *133–135*, 305-313.

[131] F. Ma, M. A. Hanna, *Bioresour. Technol.*, **1999**, *70*, 1-15.

[132] A. Demirbas, M. F. Demirbas, *Energy Convers. Manage.*, **2011**, *52*, 163-170.

[133] Y. Nakagawa, K. Tomishige, *Catal. Sci. Technol.*, **2011**, *1*, 179-190.

[134] B. Katryniok, S. Paul, V. Belliere-Baca, P. Rey, F. Dumeignil, *Green Chem.*, **2010**, *12*, 2079-2098.

[135] T. Valliyappan, N. N. Bakhshi, A. K. Dalai, *Bioresour. Technol.*, **2008**, *99*, 4476-4483.

[136] X. Liu, H. Ma, Y. Wu, C. Wang, M. Yang, P. Yan, U. Welz-Biermann, *Green Chem.*, **2011**, *13*, 697-701.

[137] J. R. Ochoa-Gomez, O. Gomez-Jimenez-Aberasturi, C. Ramirez-Lopez, B. Maestro-Madurga, *Green Chem.*, **2012**, *14*, 3368-3376.

[138] F. Liu, K. D. O. Vigier, M. P. Titus, Y. Pouilloux, J. M. Clacens, F. Decampo, F. Jerome, *Green Chem.*, **2013**, *15*, 901-909.

[139] A. Martin, M. Richter, *Eur. J. Lipid Sci. Technol*, **2011**, *113*, 100-117.

[140] J. J. W. Eshuis, J. A. M. Laan, R. P. Potman, *Zeolites*, **1996**, *17*, 316-316.

[141] M. Aresta, A. Dibenedetto, F. Nocito, C. Pastore, *J. Mol. Catal. A: Chem.*, **2006**, *257*, 149-153.

[142] B. N. Zope, D. D. Hibbitts, M. Neurock, R. J. Davis, *Sci.*, **2010**, *330*, 74-78.

[143] R. Nie, D. Liang, L. Shen, J. Gao, P. Chen, Z. Hou, *Appl. Catal. B: Environ.*, **2012**, *127*, 212-220.

[144] W. Hu, D. Knight, B. Lowry, A. Varma, *Ind. Eng. Chem. Res.*, **2010**, *49*, 10876-10882.

[145] E. G. Rodrigues, S. A. C. Carabineiro, J. J. Delgado, X. Chen, M. F. R. Pereira, J. J. M. Órfão, *J. Catal.*, **2012**, *285*, 83-91.

[146] S. Demirel, K. Lehnert, M. Lucas, P. Claus, *Appl. Catal. B: Environ.*, **2007**, *70*, 637-643.

[147] A. Tsuji, K. T. V. Rao, S. Nishimura, A. Takagaki, K. Ebitani, *ChemSusChem*, **2011**, *4*, 542-548.

[148] J. Gao, D. Liang, P. Chen, Z. Hou, X. Zheng, *Catal. Lett.*, **2009**, *130*, 185-191.

[149] D. Liang, J. Gao, J. Wang, P. Chen, Z. Hou, X. Zheng, *Catal. Commun.*, **2009**, *10*, 1586-1590.

[150] A. Villa, G. M. Veith, L. Prati, *Angew. Chem.*, **2010**, *122*, 4601-4604.

[151] S. Carrettin, McMorn, Paul, Johnston, Peter, Griffin, Ken, Hutchings, Graham J., *Chem. Commun.*, **2002**, 696-697.

[152] N. Dimitratos, A. Villa, C.L. Bianchi, L. Prati, M. Makkee, *Appl. Catal. A: General*, **2006**, *311*, 185-192.

[153] Y. Zhang, Z. Shen, X. Zhou, M. Zhang, F. Jin, *Green Chem.*, **2012**, *14*, 3285-3288.

[154] H. Kishida, F. Jin, Z. Zhou,T. Moriya, H. Enomoto, *Chem. Lett.*, **2005**, *34*, 1560-1561.

[155] D. Roy, B. Subramaniam, R. V. Chaudhari, *ACS Catal.*, **2011**, *1*, 548-551.

[156] E. P. Maris , M. Murayama, R. J. Davis, *J. Catal.*, **2007**, *251*, 281-294.

[157] Y. Fan, C. Zhou, X. Zhu, *Catal. Rev.*, **2009**, *51*, 293-324.

[158] K. Fukushima, Y. Kimura, *Poly. Int.*, **2006**, *55*, 626-642.

[159] R. M. West, M. S. Holm, S. Saravanamurugan, J. Xiong, Z. Beversdorf, E. Taarning, C. H. Christensen, *J. Catal.*, **2010**, *269*, 122-130.

[160] V. K. Pecharsky, P. Y. Zavalij, Springer, New York, **2005**.

[161] R. E. Dinnebier, S. J. L. Billinge, Royal Society of Chemistry, Cambridge, **2008**.

[162] D. B. Williams, C. B. Carter, Springer, New York, **1996**.

[163] S. J. Pennycook, P. D. Nellist, Springer, New York, **2011**.

[164] L. Reimer, Springer, Germeny, **1998**.

[165] B. Abécassis, F. Testard, Q. Kong, B. Francois, O. Spalla, *Langmuir*, **2010**, *26*, 13847-13854.

[166] M. Harada, N. Tamura, M. Takenaka, *J. Phys. Chem. C*, **2011**, *115*, 14081-14092.

[167] N. Steinfeldt, *Langmuir*, **2012**, *28*, 13072-13079.

[168] O. Glatter, O. Kratky, Academic Press, Michigan, **1982**.

[169] A. Einstein, *Anna. Phys.*, **2005**, *14*, 164-181.

[170] P. V. Heide, Wiley, Hoboken- New Jersy, **2011**.

[171] S. Brunauer, P. H. Emmett, E. Teller, *J. Am. Chem. Soc.*, **1938**, *60*, 309-319.

[172] G. Fagerlund, *Mat. Constr.*, **1973**, *6*, 239-245.

[173] B. J. Clark, T. Frost, A. Russell, Springer, London, **1993**.

[174] J. M. Pitarke, V. M. Silkin, E. V. Chulkov, P. M. Echenique, *Rep. Prog. Phys.*, **2007**, *70*, 1.

[175] A. Moores, F. Goettmann, *New J. Chem.*, **2006**, *30*, 1121-1132.

[176] M. B. Krüger, C. Selle, D. Heller, W. Baumann, *J. Chem. Eng. Data*, **2012**, *57*, 1737-1744.

[177] H. P. Choo, K. Y. Liew, H. Liu, *J. Mater. Chem.*, **2002**, *12*, 934-937.

[178] H. Borchert, E. V. Shevchenko, A. Robert, I. Mekis, A. Kornowski, G. Grübel, H. Weller, *Langmuir,* **2005**, *21*, 1931-1936.

[179] M. Kosmulski, *J. Colloid Interf. Sci.*, **2004**, *275*, 214-224.

[180] M. Comotti, W. C. Li, B. Spliethoff, F. Schüth, *J. Am. Chem. Soc.*, **2005**, *128*, 917-924.

[181] V. Raju, R. Radhakrishnan, S. Jaenicke, G. K. Chuah, *Catal. Today*, **2011**, *164*, 139-142.

[182] K. J. A. Raj, B. Viswanathan, *Indian J. Chem.*, **2009**, *48A*, 1378-1382.

[183] C. Berger-Karin, M. Sebek, M. M. Pohl, U. Bentrup, V. A. Kondratenko, N. Steinfeldt, E. V. Kondratenko, *ChemCatChem*, **2012**, *4*, 1368-1375.

[184] Y. Kitamoto, J. S. He, *Electrochimi. Acta*, **2009**, *54*, 5969-5972.

[185] A. Henglein, M. Giersig, *J. Phys. Chem. B*, **1999**, *103*, 9533-9539.

[186] R. E. Benfield, *J. Chem. Soc., Faraday Trans.*, **1992**, *88*, 1107-1110.

[187] S. Magdassi, M. Grouchko, A. Kamyshny, *Mater.*, **2010**, *3*, 4626-4638.

[188] F. Bonet, C. Guéry, D. Guyomard, R. H. Urbina, K. T. Elhsissen, J. M. Tarascon, *Int. J. Inorg. Mater.*, **1999**, *1*, 47-51.

[189] F. Papa, C. Negrila, A. Miyazaki, I. Balint, *J. Nano. Res.*, **2011**, *13*, 5057-5064.

[190] W. E. Kaden, T. Wu, W. A. Kunkel, S. L. Anderson, *Sci.*, **2009**, *326*, 826-829.

[191] J. H. Kang, E. W. Shin, W. J. Kim, J. D. Park, S. H. Moon, *J. Catal.*, **2002**, *208*, 310-320.

[192] K. Okumura, M. Niwa, *Catal. Surv. from Asia*, **2002**, *5*, 121-126.

[193] S. W. Gaarenstroom, N. Winograd, *J. Chem. Phys.*, **1977**, *67*, 3500-3506.

[194] J. P. Espinós, J. Morales, A. Barranco, A. Caballero, J. P. Holgado, A.R. González-Elipe, *J. Phys. Chem. B*, **2002**, *106*, 6921-6929.

[195] B. Siyo, M. Schneider, M. M. Pohl, P. Langer, N. Steinfeldt, *Catal. Lett.*, **2013**, *144*, 498-506.

[196] K. Mori, T. Hara, T. Mizugaki, K. Ebitani, K. Kaneda, *J. Am. Chem. Soc.*, **2004**, *126*, 10657-10666.

[197] Y. Li, E. Boone, M. A. El-Sayed, *Langmuir*, **2002**, *18*, 4921-4925.

[198] J. Le-Bars, U. Specht, J. S. Bradley, D. G. Blackmond, *Langmuir*, **1999**, *15*, 7621-7625.

[199] Y. F. Han, D. Kumar, D.W. Goodman, *J. Catal.*, **2005**, *230*, 353-358.

[200] R. Narayanan, M. A. El-Sayed, *J. Am. Chem. Soc.*, **2003**, *125*, 8340-8347.

[201] G. Porod, O. Glatter, O. Kratky, Academic Press, London, **1982**.

[202] Y. Xiong, J. Chen, B. Wiley, Y. Xia, S. Aloni, Y. Yin, *J. Am. Chem. Soc.*, **2005**, *127*, 7332-7333.

[203] J. Baumgard, M. M. Pohl, U. Kragl, N. Steinfeldt, *Nanotechnol. Rev.*, **2013**, *3*, 87-98.

[204] H. Li, L. Li, Y. Li, *Nanotechnol. Rev.*, **2013**, *2*, 515-528.

[205] W. X. Lu, C. G. Yan, R. Yao, *Synth. Commun.*, **1996**, *26*, 3719-3723.

[206] M. L. Toebes, J. A. van Dillen, K. P. de-Jong, *J. Mol. Catal. A: Chem.*, **2001**, *173*, 75-98.

[207] S. K. Sharma, P. A. Parikh, R.V. Jasra, *J. Mol. Catal. A: Chem.*, **2007**, *278*, 135-144.

[208] A. Corma, S. Iborra, S. Miquel, J. Primo, *J. Catal.*, **1998**, *173*, 315-321.

[209] P. Kuśtrowski, L. Chmielarz, E. Bożek, M. Sawalha, F. Roessner, *Mater. Res. Bull.*, **2004**, *39*, 263-281.

[210] S. Carrettin, P. McMorn, P. Johnston, K. Griffin, C. J. Kiely, G. J. Hutchings, *Phys. Chem. Chem. Phys.*, **2003**, *5*, 1329-1336.

[211] T. Mallat, A. Baiker, *Catal. Today*, **1994**, *19*, 247-283.

[212] P. Gallezot, *Catal. Today*, **1997**, *37*, 405-418.

[213] S. Demirel-Gülen, M. Lucas, P. Claus, *Catal. Today*, **2005**, *102*, 166-172.

[214] S. Hirasawa, H. Watanabe, T. Kizuka, Y. Nakagawa, K. Tomishige, *J. Catal.*, **2013**, *300*, 205-216.

[215] O. Glatter, *J. Appl. Crystall.*, **1980**, *13*, 7-11.

Curriculum Vitae

Baraa Siyo

Date/Place of Birth: August 29, 1985/ Latakia (Syria)

Work address
Leibniz-Institut für Katalyse e.V

Albert-Einstein-Str. 29a,

18059 Rostock, Germany
E-mail: baraa.siyo@catalysis.de
Tel.: +49 (0)381 1281 177

Home address
Max-Planck-Str. 3,

Haus 3B, Zi. 2.03.2

18059 Rostock, Germany

E-mail:baraa.siyo@yahoo.com

Academics:

January 2012 - June 2014	PhD student in Chemistry, Leibniz Institute for Catalysis (Likat) at University of Rostock, Germany, Supervisor: Prof. Dr. Peter Langer and Dr. Norbert Steinfeldt. Title: Development of Palladium Nanoparticles Based Catalysts for Aerobic Oxidation of 5-Hydroxymethylfurfural and Glycerol.
2010-2011	Equivalent Master in Chemistry, Institute of Chemistry-University of Rostock, Germany, Supervisor: Prof. Dr. Peter Langer. Title: Synthesis of N,N´-Diglycosylated Isoindigo-Derivatives and Regioselective Pd(0)-Catalysed Cross-Coupling Reactions of 2,4-Dichloro-1-(trifluoromethyl)benzene.

2007-2008	Diploma in educational qualification (Excellent), Tishreen University, Latakia/Syria.
2004-2007	Bachelor Degree in Chemistry- Faculty of Science-Department of Chemistry- Tishreen University, Latakia/Syria (Very good), rank 1st.
2002-2003	Secondary School Certificate, Latakia/Syria

Work

2008-2010	Assistant lecturer for undergraduate students, Tishreen University, Latakia/Syria

Languages English, German, Arabic (Mother Tongue).

References:

Prof. Dr. Peter Langer

Department of Organic Chemistry,

Albert-Einstein St. 3a,

18059 Rostock, Germany

Tel.: +49 (0)381 498 6410

E-mail: peter.langer@uni-rostock.de

Dr. Norbert Steinfeldt

Leibniz-Institut für Katalyse e.V.

Albert-Einstein-Str. 29a,

18059 Rostock, Germany

Tel.: +49 (0)381 1281 319

Fax.: +49 (0)381 1281 5319

E-mail: norbert.steinfeldt@catalysis.de

Publications:

1. **Baraa Siyo**, Matthias Schneider, Marga-Martina Pohl, Peter Langer, Norbert Steinfeldt, *Catalysis Letter*, **2014**, *144*, 498-506. “Synthesis, characterization, and application of PVP-Pd NP in the aerobic oxidation of 5-hydroxymethylfurfural (HMF)”.
2. **Baraa Siyo**, Matthias Schneider, Jörg Radnik, Marga-Martina Pohl, Peter Langer, Norbert Steinfeldt, *Applied Catalysis A: General*, **2014**, *478*, 107–116.“Influence of support on the aerobic oxidation of HMF into FDCA over preformed Pd nanoparticle based materials”.
3. Dennis Kleeblatt, **Baraa Siyo**, Martin Hein, Viktor Iaroshenko, Jamshed Iqbal, Alexander Villinger, Peter Langer, *Organic & Biomolecular Chemistry*, **2013**, *11*, 886-895. “Synthesis of *N,N’*-Diglycosylated Isoindigos”.
4. Iftikhar Ali, **Baraa Siyo**, Zahid Hassan, Imran Malik, Ihsan Ullah, Asad Ali, Muhammad Nawaz, Jamshed Iqbal, Tamás Patonay, Alexander Villinger, Peter Langer, *Journal of Fluorine Chemistry*, **2013**, *145*, 18-34. “Synthesis of trifluoromethyl-substituted di- and terphenyls by site-selective Suzuki-Miyaura reactions of various dihalogenated trifluoromethyl-benzene derivatives”.
5. Iftikhar Ali, **Baraa Siyo**, Yaseen Al Soud, Alexander Villinger, Peter Langer, *Synthesis* **2012**, *44*, 1637-1646. “Regioselective Suzuki-Miyaura Cross-Coupling Reactions of 2,6-Dichloroquinoxaline”.

Participation in Conferences/Oral Presentation:

1. Jens Baumgard, **Baraa Siyo**, Norbert Steinfeldt. “Synthesis of tailored metallic nanoparticles and their application in liquid phase reaction“.1st International Symposium on Nanoparticles/Nanomaterial and Applications, Caparica, Portugal, 20-22 January 2014.
2. Jens Baumgard, **Baraa Siyo**, Norbert Steinfeldt. “Influence of NaOH on formation of Pd nanoparticles in ethylene glycol”. 7th Workshop of Chemical and Biological Micro Laboratory Technology, Ilmenau/Elgersburg, 25-27 February, 2014.
3. Norbert Steinfeldt, **Baraa Siyo.** "Development of tailored Pd nanoparticle based catalysts for aerobic oxidation of 5-hydroxymethylfurfural in to 2,5-furandicarboxylic acid". 2nd International Symposium on Green Chemistry Renewable carbon and Eco-Efficient Processes, 21-24 May 2013, La Rochelle – France.

Participation in Conferences/Poster:

1. **Baraa Siyo**, Matthias Schneider, Jörg Radnik, Marga-Martina Pohl, Peter Langer, Norbert Steinfeldt. "Aerobic oxidation of 5-hydroxymethylfurfural to 2,5-furandicarboxylic acid catalyzed by pre-formed Pd nanoparticles based materials". X6. Jahrestreffen Deutscher Katalytiker, 13-15 March 2013, Weimar-Germany.

2. **Baraa Siyo**, Matthias Schneider, Martin Adam, Jörg Radnik, Marga-Martina Pohl, Wolfgang Baumann, Peter Langer, Norbert Steinfeldt. "Selective oxidation of glycerol into lactic acid over preformed Pd and Pd-Ag nanoparticles (NPs) based materials".CASuS-LIKAT Workshop, 16-18 September 2013, Rostock-Germany.